2014

# Effect Of Electrospun Nanofibers On The Short Beam Strength Of Laminated Fiberglass Composite

Dattaji K. Shinde
*North Carolina Agricultural and Technical State University*

# Effect of Electrospun Nanofibers on the Short Beam Strength of Laminated Fiberglass Composite

Dattaji K. Shinde

North Carolina A&T State University

A dissertation submitted to the graduate faculty

in partial fulfillment of the requirements for the degree of

DOCTOR OF PHILOSOPHY

Department: Nanoengineering

Major: Nanoengineering

Major Professor: Dr. Ajit D. Kelkar

Greensboro, North Carolina

2014

The Graduate School
North Carolina Agricultural and Technical State University
This is to certify that the Doctoral Dissertation of

Dattaji K. Shinde

has met the dissertation requirements of
North Carolina Agricultural and Technical State University

Greensboro, North Carolina
2014

Approved by:

Dr. Ajit D. Kelkar
Major Professor

Dr. James G. Ryan
Committee Member

Dr. Ram V. Mohan
Committee Member

Dr. Shyam Aravamudhan
Committee Member

Dr. Ajit D. Kelkar
Department Chair

Dr. Lifeng Zhang
Committee Member

Dr. Sanjiv Sarin
Dean, The Graduate School

# Biographical Sketch

Dattaji K. Shinde was born on May 3, 1976, at Shekapur in Latur District, Maharashtra State, India. He received his Bachelor's degree in Mechanical Engineering from Dr. B. A. Marathwada University, Aurangabad, India in 2000 and Master's degree in Design Engineering from Indian Institute of Technology, Delhi, India in 2002. He worked as project engineer in Mahanagar Gas Ltd., Mumbai, India, for one year and later worked as Lecturer in Mechanical Engineering in Rajiv Gandhi Institute of Technology, Mumbai India for five years. Since 2008, he is working as associate professor in production engineering in Veermata Jijabai Technological Institute -VJTI, Mumbai, India. He joined the Ph. D. program at North Carolina Agricultural & Technical State University in the fall of 2011. His area of research interest includes design engineering, fracture mechanics, low cost manufacturing of composites, electrospinning, nanocomposites, failure of composite materials, nanomaterials, and analytical and finite element modeling and analysis of composites.

# Dedication

To my father Kashinath P. Shinde and my mother Dropati K. Shinde and my wife Deepmala for always were being with me in all moments of life. Also to my two loving sons Rohit and Ishan.

# Acknowledgments

I am extremely grateful to Dr. Ajit D. Kelkar, for his constant support, motivation and valuable guidance for performing this research and, also for giving me opportunities to participate in national and international conferences, and for being a great mentor during my Ph. D. Program. I am sincerely thankful to Drs. James G. Ryan, Ram V. Mohan, Shyam Aravamudhan, and Lifeng Zhang for serving on my advisory committee and their valuable suggestions and advice regarding my dissertation research and writing.

I would like to express my thanks to Dr. Evan Kimbro for his support during experiments and laboratory work. I am also thankful to Mrs. Kareen Ryan for her help in gaining access to laboratories during my research. I appreciate the help and guidance of Dr. Srinivas Gundla and I am also thankful to Ms. Jaqueline Oates, Ms. Karen Courtney, and Ms. Patricia Hedley for their administrative help.

I would like to express my gratitude to all my friends who have directly or indirectly supported and helped me. I am truly indebted to Dr. K. G. Narayankhedekar, Ex-director of VJTI, Dr. D. N. Raut, Professor and Dean of Administration, VJTI, and Dr. R. N. Awale, Professor, VJTI and Ex-Dean Academic for their encouragement and constant support to pursue a Ph. D. Degree.

I am deeply thankful to my father Kashinath, my mother Dropati, my brother, Balaji Shinde and other family members who believed in my potential and encouraged me for higher education studies abroad. My loving thanks to my wife, Deepmala, and two precious diamonds Rohit and Ishan who are always with me in everything I do.

Finally, I acknowledge Joint School of Nanoscience and Nanoengineering for financial support for research.

Table of Contents

List of Figures

*List of Tables*

## Abstract

High specific modulus and strength are the most desirable properties for the material used in structural applications. Composite materials exhibit these properties and over the last decade, their usage has increased significantly, particularly in automotive, defense, and aerospace applications. The major cause of failures in composite laminates is due to delaminations. Delamination in composite laminates can occur due to fatigue, low velocity impact and other loadings modes. Conventional methods like “through-the-thickness stitching” or “Z-Pinning” have limitations for improving flexural and interlaminar properties in woven composites due to the fact that while improving interlaminar properties, the presence of stitches or Z pins affects in-plane properties.

This study investigates the flexural behavior of fiberglass composites interleaved with non-woven Tetra Ethyl Orthosilicate(TEOS) electrsopsun nanofibers(ENFs). TEOS ENFs were manufactured using an electrospinning technique and then sintered. Nanoengineered beams were fabricated by interleaving TEOS ENFs between the laminated fiberglass composites to improve the flexural properties.

TEOS ENFs, resin film, and failed fiberglass laminated composites with and without nanofibers were characterized using SEM Imaging and ASTM standard testing methods. A hybrid composite was made by interleaving a non-woven sheet of TEOS ENFs between the fiberglass laminates with additional epoxy resin film and fabricated using the out of autoclave vacuum bagging method. Four commonly used stacking sequences of fiberglass laminates with and without nanofibers were used to study the progressive failure and deformation mechanics under flexural loadings. The experimental study has shown significant improvements in short beam strength and strain energy absorption in the nanoengineered laminated fiberglass

composites before complete failure. The modes were investigated by performing detailed fractographic examination of failed specimens.

Experimental results were validated by developing a detailed three dimensional finite element model. Results of the progressive deformation and damage mechanics from the finite element model agreed well with the experimental results. Overall, nanoengineered beams showed improvement in the short beam strength and 30 % improvement in energy absorption as compared to a fiberglass beam without the presence of nanofibers.

# CHAPTER 1

# Introduction

## 1.1 General Introduction

Composite materials are made of two or more materials and are designed to have better engineering properties than any of its constituents. Fiber-reinforced composite materials are a specialized type of high performance structural composite that consists of fibers embedded in a matrix. Fibers may be made from glass, carbon, or Kevlar and have a higher strength than the matrix material. The matrix serves as a load transfer medium between the fibers and it also keeps the fibers in the desired orientation. The matrix may be made from a polymer, metal, or ceramic. The fibers architecture can be woven, braided, or individually spaced. Also fibers can be continuous or discontinuous and can have random or set orientations.

A lamina consists of a thin layer of continuous fibers surrounded by matrix material. The fibers in a lamina can be oriented in a single direction or multiple directions as in the case of woven fiber composites. Each individual lamina with continuous unidirectional fibers has two planes of symmetry and its mechanical properties can be considered orthotropic, in which material properties in the direction parallel to the fibers are different than those in the direction normal to the fibers.

The lamina can be stacked and consolidated to form a laminate. The laminate is unidirectional when the fibers of all lamina are oriented in the same direction and multidirectional when the fiber orientations of the lamina are in different direction of orientation. The sequence of stacking the laminates (or lay-ups), gives fiber-reinforced composites a wide range of structural properties. The stacking sequence can be symmetric or asymmetric about the mid-surface of the laminate. In general, symmetric laminates are angle-ply and cross-ply

laminates. Angle-ply laminates consist of lamina that alternate fiber orientation angle, +θ/- θ /+ θ /- θ s Cross-ply laminates consist of lamina with 0° or 90° fiber orientation angles, such as 0°/90°/90/0°. Symmetric the laminates have quasi-isotropic properties and are composed of a specific stacking sequence so that the mechanical properties of the laminate are isotropic even though each lamina is orthotropic.(Slager, 2007)

Thus composite materials have been considered as advanced materials solutions for demanding aerospace, automobile, wind energy, and defense applications. Fiber reinforced polymeric (FRP) composites have high strength, light weight, and high strength to weight ratio as compared with steel. They are also easily manufactured using molding processes. The continuous fiber reinforced polymer matrix composite has been widely used in the fields mentioned above as shown to be a key performance enabler in many applications. High performance S-glass fiber reinforced polymeric composites provide a unique combination of properties such as strength, impact resistance, stiffness, temperature resistance, fatigue resistance, light weight and radar transparency as compared with conventional glass fibers (AGY, 2004) and also, deliver better cost performance than aramid and carbon fibers.

The strength of composite materials can be determined experimentally, however it is more practical to estimate composite performance by modeling behavior in response to an applied load. In fact, a model should be able to predict laminate behavior for any lay-up using parameters determined from testing the same material, but not necessarily the same layup process. Differences between theoretical predictions of laminate behavior and experimental results have forced numerous refinements of theories describing composite behavior.

## 1.2 Motivation

The motivation for this research was to address the most common failure of glass fiber reinforced polymeric (GFRP) composites, delamination. In order to understand the long term behavior of GFRP under static, fatigue and dynamic loading, it is essential, to perform laboratory testing and characterize the composite material. Failure occurring in the static and fatigue model for GFRP is progressive damage from the combination of matrix cracking, fiber breaking, delamination, and buckling of fibers etc.

Various modes of failure depend on factors such as, fiber architecture, fiber volume fraction, matrix properties, type of loading, frequency, manufacturing process and environmental exposures. Failure analysis of a composites material is very important in order to understand how a structural component can be loaded. There are three types of delamination failures such as interlaminar, intralaminar, and translaminar. The most common failure is interlaminar because of the varying Poisson ratios of different ply orientations. Depending on the loading conditions there are three types of composite failure, which include tension (Mode I), shear (Mode II), tearing (Mode III), or a combination of the three. Failure analysis investigates the physical evidence left behind from a fracture or crack face that exhibit characteristic features that change with loading, type of fiber or resin material, structural configuration, environment and other factors. The most effective way to determine the characteristic fracture features that are produced under different loading conditions is to fabricate test specimens and load them in a controlled manner. From these test specimens, the characteristic fracture features can then be documented with a known crack direction.

In order to achieve successful design life for composite materials, the designer has must choose the appropriate composite material for the application in order to avoid failure with the

designed service life. Thus, it is urgent need to understand mechanisms of failure of composites, degradation in service life, in order to predict the life of a GFRP composite under design conditions.

In the past 30 years, the stiffness degradation and damage mechanisms of FRP composite materials have been actively studied by materials scientists and engineers. Also extensive research has been carried to understand the fracture behavior of composite materials(Curtis P T, 1989). Researchers have shown that progressive damages in FRP composites due to matrix micro-cracking, due to the existence of voids and pre-defect, delamination of plies of unidirectional and bidirectional FRP composite as shown in Fig. 1(Paiva et al., 2006**)**.

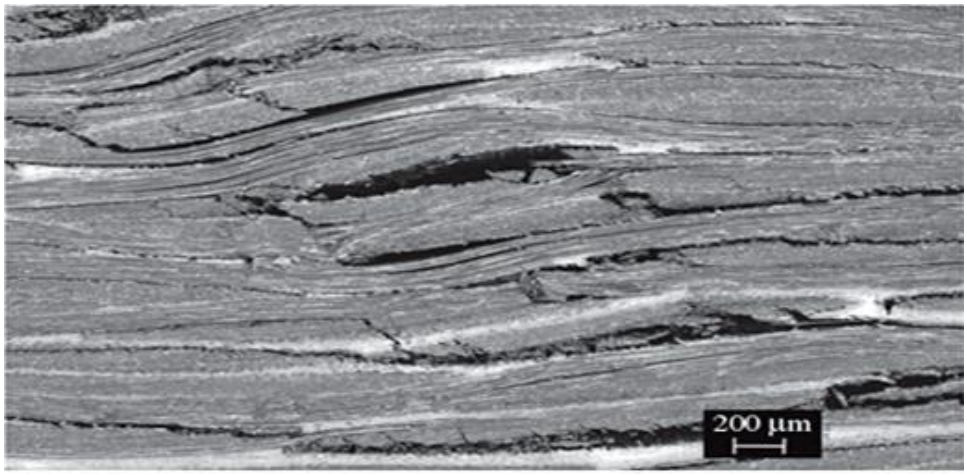


*Figure 1.1.* Delamination of plies in composite laminates after shear test

The main focus of this research is to investigate the effects associated with the introduction of a new nanomaterial between the plies of a fiberglass composite and analyze fracture in the composite in order to improve resistance to delamination failure modes.

## 1.3 Review of Earlier Work

### 1.3.1 Electrospinning Process

In an electrospinning process, small diameter nanofibers are manufactured to create a fibrous mat. Electrospinning uses an electric field created by a high voltage power supply to

generate fibers of varying diameters from a sol-gel solution to a ground collector. There are various uses of this type of fiber mat. The process originally developed around 1934 by Formahals is shown in Figure 1.2 (Formhals, 1934), and has been used in mechanical engineering and the bio-medical fields. Electrospinning has also been used in research involving biomedical tissue engineering and drug enhancements (Fang et al., 2008; Z.-M. Huang et al., 2003).

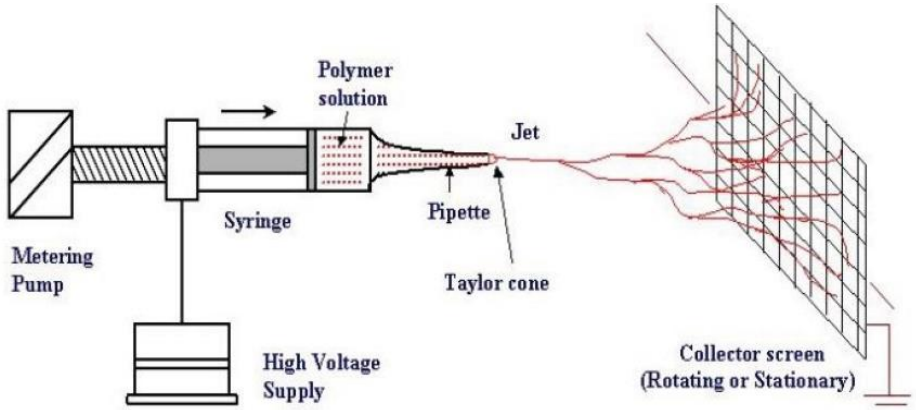


*Figure 1.2.* Schematic of the electrospinning setup

The electrospinning set-up consists of main four components; spinneret at positive potential, a grounded collector plate, a high voltage supply and a solution dispensing pump. The dispensing pump controls the rate of sol-gel discharge at the spinneret tip. Sol-gel flow rate is adjusted depending upon the viscosity and voltage applied. At low viscosity and voltage, the discharge rate of solution is expected to be in the range of 0.1 ml per min. to 10 ml per min. When the Sol-gel solution is aging at ambient conditions of temperature and humidity, then this discharge rate is sufficient to have a full double layer deposition of electrospun nanofibers (ENFs) on 16 inches by 20 inches Teflon sheet in 2 hours. When the solution approaches the tip of the spinneret, it becomes charged on its surface. The forces acting on a droplet at the tip include hydrostatic surface tension and surface charge due to the applied potential difference. Because tip is at a positive potential and the surface charge on the sol-gel droplet is positive, the

repulsive force counter acts the surface tension and. causes the spherical droplet to stretch into a conical shape called the "Taylor Cone"(Taylor, 1964). There is less surface area on the tip of Taylor cone under influence of the potential difference, causing the tip of cone to elongate into a charged jet that further increases in length and reduces diameter resulting in "Bending Instability"(Reneker et al., 2000). Bending Instability is caused by the non-linear characteristics of electric charge and causes the charged jet to undergo whipping that further elongates and reduces in fiber diameter accompanied by evaporation of solvents is shown in Figure 1.3 (Reneker et al., 2000). Before 1996, limited research work related to the electrospinning was done, but the growing interest in nanotechnology during the mid-1990's and the observation of the nanosize fibers from variety of polymers produced by D.H. Reneker triggered renewed interest in electrospinning (Reneker et al., 1996).

Ceramics and polymer fibers have been electrospun either in dissolved form or in the form of a melt. Literature shows that more than 100 polymers, in either dissolved or melt form have been electrospun into ultra-thin fibers, and approximately fifty different formulations of Polymers and their concentration in preferred solvents have been found ( Kelkar et al., 2008). There are also limited instances of processing of fibers from polymer melts and ceramics by electrospinning.

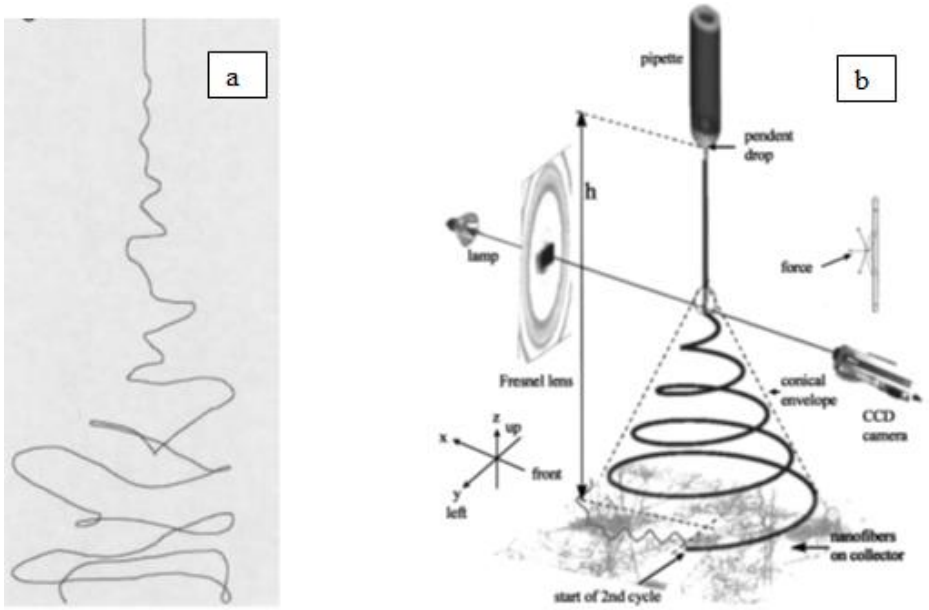


*Figure 1.3.* a) Bending Instability b) Bending cone formation study setup

Processing polymers in melt form has a significant disadvantage in that the electrospinning process must be carried out a in vacuum chamber. Electrospinning of ceramic fibers has also attempted, but due to the limited number of application specific formulations for ceramic nanofibers, the numbers of publications on electrospun ceramic nanofibers are also limited.

Electrospinning of polymer dissolved in solvent is simple to setup and is carried out room temperature in an open chamber. In order to successfully electrospin polymer solutions, the potential difference maintained between spinneret and grounded collector is of the magnitude of 1kVto 30kV. Care must be taken, during manipulation of the electrospinning setup because if any of these electrodes comes in contact with the operator, it may prove fatal due to the high voltage involved. Also since the electrospinning setup for dissolved polymers is in atmospheric conditions, there should be sufficient ventilation to carry away solvent fumes.

### 1.3.2 Process parameter in electrospinning

Drawing of sub-micron to nanometer size fibers has been achieved consistently using

electrospinning (without surface defects) by controlling processing parameters. The governing process parameters associated with electrospinning polymer solutions are viscosity, elasticity, conductivity, molecular weight, solution concentration and surface tension. These parameters are dependent on the inherent properties of solute and solvent such as molecular weight and cross linking of polymer chains etc., which are further influenced by temperature, time and humidity. Process parameters such as electric field, distance between spinneret and collector, rate of dispensing can be mechanized, however a sufficient amount of operator judgment is required in order to set the electrospinning device to the suitable conditions. Some researchers have tried to analyze the effect of these controllable parameters on the quality of fibers (shown in Tables 1.1(Greiner et al., 2007) and 1.2 (Z.-M. Huang et al., 2003)).

*Table 1.1* Parameters that affect the morphology of the electrospun fibers

| Polymer properties | Solution properties | Other properties |
|---|---|---|
| Molecular weight | Viscosity | Substrate properties |
| Molecular-weight distribution | Viscoelasticity | Solution feed rate |
| Glass-transition temperature | Concentration | Field strength |
| Solubility | Surface tension | Geometry of electrode(s) |
| | Electrical conductivity | Vapor pressure of the solvent |
| | | Relative humidity |

*Table 1.2* Controlling Parameters and characteristics of the electrospun fibers

| Controllable Parameters | Fiber Characteristics |
|---|---|
| A) Solution Parameters: Viscosity, Concentration Conductivity, Surface tension, Elasticity, Molecular weight | A) Structure: Diameter, Solid, hollow, ribbon, Surface roughness, with beads or pores |
| B) Process Parameters: Rate of dispensing, Potential difference, Distance between spinneret and grounded collector | B) Alignment: Random Non-woven, Aligned or Unidirectional |
| C) Ambient Conditions: Temperature, Humidity, Velocity of Air | C) Properties: Modulus, Shear strength, Glass transition temperature, Surface to weight ratio, Refractive Index etc. |

The diameter of electrospun fibers is important and highly influenced by the viscosity of the polymer solution. The relationship fiber diameter of polymer solutions at varying viscosities has been investigated(H. Liu et al., 2002). When cellulose acetate was dissolved in 50% of solution of acetone and dimethylacetamide, uniform diameter fibers were obtained over a range of viscosity 10.2 to 1.2 poise at room temperature.

In a study of Polyethylene Oxide in dilute ethano1, a viscosity in the range of 1-20 poise and surface tension between 35 to 55 dynes/$cm^2$ was found to be suitable for getting uniform diameter fibers. For a polymer solution, a useful electrospinning process consumes solution rather slowly. A consumption rate between 1 ml/hr to around 3ml/hr is typical and will depend on viscosity and rate of dispensing and direct affects the diameter of fibers produced (Teo et al.,

2006). Humidity and temperature are two factors that affect viscosity. Also, a wide range of viscosities have been found to be suitable for getting uniform diameter fibers. The fiber diameter is also a function of applied voltage. This means there should be some co-relationship between viscosity, voltage and diameter. However, very few references have been found that clearly indicate the relationship.

Deitzel et al have shown that diameter is directly proportional to square of concentration of the solution (Deitzel et al., 2001). Further it is found that the fiber diameter varies as cube of the concentration (Demir et al., 2002).Thus it can be broadly concluded that electrospun fiber diameter is directly proportional to viscosity as shown in Figure 1.4 (S. H. Tan et al., 2005). It is very important to note that there is critical a viscosity for polymer solutions where if viscosity is lower than the critical value there will be no fiber formation (only spraying of droplets). A processing map summarizes the effects of solutions properties and processing conditions on the electrospun nanofiber morphology. Polymer concentration, its molecular weight and, electrical conductivity of solvents were found as dominant parameters to control the morphology (as shown in Figure 1.4 (S. H. Tan et al., 2005)).

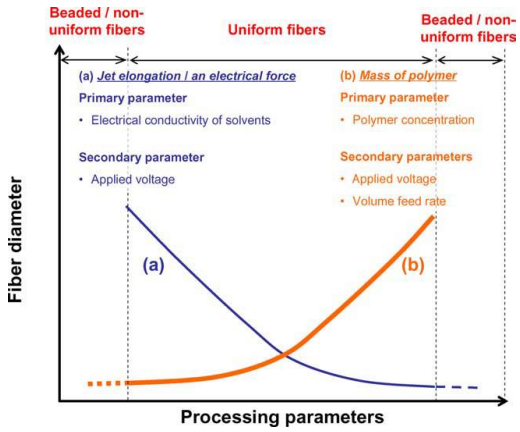


*Figure 1.4.* Processing map obtained based on the systematic parameter study: (a) jet elongation/an electrical force (affected by electrical conductivity of solvents, applied voltage), (b) mass of polymer (affected by polymer concentration, applied voltage, volume feed rate)

If viscosity is more than the permissible range, clogging of the spinneret is evident. In the discussion relating diameter to viscosity, there is a passing reference of the influence of applied voltage. Applied voltage influences the diameter of electrospun fibers, and must be a controlled parameter in order to obtain fibers with smallest uniform diameter. Some references have inferred that higher the applied voltage, the larger the fiber diameter. That is not true in all situations such as when polymer solution is fed to the spinneret with a controlled rate using dispensing pump. If the rate of dispensing is controlled; increasing applied voltage usually results in higher force being exerted on the charged jet, resulting into higher whipping amplitude causing more elongation and evaporation of charged jet resulting in decrease in fiber diameter. Voltage is used as regulating parameter in conjunction with the distance between spinneret and grounded collector to get uniform diameter fibers. If higher temperature electrospinning processes are used for polymer solutions such as polyurethene, relatively high solution viscosity must be maintained in order to yield appropriate fiber structure although no relationship between viscosity and fiber diameter was observed. (Demir et al., 2002).

### 1.3.3 Characterization

The characterization of electrospun fibers can be segregated into four broad categories mechanical, chemical, physical and geometrical. Mechanical characterization is used to determine mechanical properties of individual ENFs, but is by far the most difficult and hence is the least investigated area. Efforts in mechanical characterizations of ENFs are based on the methodology used in the determination of mechanical properties of carbon nanotubes. Mechanical testing of individual carbonized nanofibers was performed using AFM. The bending modulus was found by a mechanical resonance method. The average modulus of the fiber was observed to be 63 GPa (Zussman et al., 2005). Wong et al demonstrated the use of AFM to deflect a CNT in order to determine bending strength and Young's modulus (Wong et al., 1997). There has been fabrication of micro devices to determine mechanical properties of CNT'S using SEM, TEM, & AFM(Demczyk et al., 2002). However there is no report on tensile properties (test) of single ENFs.

Molecular orientation, bonding, crystal structure and chemical properties are the areas of research associated with chemical characterization. Investigations of these properties are accomplished by using equipment like FTIR, NMR, WAXD, SAXC, XPS & ATR analyzers. And NMR study of collagen and a PEO blend of electrospun fibers was useful to identify inter molecular interaction due to formation of hydrogen bonds between them(L. Huang et al., 2001). SAXC was used to recognize macromolecular orientation in ENFs using optical bifringence. Molecular orientation of Styrene- Butadiene-Styrene was identified while studying bifringence using an optical microscope(Hao Fong et al., 1999). To determine the surface chemical properties of nanofiber membranes water contact angle analysis is useful. In a study on an electrospinning of polymer nanofibers with specific surface chemistry concentration of fluorine

on the surface of PMMA–TAN ENFs, it was shown that the electrospun material was twice as dense as the bulk polymer(Deitzel et al., 2002).

Physical characterization methods such as electrical conductivity, thermal properties and diffusion of air and water have been used to study nanoporous, electrospun membrane useful in filtration applications. During thermal analysis conducted for PET and PEN nanofibers, it was found that the melting temperature was unaffected but there was a decrease in Tg (Glass transition Temperature) / Tc when nanofibers were compared to the bulk polymer properties(KIM et al., 2000). PAN electrospun fibers exhibited high resistance but considerable improvement in conductivity was observed when they were graphitized (Yu Wang et al., 2002).

A dynamic moisture vapor permeation cell (DMPC) was used to determine air, vapor permeation through ENFs mats and melt blown thermoplastic polyurethenes. The electrospun fiber mate had over 100 times smaller pores and hence better resistance to air flow than melt blown mats (Gibson et al., 1999).

The characterization of electrospun fibers in this research is related to study of geometrical properties including, determination of fiber diameter and its variation in nonwoven mats, morphology in terms of cross-section (circle, flat, coaxial) surface texture and porosity, Geometrical properties are measured by using SEM, field emission SEM, TEM & AFM. Also TEM can use as spun electrospun fibers because it does not need fibers to be in a dry state as in SEM. AFM can accurately measure fiber diameter. An AFM tip is moved over on cross – over of fibers. The top surface of the lower fiber is considered asa reference plane & the vertical distance traveled by the tip as it reaches the top surface of upper fiber is the diameter of the top fiber(Morozov et al., 1998). Porosity of electrospun nanofiber membrane is useful in filtration, tissue template and protective clothing applications can be assessed by a capillary flow parameter

(Stillwell, 1996). It can be demonstrated that porosity is extremely small as compared to the diameter of fibers.

### 1.3.4 Surface defects of electrospun fibers

One of the observed defects in electrospun nanofiber is beads on the fiber surface. Beads are lumps concentrated at certain locations on the surface of the fibers. These beads are formed due to concentration variation and hence viscosity non-uniform of the polymer solution. Higher polymer concentrations result in smoother bead free fibers (Hao Fong et al., 1999). SEM images (Figure 1.5 ) clearly indicate that with the increase in concentration from 1% by wt. ( i. e at 13 centipoises viscosity) to 4% by wt. of PEO (i.e at 1250 centipoise viscosity) result in decrease in the percentage of bead and the dispersion of beads, however, the diameter of beads is as concentration increases. TEOS sol-gel electrospinning the formation of beads is exactly opposite what occurs in the polymer solution case i.e. at lower viscosity there is less bead formation. Thus the bead formation may be dependent on polymer solution properties other than concentration and viscosity.

Other researchers have found that bead free fibers are obtained by reducing the surface tension of the polymer solution. In this case, surface tension is not only s function of polymer concentration, but also due to the solvent. . The variation in surface tension due to usage of different solvent has been shown in several studies (Hao Fong et al., 1999; H. Liu et al., 2002). When acetone and dimethylacetamide (DMA) are independently used as solvents with cellulose acetate, the surface tension was found to be in the range of 23.7 dyne/$cm^2$ to 32.4 dyne/$cm^2$ but when DMA is used alone as a solvent, it only produced beads when 5 to 8% wt. of cellulose acetate in acetate was used. When the solvent was combination of acetone and DMA in proportion of 2:1 with a cellulose acetate concentration in range of 15-25 wt. % continuous

smooth fibers were obtained. When the solvent ratio was adjusted to a 10:1 proportion of acetone to DMA with 15 wt.% cellulose acetate, 700 nm diameter, smooth fibers were produced. Further, the innovative method to produce bead free smooth fibers was proposed by (Zong et al., 2002) with the use of salt as a filler in proportion of 1% by weight to produce smooth uniform diameter electrospun fibers.

The reason for using salt as filler to produce smooth bead-free fibers was attributed to an increase in charge density on surface of polymer droplet emanating from the spinneret as compared to when no filler was used. This increased charge density resulted in higher dragging force due to applied electric field causing greater whipping amplitude to produce longer & thinner electrospun fibers. An increase charge density by using a higher potential difference wil cause less of impact on bead formation than the use of 1% by weight of salt and increase in roughness in the electrospun fibers (Deitzel et al., 2001) as shown in Figure 1.7(Deitzel et al., 2002). Improvement in properties of nanofibers is also indeed dependent on diameter, smoothness and uniformity. As solution viscosity increases, bead formation in the fibers will decrease and form straight fibers as shown in Figure 1.5(H Fong et al., 1999) and Figure 1.6(Teo et al., 2006).


*Figure 1.5.* SEM photographs of ENFs from different polymer concentration solutions

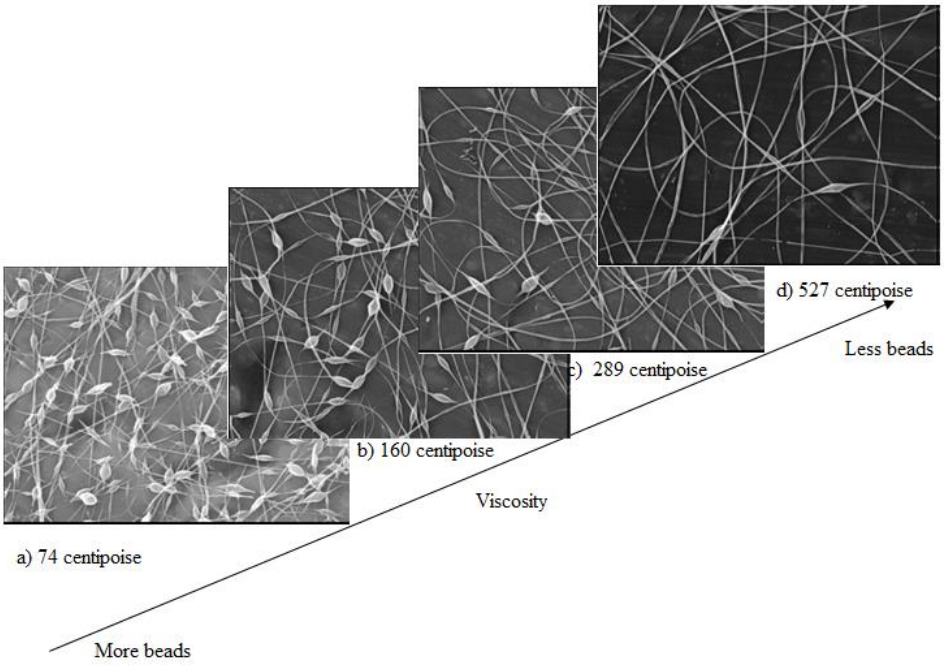


*Figure 1.6.* Variation of bead density with change in viscosity of polymer solution

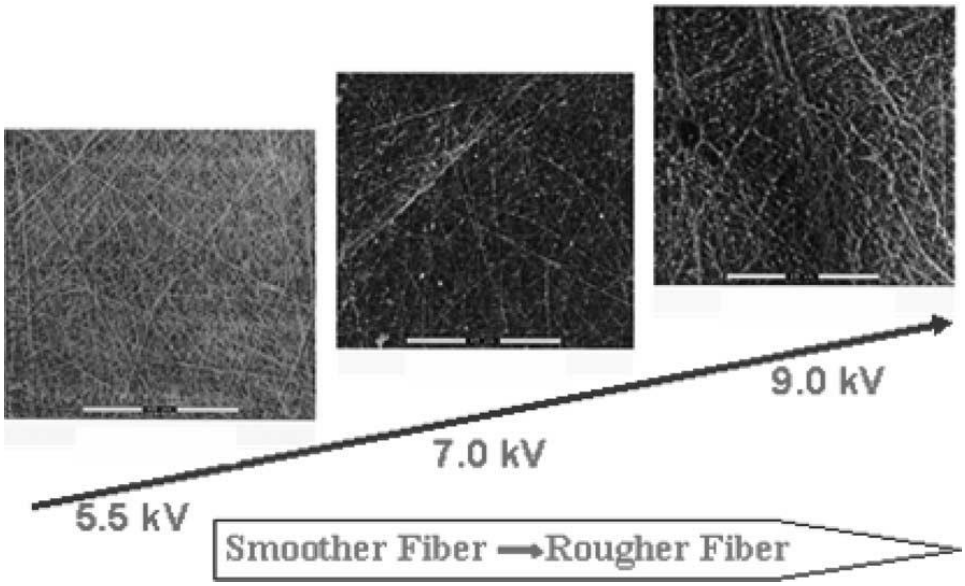


*Figure 1.7.* SEM photographs of PEO nanofibers electrospun under different electrical potentials

### 1.3.5 Surface treatment of nanofibers

Previously reported studies indicated thatSiO2 nanofibers can be prepared to be morphologically uniform with bead -free smooth surface. SiO2 nanofibers with diameters of ~500 nm were prepared by selecting tetraethyl orthosilicate (TEOS) as an alkoxide precursor, polyvinylpyrrolidone (PVP) as the carrying polymer, N,N-dimethylformamide (DMF)/acetic acid (HAc) as the mixture solvent, and pyrolysis temperature between 600 $^{0}$C and 1000 $^{0}$ C. The $SiO_2$ nanofibers were structurally amorphous, and retained the fiber morphology even when subjected to vigorous ultrasonication (Y. Liu et al., 2008). Electrospun nano-scaled glass fibers; and their reinforced dental composites exhibited substantially improved mechanical properties(Gao et al., 2008).Nonetheless, due to the complexity of TEOS reactions during the sol–gel process including hydrolysis and condensation shown in Figure 1.8, the need for precise control of the gelation extent of TEOS before, during, and after electrospinning, and the retention of the nanofibers morphology throughout the process remains as technological challenges.

Furthermore, for the application of reinforcing composites, the surface of electrospun $SiO_2$ nanofibers is preferably rough in order to obtain the physical interlocking between the nanofibers and the polymer matrices. This structure leads to improved mechanical properties and is particularly important when the composites are under load/tension(Xu et al., 2006).

The hierarchical electrospun $SiO_2$ nanofibers with optimal surface-roughness and/or porosity outperform $SiO_2$ nanofibers without $SiO_2$ nanoparticles for reinforcement of composites. Also the hierarchical electrospun $SiO_2$ nanofibers have high specific surface areas.(Wen et al., 2010)

Recent studies have indicated that continuous $SiO_2$ nanofibers with diameters of ~400 nm can be prepared through electrospinning a spin dope containing an alkoxide precursor of SiO2 followed by pyrolysis at high temperature. When the electrospun glass nanofibers (EGNFs) with diameters of about ~400 nm were incorporated (at very low mass fractions of 0.5 and 1%) into epoxy resin for reinforcement and/or toughening purposes; two silane coupling agents with respective end groups of epoxy and amine including 3-glycidoxyl-trimethoxysilane (GPTMS) and 3-aminopropyl triethoxysilane (APTES) were selected for surface treatment (shown in Figure 1.8)(Chen et al., 2012). The surface treatment of EGNFs with GPTMS or APTES would improve the interfacial bonding strength between the fibers and the matrix, and also facilitate the uniform dispersion of EGNFs in the resin matrix. The effects of incorporation of EGNFs and the different silanization treatments on mechanical properties of the resulting nano-epoxy composite resins were investigated(Chen et al., 2012)

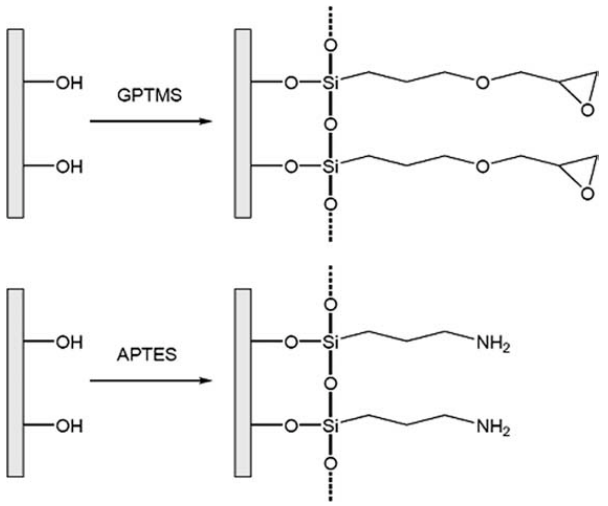


*Figure 1.8.* Schematic diagrams showing the reactions between silane coupling agents (of GPTMS and APTES) and silanol (Si-OH) groups on the surface of glass fibers (of EGNFs and CGFs)

In general, the silanized EGNFs with epoxy end groups (G-EGNFs) showed a higher degree of toughening effect, while the silanized EGNFs with amine end groups (A-EGNFs) showed a higher degree of reinforcement effect. The study suggested that electrospun glass nanofibers could be used as reinforcement and/or toughening agent for making innovative nano-epoxy composite resins, which would be further used for the development of high-performance polymer composites.

In order to investigate the effect of sintering temperature, electrospun fibers were heated at three different temperatures (300 $^0$C, 600 $^0$C and 900 $^0$C). The result shows an around approximately 50 % reduction in diameter of TEOS fibers after sintering at the two higher temperatures. This reduction is due to evaporation of solvent that is accompanied with physical, chemical and structural changes (Shendokar et al., 2008). Thus an increase in the sintering temperature will decrease the diameter of the nanofibers. However increasing temperature beyond 900 $^0$C was made nanofibers highly brittle and therefore 600 $^0$C was selected as the

optimum temperature to evaporate the water and ethanol solvent from the TEOS nanofibers and create more roughness on the surface.

## 1.4 Failure of Fiberglass Composites

### 1.4.1 Failure mechanisms

Several progressive damage and failure models take place in composite laminates. Macromechanics based models either combines fundamentally different failure mechanisms in a polynomial approximation or use separate equations to explain various failure modes. Regardless of whether a failures model is based on micromechanics or macromechanics, it is preferred that any model have chosen should have a on physical basis, which either directly or indirectly relates to the mechanisms of failure. Fiber and matrix failure and delamination are briefly reviewed in this section. When a lamina undergoes unidirectional static loading, local failure occurs depending on the direction of static loading. Local failure originates from the parts of the lamina such as the fibers, the matrix, and the interface. Interaction among local failure modes occurs during multi-axial loading as shown in Figure 1.9 (Talreja, 2006).

The failure modes may occur in composite lamina under longitudinal tension, transverse tension, longitudinal compression, transverse compression or shear. Figure 1.10 shows a composite lamina under longitudinal tension. During longitudinal tension, the load is carried by the fibers until fiber breakage. Fiber breakage is represented by the letter ‘a’ in Figure 1.10. In practice, fiber strength is not a unique value, however it follows a statistical distribution in which a few fibers break at lower stress values (Cook et al., 1964; Talreja, 2006). When a fiber breaks, it cannot sustain normal stress at the broken ends. Shear occurs at the fiber-matrix interface, which transfers the stress to the surrounding matrix.

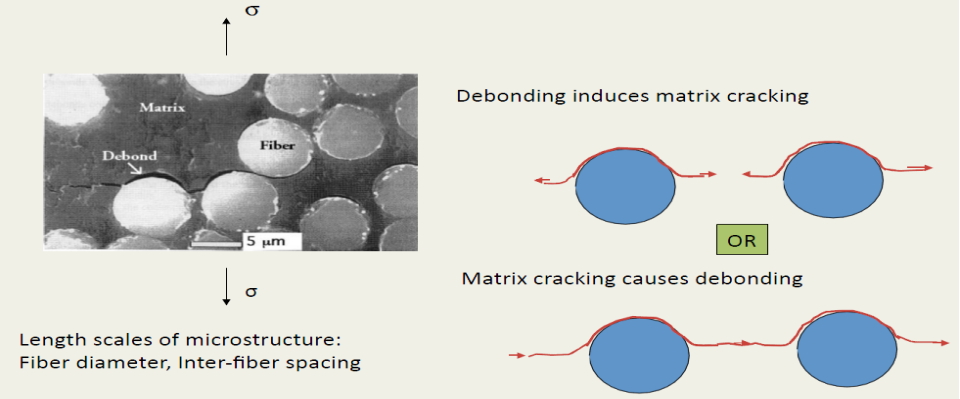


*Figure 1.9.* Failure of glass fiber reinforced polymeric composites

As a result, fiber breakage causes stress concentrations to be present at the voids created by the broken fiber, high shear stress concentrations in the matrix near the fiber ends, and an increase in the normal stresses carried by the unbroken fibers. The local shear stress concentrations at the fiber-matrix interface cause local failure due to total debonding of the broken fiber from the surrounding matrix. The high local stress concentrations near the voids caused by fiber breakage cause initiation of microcracks, which lead to failure (Cook et al., 1964).The increase in the stress carried by unbroken fibers causes additional fibers to break leading to more fiber-matrix debonding, more voids and microcracks, and more stress carried by each unbroken fiber as shown in Figure 1.9.

Further, the longitudinal stress concentration ahead of the crack tip, the transverse stress and in-plane shear stresses reach relatively high values ahead of the crack tip (Amaya, 2012). The stress concentrations parallel to crack propagation are capable of debonding the fibers from the matrix even before the unbroken fibers fail in tension(Cook et al., 1964). The statistical distribution of fiber surface flaws do not always cause the fibers fail in the areas debonded from the matrix, which leads to broken fibers being pulled out of the surrounding matrix. Fiber pullout is denoted by the letter ‘b’ in Figure 1.10. If pullout does not occur after fiber breakage in an area outside the crack plane, the broken fiber will act as a bridge between two surfaces of the matrix

crack. Multiple fiber break points can form parallel cracks orthogonal to the fibers that cause significant deformation of the matrix between cracks if the cracks are bridged by a broken fiber shown by the letter ‘c’ in Figure 1.10(Gotsis et al., 1998).

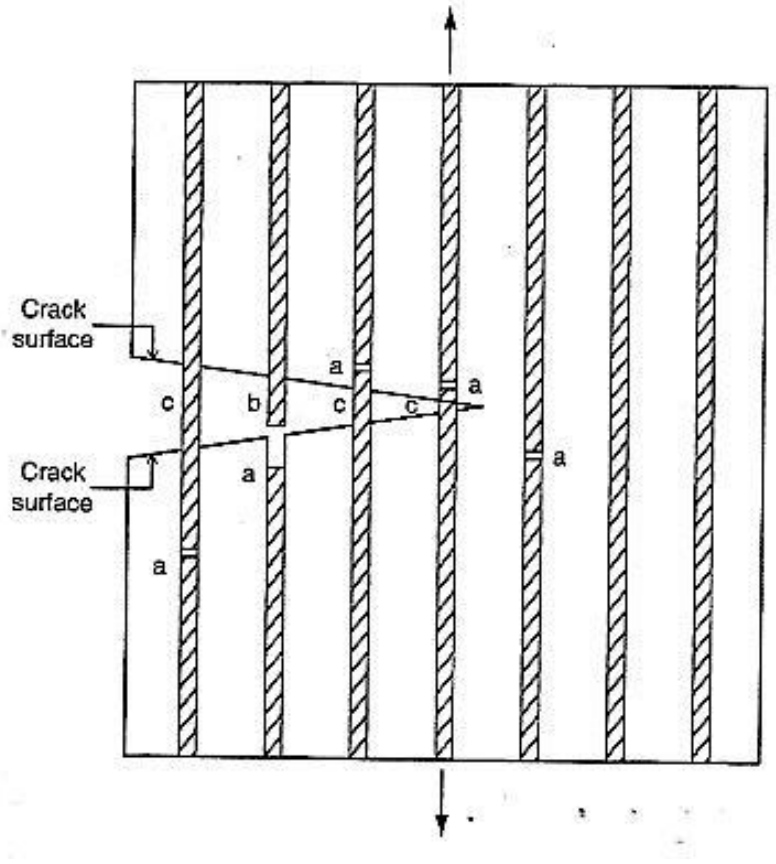


*Figure 1.10.* Schematic representation of fiber pullout and matrix bridging by broken fibers (a) fiber breakage; (b) fiber pullout; (c) matrix bridging

Theoretical failure models based on fracture mechanics attempt to link the local stress concentrations and local failure modes with failure of the composite laminate. A composite lamina under transverse tension is shown in Figure 2.10. When transverse tensile load is applied to a unidirectional composite laminate, the fibers are not the principal load carrying members. The radial stress is tensile and about 50% higher than the applied stress near the fiber-matrix interface, which cause cracks normal to the loading direction that develop at either the fiber-

matrix interface or in the matrix, both shown in Figure 1.10(Gotsis et al., 1998).

### 1.4.2 Micromechanics Models

A theory of heterogeneity of composite laminates was based on the assumption that the reinforcing material has much higher elastic moduli than the matrix material and the thickness of the reinforcing elements and distance between them were small (Bolotin, 1965). Bolotin's extension of micromechanics theory to layered media with random imperfections indicated that macroscopic homogeneity assumptions are not valid under certain conditions. Since the early investigations into heterogeneity, there have been several investigations involving micromechanics models and different methods accounting for material heterogeneity have emerged as a result.

The mechanics of composite behavior have been studied since the early sixties. Research activities on composite mechanics were reviewed by C. C. Chamis 1984 The various theories reviewed consisted of netting analysis, variational models, elasticity, mechanics of materials, self-consistent models, statistical, discrete element, semiempirical methods, and theories accounting for microstructure(C. Chamis et al., 1968). The early models included basic assumptions that the ply is, linearly elastic, macroscopically homogenous and orthotropic. The fibers and matrix were assumed to be linearly elastic, homogenous, and free of voids. Complete bonding at the interface between fibers and matrix was assumed. The fibers were assumed to be regularly spaced and aligned (no microbuckling or kinking). The residual stresses were neglected.

Mechanical or thermal loads may cause the formation of microcracks before any detectable change at the macroscale. Final failure of the lamina can occur due to accumulation and the propagation of several microcracks. Fracture mechanics based models analyze the stress

distribution around the microcrack tips while taking into account spatial distribution of the microcracks, bridging effect of fibers, and interaction between cracks. Methods predicting cracking in composites typically use a stress transfer function to satisfy both the equilibrium and the stress boundary conditions (McCartney, 2002)

Microbuckling and kinking theories have been proposed to account for the observation that the compressive strength of fibers is lower than their tensile strength. The rule of mixtures is a method of estimating the mechanical properties of a composite laminate as a function of the volume fraction of the fibers and matrix. The multicontinuum approach to micromechanics modeling has been used more widely due to improvements in computational modeling. The different types of micromechanics based models attempt to directly describe the local failure phenomena and relate them to lamina and structural failure.

#### 1.4.2.1 Fracture Mechanics

Fracture mechanics is concerned with the initiation and growth of critical cracks that could finally lead to catastrophic structural failure. In fiber-reinforced composite laminates, critical cracks emerge at areas of manufacturing defects such as micro-voids or at localized damages caused by low energy impacts or delaminations at edges caused by static or fatigue loading. The resistance to crack growth is considered to be important to achieving damage tolerance. The structural fracture process depends on many parameters including laminate configuration, fiber volume ratio, constituent stiffness, strength, hygrothermal properties and the fabrication process(Harris et al., 1986). The linear elastic fracture mechanics approach is based on stress intensity factors, which are functions of applied stress, crack length, and a geometric function that depends on crack length, location, and mode of loading.

An existing crack may propagate in an unstable manner when the stress intensity factor reaches a critical level. Standard testing methods are used to determine the critical stress intensity factor, or fracture toughness for metals. No standard method is currently available for fiber-reinforced composite laminates (Cook et al., 1964). Pre-notched specimens are typically used to experimentally determine the stress intensity factors. The load-crack opening displacement (COD) curves obtained from notched specimen tests become nonlinear or even discontinuous as local damage occurs at the notch tip. The nonlinearity presents difficulty in determining the load corresponding to the critical stress intensity factor. The stress intensity factor was calculated using a graphical method (Harris et al., 1986). A line through the origin with a slope equivalent to 95% of the initial slope of the load- COD curve intersects the load-COD curve itself at the load corresponding to the critical stress intensity factor.

In addition to stress intensity factors, strain energy release rates are considered a measure of fracture growth resistance, particularly when considering delamination. Failure criteria are sometimes established in the form of stress intensity factors or strain energy release rates. Fracture toughness is dependent on loading modes necessitating the use of mixed-mode delamination criteria. The mechanisms that determine fracture mode are not well understood (Bui, 2011).

*1.4.2.1.1 Modes of fracture*

The type of loading applied to the composite will determine mode of fracture. The in-plane properties of a composite laminate can be easily adjusted; however the inter-laminar regions are more difficult to strengthen. Inter-laminar regions are matrix rich with lower fiber content than the in- plane regions, making their properties dominated by the isotropic matrix material. Although attempts have been made to increase inter-laminar toughness by stitching the

layers together (O'Brien, 1998; Wood et al., 2007)or adding support structures (P. Tan et al., 1997), in general, the only option is to use a tougher matrix. Inter-laminar cracks reduce the stiffness and fatigue life of composite materials and introduce more buckling failure modes. Damage in composite structures is difficult to detect and repair and therefore fracture toughness must be well understood to predict stability and service life.

Figure 1.11 shows that the cracks can grow under three separate modes (Slager, 2007). Mode I (opening mode) occurs due to a tensile stress normal to the plane of the crack. Mode II (sliding mode) occurs due to a shear stress perpendicular to the crack front. Mode III (tearing mode) occurs due to a shear stress parallel to the crack front. Mode II Inter-laminar fracture occurs in laminated FRP because crack growth is confined by the adjacent fiber layers. Even though the matrix has been shown to crack in mode I at the microscopic scale (Sankar et al., 1997), it is still considered a mode II fracture when studied as a macroscopic process. Mode I inter-laminar toughness is tested using the double cantilever beam (DCB) test according to ASTM D 5528.

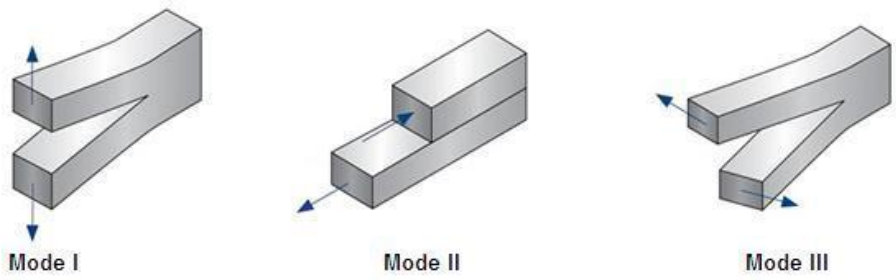


*Figure 1.11*. Modes of fracture in the composite

There are multiple Mode II tests that have been considered for standardization, but none has been adopted by the ISO(Davies et al., 1998; Strong, 2008). The lack of an international standard is partially due to disagreement among regional standards organizations as to which mode II test is the best, with ASTM, ESIS, and JIS each championing a different one. O'Brien

has published an explanation of this disagreement.(Davies et al., 1998) These organizations have different mandates, and different scopes of practice, which often leads to conflict. Mode III is also not standardized, in this case because of the difficulty of generating mode III separation.

**1.5 Methods of Improving Delamination Resistance**

Delamination resistance can be improved by using methods such as toughened matrix materials, laminate design with stacking sequence and ply thickness, stitching through the thickness, 3 – D braiding stitches, Z – pinning, edge cap reinforcement, and tough adhesive interleaf.

*Table 1.3* Method to improve delamination resistance

| | |
|---|---|
| Stitching through the thickness | 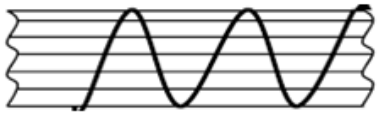 |
| 3D braiding (no distinct plies) | 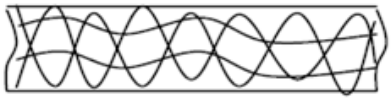 |
| Z – pinning | 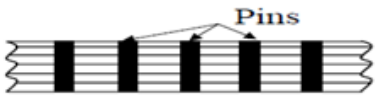 |
| Edge cap reinforcement | 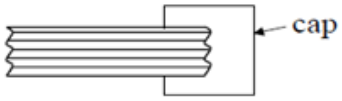 |
| Tough adhesive interleaf |  |

**1.6 Review on Improvement of Short Beam of Fiber Reinforcement Composite**

Pipes and Pagano shown have significant inter-laminar shear stresses are required to allow shear transfer between the layers of the laminate. The inter-laminar shear stress was found to be an edge effect and is a function of laminate thickness. There is strong evidence of a

singularity in the inter-laminar shear stress at the intersection of the interface and free-edge. High stresses in the neighborhood of the free edge may be expected to cause delamination of the laminate under fatigue loading. All such high stresses in the neighborhood of the free edge may be expected to cause delamination of the laminate and therefor it is necessary to understand the effects of interleaved nanofibers in order to obtain accurate prediction of inter-laminar stresses in the laminates with and without nanofibers (Pipes et al., 1970).

A review of the current techniques for characterizing inter-laminar fracture in terms of their configurations, testing methods, and data reduction include the mode I double cantilever beam (DCB) test for measuring $G_{IC}$ and the end notched flexure for measuring Also, the mode II end loaded split (ELS) test, the mixed mode delamination characterization and the mixed mode bending (MMB) test have been reviewed. The split cantilever beams (SCB) were given. Specimens has been proposed as a mode III test, however recent analysis has shown that this type of specimen delaminates in a combination of modes II and III. Therefore, to date no recommended mode III test is available. Lastly, techniques for characterizing inter-laminar fracture by fatigue were reviewed that include the delamination growth method and the delamination onset method. The work done using both methods details the advantages of the onset method versus the growth method.(Martin, 1991)

An attempt was made to enhance composite inter-laminar toughness by adding different type of microfibers into matrix. The effect of adding microfiber to the matrix resin on the fracture toughness of composite was evaluated for selected microfiber at low weight fractions of 1 to 3 wt.% and significant increases in toughness( from 75 to 108% ) were observed due to microfiber inclusion.(Youjiang Wang et al., 1995).The effective or apparent critical strain-energy release rate for stitched laminates have also been published were presented. Stitching results in

an excellent improvement in $G_{II.}$ The apparent $G_{II}$, was 5 to 15 times that of the unstitched laminates, depending on the stitching parameters. There appears to be an optimum stitch density at which the toughness will be maximized. The critical strain-energy release rate increases with an increase in crack length as more and more stitches bridge the delamination(Sankar et al., 1997).

A new transverse shear force-deformation relationship for a metallic z-rod is obtained by using classical beam theory and modeling its surrounding matrix as linearly elastic, rigid–perfectly plastic or linearly elastic–perfectly plastic springs. The bridging traction provided by a metallic z-rod to the mode II delamination toughness is assumed to be only the shear force carried by a z-rod created by the relative slippage between two substrate beams in an end-notched flexure (Liao et al.) specimen, whereas the longitudinal sliding friction is assumed to make negligible contribution to the bridging traction. Mode II strain energy release rate (Yu Wang et al.) is employed to evaluate the influence of the metallic z-rods on the interlaminar fracture toughness of end-notched flexure (Liao et al., 2008) specimens. A parametric study of ENF specimens reinforced with the z-rods is conducted to demonstrate the effect of the new bridging mechanism by the metallic z-rods on the mode II delamination toughness(P. Tan et al., 1997).

The interlaminar fracture toughness ($G_{IC}$) of braided and knitted composites are higher than traditional composites by factors of more than two and four, respectively. Toughening in these textile composites was caused by extensive crack branching as the interlaminar crack was forced to follow a tortuous path through the complex fiber architectures. The $G_{IC}$ values of the composites reinforced in the through-thickness direction by weaving or stitching were higher than traditional composites by factors of nearly two and three, respectively, with the main

toughening mechanism being crack bridging by the through-thickness binder yarns/stitches (A. D. Kelkar et al., 2006; Mouritz et al., 1999).

Uniform distribution of fibers in the stitch roving, absence of resin rich regions and reduced fiber damage result in increased in-plane tensile, lap shear, flexural, transverse shear and impact strengths. The effect of stitching on Mode I delamination toughness ($G_{IC}$) of glass/polyester laminates has been investigated by a performing double cantilever beam (DCB) test. It is observed that stitching increases the Mode I delamination toughness up to 20 times higher than that of an unstitched specimen.(Velmurugan et al., 2007).

A study of mixed mode II + III fractures of carbon/epoxy laminates was performed using six-point bending plates with cross-ply lay-up and the standard 0/0 interface. Finite element analyses (FEA) were performed to select specimen geometries suitable for measuring the initiation critical strain energy release rate $G_c$ over a wide range of mode mix ratios. The main difficulties were non-uniform distributions of $G_{II}$ and $G_{III}$ and considerable geometric non-linearity. Nevertheless, experimental results suggested a quasi-linear evolution of $G_c$ with the $G_{III}/G$ mode mix ratio consistent with previously measured $G_{IIc}$ values and expected $G_{IIIc} > G_{IIc}$ (De Morais et al., 2008).

Over the past 10 years there has been significant progress, with benefits such as improved delamination resistance, damage tolerance, through-thickness stiffness and joint strength being demonstrated. The detrimental effects of z-pinning on the in-plane mechanical properties, such as lower elastic modulus, strength and fatigue performance, have also been investigated. In general, the improvements to the interlaminar properties achieved by z-pinning out-weight the reductions to the in-plane mechanical properties(Mouritz, 2007)

The reinforcement potential of a glass fiber reinforced vinyl ester composite with infused carbon nanotubes was examined and the effect on interlaminar shear strength was investigated. Several sidewall functionalized nanotube derivatives were also prepared in order to obtain high dispersion and matrix bonding. Carbon nanotube enhanced vinyl ester/glass fiber composites were fabricated by a vacuum assisted resin transfer molding process. Over coating the glass fiber weave with nanotubes and processing modification led to enhancement of the interface properties. A maximum of 45% increase in shear strength was observed for specimens containing 0.015 wt.% carbon nanotubes in the mid-plane ply when compared with over control sample  without carbon nanotubes (Zhu et al., 2007).

The effects of load rate on mode-I fracture behavior of laminated composites were studied using quasi-static experiments. The experiments were conducted on laminated beam type specimens with inserts to simulate delamination. The results showed an increase fracture toughness for the corresponding increase in crack extension rate for the Toray Carbon Unitape samples and a scattered response for Newport Fiberglass samples (Nandakumar et al., 2009).

Radially-aligned CNTs grown in situ on the surface of fibers in a woven cloth provide significant three-dimensional reinforcement, as measured by Mode I interlaminar fracture testing and tension-bearing experiments. Aligned CNTs bridge the ply interfaces giving enhancement in both initiation and steady-state toughness, improving the already tough system by 76% in steady state (more than 1.5 $kJ/m^2$ increase). CNT pull-out on crack faces is the observed toughening mechanism, and an analytical model is correlated to the experimental fracture data. In the plane of the laminate, aligned CNTs enhance the tension-bearing response with increases of: 19% in bearing stiffness, 9% in critical strength, and 5% in ultimate strength accompanied by a clear

change in failure mode from shear-out failure (matrix dominated) without CNTs to tensile fracture (fiber dominated) with CNTs (Wicks et al., 2010)

A unified framework for the development of various 2D mixed-mode delamination criteria has been developed, and due to its generality, an extension can also be made for the development of 3D criteria. Limited by its mathematic form, each fracture criterion is able to faithfully describe only certain shapes of fracture locus of laminated composite materials. Based on knowledge about the interlaminar fracture behavior of laminates, an appropriate fracture criterion needs to be chosen by users when delamination growths are simulated by fracture mechanics or the cohesive zone approach can be used via finite element simulation packages. Once a correct mathematical form is chosen, the use of more parameters generally leads to more better descriptions of the fracture behavior. The modified B-K criterion can consistently reproduce the linear non-interaction criterion (also validated against experimental data). The quantitative and qualitative improvements are observed in the description of inter-laminar fracture behavior of laminates, especially for the fracture locus featuring a monotonic decrease of mode I toughness with increasing mode II. The modified B-K criterion may therefore be an alternative to the case where the original B-K criterion shows its limitations (Bui, 2011).

Less research has been done on short beam/fracture toughness of plain weave woven fiberglass laminate composite. The available literature related to high strength fiberglass polymer composite provides data for damage mechanics, crack initiation, progressive damage and the inter-laminar shear stress. However the de-bonding of the ply laminates of plain weave woven fiberglass composite leads to delamination. Further, use of three dimensional textile structure composites (3DTSCs) such as, the 3D angle-interlock woven composite (3DAWC) under cyclic bending loading has shown substantial improvement in inter-laminar strength, modulus and

delamination properties. 3-D braided composite have shown improvement in the tensile fatigue with variation in the braided angle. In addition, over-coating the glass fiber weave with functionalized carbon nanotubes and processing modification led to further enhancement of interface properties. The radially-aligned CNTs grown in situ on the surface of fibers in a woven cloth provide significant three-dimensional reinforcement and significant improvement in inter-laminar strength of the composite. The literature review gives very little insight on the short beam improvement of plain weave woven fiberglass composite. Thus a detailed analysis the of failure mechanisms in plain-weave woven fiberglass polymer composite with and without interleaved TEOS nanofibers is the subject this dissertation research.

**1.7 Finite Element Modeling and Analysis**

Due to the large variety of material systems available in composite materials, and, the complex geometrical shapes available for composites, experimental characterization is tedious time consuming, and a very expensive process. In order to validate the experimental results, an analytical model is required and hence finite element analysis is used as an efficient method for modeling, analysis and simulation. The importance of the numerical simulation is partly due to the difficulty in conducting tests with special configurations or observing the occurrence of internal damage at different loading levels.

The response of a finite width composite laminate under uniform axial strain is treated through the application of classical elasticity theory. Finite-difference solution techniques are tailored to obtain solutions for stresses and displacement throughout the region. The results for material properties such as the high modulus graphite-epoxy composite system are presented that explain the mechanism of shear transfer within a symmetric laminate.(Pipes et al., 1970)

The properties of composite lamina can be obtained using simplified micromechanics equations for strength, fracture toughness, impact resistance, and environmental effects developed by C. C. Chamis 1984.

Ishikawa and Chou proposed three models to analyze woven composites: the mosaic model, the fiber undulation model and the bridging model. These models were known as laminate theory models since they basically assumed that the classical laminate theory was valid for every infinitesimal piece in the repeating region of the woven lamina(Ishikawa et al., 1982). The fiber undulation model is an advanced model that was used to understand considered for fiber undulation in the loading direction. The two dimensional extension to this model was introduced by Naik and Ganesh (Naik et al., 1992).

Raju and Wang considered tow continuity along both fill and warp direction(Raju et al., 1994). Conventional finite element analysis of textile composite structure is impractical due to their complex microstructure a global/local methodology with special macro-elements as an alternative method to evaluate the elastic properties of woven composite using finite element analysis has been developed. Global /local finite element analysis was used to study the stress distribution in a small portion of a structure in great detail(Whitcomb, 1991).A finite element model as well as analytical solution for determining elastic properties of twill woven composite was proposed by Chaphalkar and Kelkar(Chaphalkar et al., 1999).

A review that provide an estimation of transverse or inter-laminar stresses in laminated composite plates and shells for both analytical and numerical methods has been published. The review compares numerical methods, finite element methods, as well as other methods like the finite difference method. Aspects considered include the effects of variation in geometric and material parameters, transverse shear and normal deformation, interface stress

continuity and the influence of -interfacial bonding on the accuracy of prediction of transverse or interlaminar stresses(Kant et al., 2000).

The damage behavior of FRP is simulated by finite element analysis using an anisotropic damage model based on damage mechanics and used to predict microscopic damage propagation in woven fabric composites(Zako et al., 2003).

Progressive failure analysis was conducted for the cross-ply and quasi-isotropic laminates subjected to axial extension. Stresses and strains are calculated by the 3-D finite element method based on the generalized layer-wise plate theory (GLPT) in order to consider the local effect near free edges. The types and size of damage in composite laminates are predicted in the failure analysis that consists of a set of failure criteria and property degradation models for each mode of failure. In the case of matrix cracking, the macroscopic stiffness reduction model based on the shear-lag method is introduced to the finite element method in order to consider the nonlinear reduction of stiffness at each strain level(Zhang et al., 2009).

The inter-laminar stresses are analyzed by combining the first shear theory with the layer-wise theory method. The plate is subjected to a uniform axial strain and is studied with the simplified displacement field. Using the simplified displacement field, the equations of the finite element method are developed by the principle of virtual work and the amount of calculation is reduced by using the linear element(Yang et al., 2013).

Goodsell and Pagano approximate elasticity solutions for the prediction of displacement, stress, and strain fields within the m-layer for symmetric and balanced angle-ply composite laminate of finite width and subjected to bending deformation. Bending and torsion moments are combined to yield a deformation state without twisting curvature and with transverse curvature using only the laminate Poisson effect. This state of deformation is termed anticlastic bending.

The approximate elasticity solution for this bending deformation is shown to recover laminated plate theory predictions at interior regions of the laminate and thereby illustrates the boundary layer character of this inter-laminar phenomenon. The results exhibit the anticipated response in congruence with the solutions for uniform axial extension (Goodsell et al., 2013).

A simple three dimensional solid model for fiberglass prepreg laminated composites is developed and discussed in Chapter 6. The main objective of this model is to understand perform the progressive failure, predict the mode of fracture and compare the type of fracture with that of a failed specimen in the experimental study in order to validate the experimental results.

**1.8 Objective of Research**

In summary, the objective of the present research is to electrospin TEOS ENFs and using appropriate surface treatment, fabricate of composites using the out of autoclave vacuum bagging method with interleaving TEOS ENFs between the fiberglass laminates to study short beam improvement using a three point bend test. The experimental results will validate using three dimensional finite element modeling and analysis using ANSYS. The research focuses on the following objectives

1. Electrospinning and characterization of TEOS nanofibers
    a. The electrospinning set-up was modified to achieve consistent deposition of nanofibers on a 20 inches by16 inches collector plate.
    b. Optimization of processing parameters in order to improve the uniformity of nanofiber deposition while achieving higher deposition rates
    c. Sintering of nanofibers was done to achieve high surface roughness and a reduction in diameter of the fibers.

2. Fabrication and characterization of unidirectional prepreg of fiberglass composite prereg with and without TESO ENFs. The composite panels have been fabricated using the out of autoclave vacuum bagging method and have undergone mechanical characterization.
    a. Mechanical characterization of fiberglass, resin film and non-woven mat of TEOS ENFs.
    b. Static test for mechanical properties.
    c. The 23 ply composite is fabricated using a combination of 12 fiberglass and 11 resin film and other combination is for 23 plies of combination of 12 fiberglass and 11 resin film ply and compared to another 23 ply composite using combination of 12 fiberglass, 11 resin film and 11 TEOS ENFs layers with following stacking sequences
        i. $[0/0/0/0/0/0]_s$
        ii. $[0/90/90/0/0/90]_s$
        iii. $[0/60/-60/-60/60/0]_s$
        iv. $[+45/-45/+45/-45/+45/-45]_s$
3. Experimental analysis of short beam shear strength and mode of failures in unidirectional fiberglass composite
    a. Three point bending test for evaluation of short beam for all above stacking sequences of the laminates.
    b. Fractography of failed modified short beam strength specimens using optical and SEM images.
4. Modeling and analysis for inter-laminar stresses of laminated composite.
5. Finite element modeling and analysis for validation of experimental result.

6. Conclusions and future research.

Chapter 2 will discuss more about electrospinning and characterization of the TEOS nanofibers.

# CHAPTER 2

## Electrospinning and Characterization of TEOS Nanofibers

### 2.1 Introduction

Electrospinning of tetra ethyl orthosilicate is important process to produce non-woven nanofiber mats that are is used to interleave between two laminates. Electrospinning is a simple and versatile process to produce ultra-thin nanofibers in random, as well as aligned structure using a variety of polymers, ceramics, metals and composites. A comprehensive analysis of the electrospinning setup and process is available in the literature (Kelkar et al., 2010). Using tetraethyl orthosilicate (TEOS) sol-gel, electrospinning utilizes electrical force instead of mechanical force to drive the spinning process and produce nanofibers having diameters at least one or two order of magnitude smaller than mechanical processes.

### 2.2 Steps Involved in Electrospinning of Tetra Ethyl Orthosilicate Nanofibers

The critical steps involved in electrospinning tetra ethyl orthosilicate nanofibers are:

1. Preparation of the sol-gel solution using a titration method.
2. Promoting a polymerization reaction to form spinnable solution.
3. Conduct the electrospinning set up.
4. Measure the viscosity of the solution.
5. Maintain/control the humidity and temperature in the electrospinning hood.
6. Set the input parameter voltage to 18 kV with a feed rate 0.1 ml per min.
7. Set the distance between spinneret and collector plate to 20 cm.
8. Place Teflon or aluminum foil sheet on the collector plate.
9. Design the sliding speed and feed in the loop using software for 2 hours.
10. Connect voltage potential to steel needle at the tip of the solution.

11. Fill the syringe with 8-10 milliliters of the sol-gel and attach to the socket through plastic tubing.
12. Run the program for 2 hours.

**2.3 Sol-gel Solution**

The silica sol-gel was prepared from tetraethyl orthosilicate (TEOS), deionized (DI) water, ethanol (EtOH), and HCl. The mass ratio composition of the TEOS-ethanol solution was 95.5:10.425 (TEOS: ethanol). The mass ratio composition of the ethanol-D-water-HCl solution was 20.25:8.25:0.33 (ethanol: DI-water: HCL). The TEOS was mixed with ethanol in a beaker and stirred using a magnetic stirrer until it becomes a homogeneous solution. Then ethanol, DI water and HCl were then mixed and stirred vigorously, The EtoH/DI water/HCl was added slowly to the TEOS/EtoH solution via drop-wise titration of about 1 drop every 20 – 30 seconds while constantly stirring until the entire solution becomes single-phase solution. The hydrolysis and condensation reaction of TEOS occurred as shown in Figure 2.1(Xu et al., 2006).

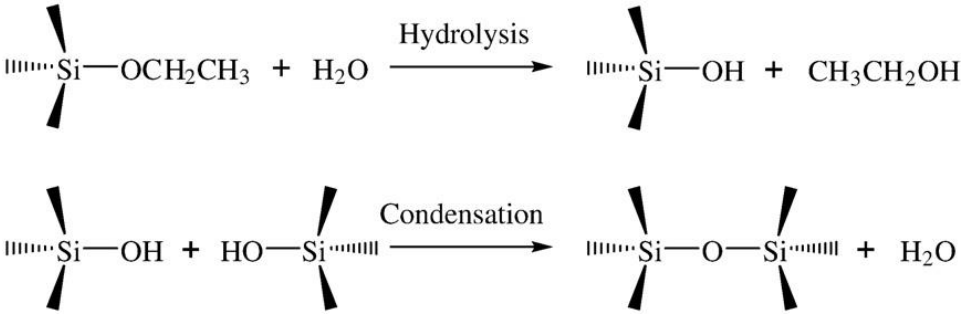


*Figure 2.1.* Reaction schemes for hydrolysis and condensation of TEOS

Aging was done with the beaker uncovered at room temperature for 32-48 hours in order to advance the polymerization reaction and increase the viscosity of the solution to a spinnable viscosity. The sol gel recipe above was adapted from S. Sakka, and K. Kayima(Sakka et al., 1982). The viscosity of solution was spinnable in the range of 180-350 Centipoise and measured using a ViscoTester $6^{R}$ from ThermoHaake Inc. as shown in Figure 2.2.

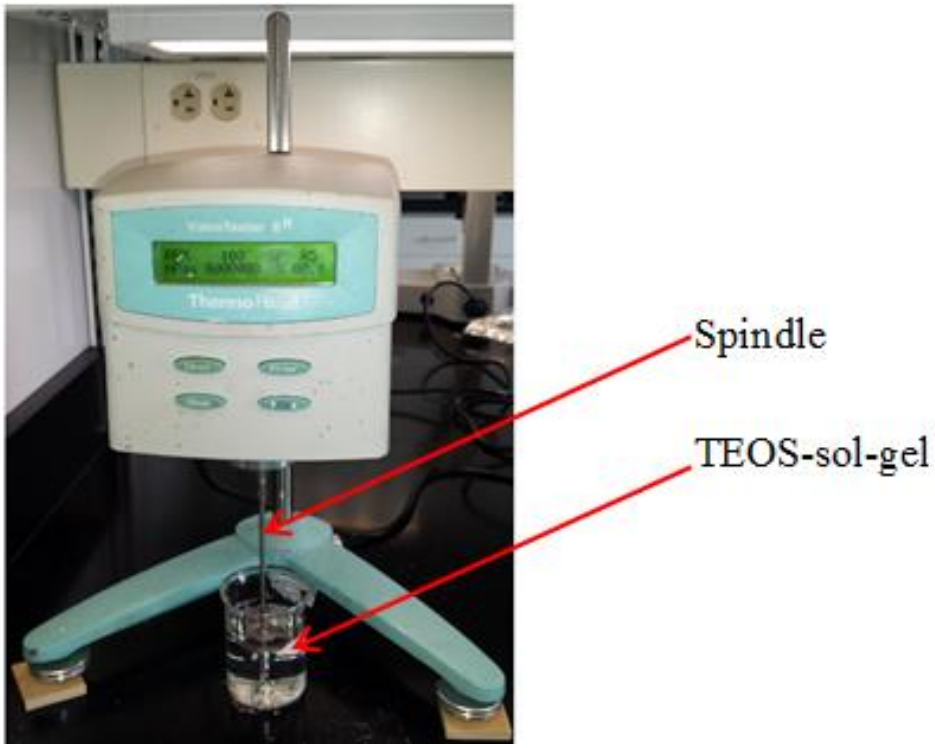


*Figure 2.2.* ViscoTester set-up for measurement of viscosity of sol-gel solution

**2.4 Electrospinning Process**

Electrospinning is a non-contact drawing process in which a polymer droplet emanating from the tip of spinneret is attracted towards a grounded collector due to the electrical potential difference applied and surface tension of the droplet. The electro-static forces cause the droplet to stretch, resulting in bending instability and whipping of the elongated jet producing fibers of nanoscale diameter (nanofibers) with exceptionally long lengths. Evaporation of solvents takes place as the nanofibers are deposited on a grounded collector. Splaying is not dominant in reduction of diameter of nanofibers. By controlling process parameters and properties of the polymer, ceramic or composite starting solution, fiber diameters from 3 - 900 nanometers can be produced(A. D. Kelkar et al., 2008). A schematic of the electrospinning set-up at the Joint School of Nanoscience and Nanoengineering is shown in Figures 2.2 and 2.3. Electrospinning is a fast and low cost manufacturing technique that can be easily scaled up. A computer controlled

program was made in VXS COSMOS Velmex Inc. version 2.0.1in order to move the plate horizontally and vertically in a controlled manner allowing uniform deposition of nanofibers on the collector plate. The dispensing pump was for the sol-gel solution from the stationary needle tip was a New Era Pumps Systems Inc. model.

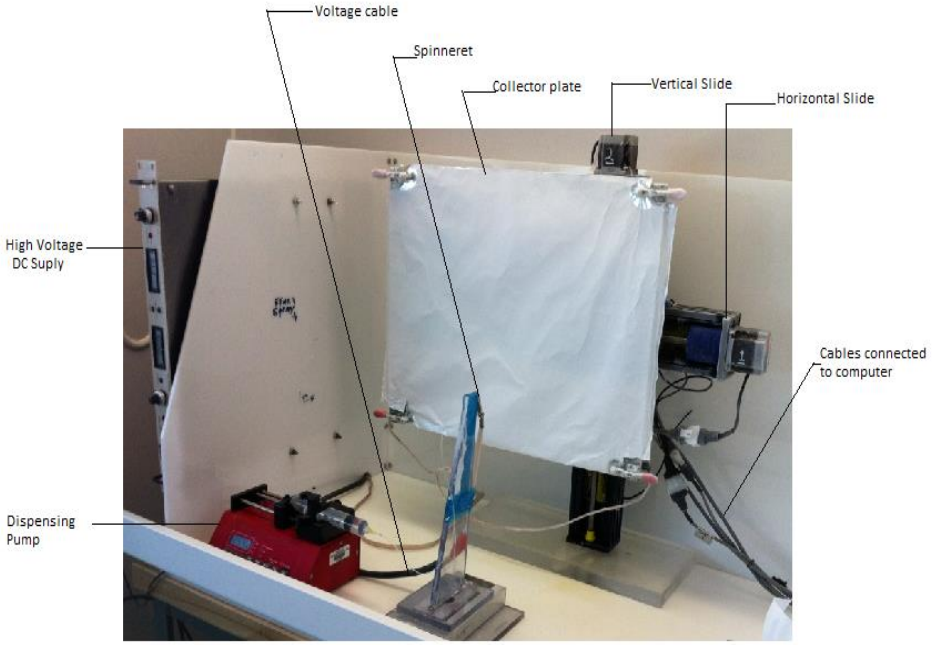


*Figure 2.3.* Electrospinning set-up at JSNN

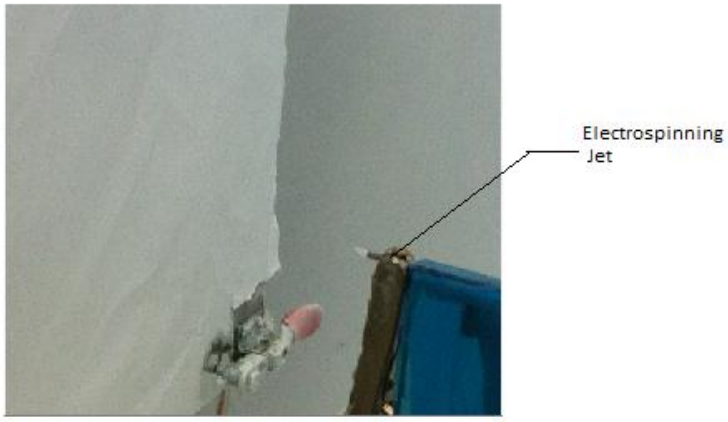


*Figure 2.4.* Electrospinning jet formation

### 2.4.1 Optimization of Processing Parameters

For optimization of processing parameters to reduce deposition time and deposit nanofibers uniformly, a laboratory setup for electrospinning has been modified for consistent deposition of uniform diameter nanofibers on Teflon/aluminum foil sheet. Operating parameters are optimized for a deposition process primarily governed by distance between spinneret and grounded collector, voltage applied, viscosity of solution and dispensing rate of sol-gel. The automated movement of the grounded collector was synchronized to rate the of deposition to achieve a reduction in time to deposit on the 20in x 16in Teflon/aluminum sheet using a computer controlled cross head movement along horizontal and vertical directions. The needles remain stationary at a set distance from the collector plate. To make a 20in x 16in sheet of nonwoven mat initially required approximately four hours for a sparse deposition. The process has been enhanced through the course of this research so that now a dense deposition of sol-gel nanofibers can be obtained in one hour. This helps to reduce the amount of sol-gel used, (which takes approximately 3 days to obtained the right viscosity).

The success of electrospun deposition depends on the viscosity characteristics of the sol-gel during the processing. The viscosity increases with aging and an optimal spinnable viscosity depends on environmental factors such as room temperature and humidity. The aging process of sol-gel was closely monitored to identify spinnable viscosity, based on weight percentage of the remaining sol-gel after evaporation during the aging process. The spinnable viscosity is achieved when 45% of total weight of initial Sol-gel is remaining(Sakka et al., 1982). Problems encountered using this trial and error and manual procedure can be summarized as clogging at the spinneret tip and, solidification of gel in less than 2 hours. In order to use a minimum amount

of solution to improve the process spinnable time window, a slightly modified procedure was developed:

i. Evaporation was stopped when 55% of the total weight of the original sol-gel remained by covering the solution using aluminum sheet.

ii. Only the required amount of TEOS sol-gel used for electrospinning was then taken and evaporated in a flat porcelain dish to achieve required spinnable viscosity.

iii. The remaining solution was kept covered using an aluminum foil. This precluded further evaporation reducing the solidification and provided a usable sol-gel over 72 hours. This is a very important process improvement considering the time required to develop the optimum viscosity and also to preserve the viscosity over a long duration.

iv. When viscosity increases, larger needles should be used before the solution is get ages to form a gel.

These modifications improved the electrospinning process and maximized utilization of TEOS solution, achieving nearly 85% usage of the spinnable solution compared to the 15-20% usage achieved with the original sol-gel preparation process. Currently, it is possible to electrospun coat four 20”X16” sheets with 120 grams of the prepared Sol-gel solution. In addition the process parameters were changed to optimize the process based on the viscosity level of the sol-gel used at the time of spinning. Voltage was increased from 9 kV to 15 kV, in order to change from lower to higher viscosity of sol-gel. A lower voltage was found to produce optimal fibers when the viscosity is low. A high voltage up to 18kV was applied when the viscosity of sol-gel was high. The distance between spinneret and grounded plate: varied from1 inch for high viscosity sol-gel to 8 inch for lower viscosity. The dispensing rate was maintained in the range 0.01 to 2 ml/min.

## 2.5 Characterization of TEOS Nanofibers

### 2.5.1 Geometric characterization

The characterization of electrospun fibers can be classified into four broad categories viz. mechanical, chemical, physical and geometrical. Mechanical characterization to determine mechanical properties of individual ENFs is extremely difficult and hence the least investigated area. The geometric characterization to find the morphology of the nanofibers is performed using SEM imaging by using Zeiss EVOLS10 Scanning electron microscope and the mechanical characterization is discussed in the chapter 3. The SEM imaging was done to understand the geometry of the ENFs before any surface treatment is shown in Figure 2.5.

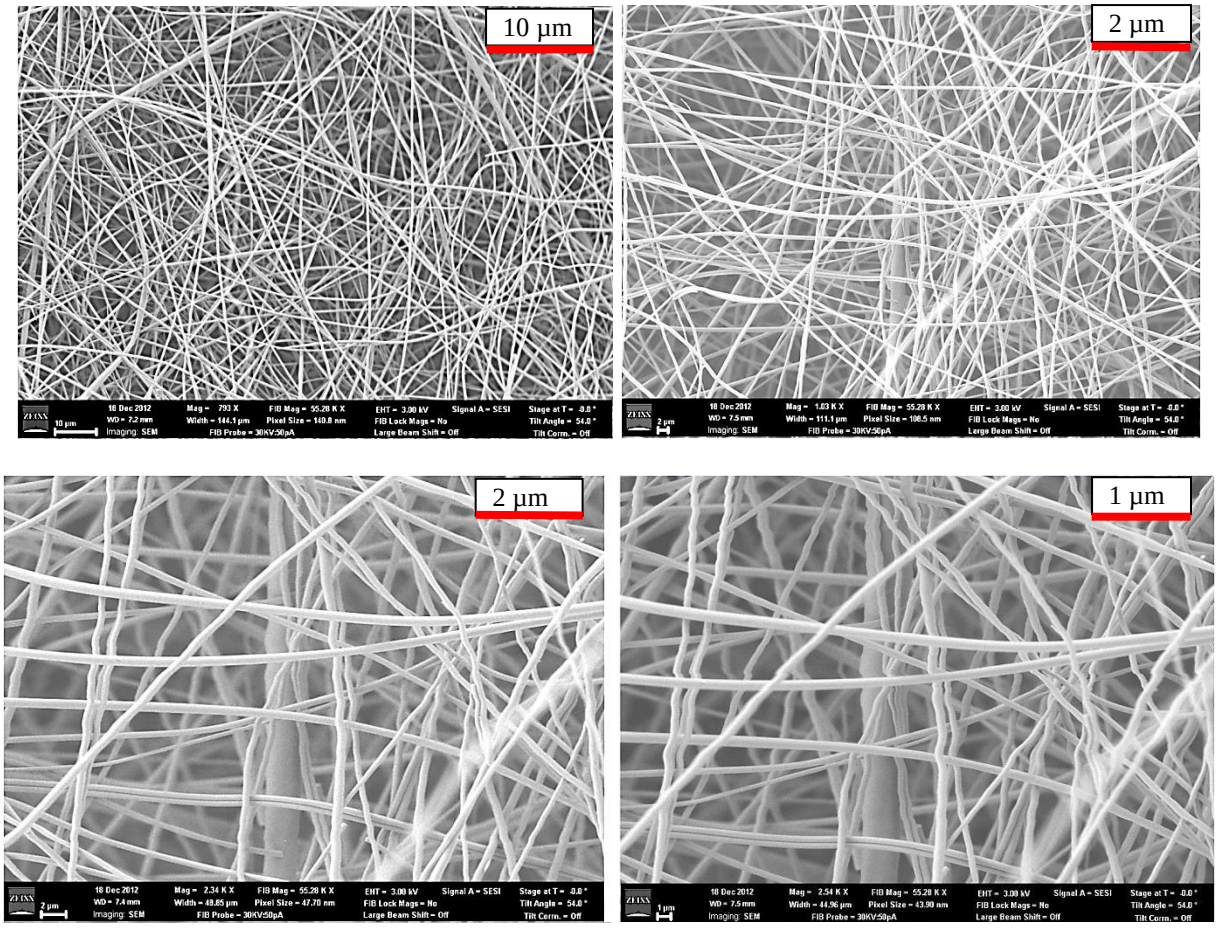


*Figure 2.5.* SEM micrograph of the TEOS ENFs

The electrospinning process was observed to be highly dependent upon the sol-gel formation and its processing. The sol-gel formulation is highly dependent on pH value of the HCl catalyst and ambient conditions such as temperature and humidity. A change in the pH value of HCl influences the time to obtain a spinnable viscosity. In some cases it was observed that the solution was not converted to solid glass even after one month of aging. This has resulted into inconsistencies in production and processing of electrospun fibers. The ambient conditions were observed to influence the Sol-gel formation. A temperature of 72 $^{0}$ F with a humidity of 30% was maintained. The temperature control was critical to the formation of suitable TESO nanofibers because it affected the sol-gel aging process.

These controlling ambient parameters have been identified hence possible check on the pH value of HCl and ambient conditions can eliminate inconsistencies during the process. Viscosity anticipated based on weight percent remaining is to be standardized by using scientific viscosity measurements. The problem involved in using available scientific viscosity measurement instruments is that they require larger fluid volumes while the amount of solution actually being used is very small and is about 10 grams. Thus it important to note that the Sol-gel prepared cannot be preserved at spinnable viscosity for a long duration. After one week of evaporation of ethanol from the fibrous sheet at ambient condition. TEOS nanofibers were soft. Figure 2.4 shows the SEM images for the TEOS nanofibers before sintering and had the diameter of the nanofibers of range of 300 - 500nm. There non-woven nanofibers mat had some ethanol. Therefore, it is essential to do some surface treatment so as to increase the surface to volume ratio and more porosity on the surface. The high resolution SEM images show the size of the nanofiber diameter and its shape before sintering is shown in Figure 2.6.

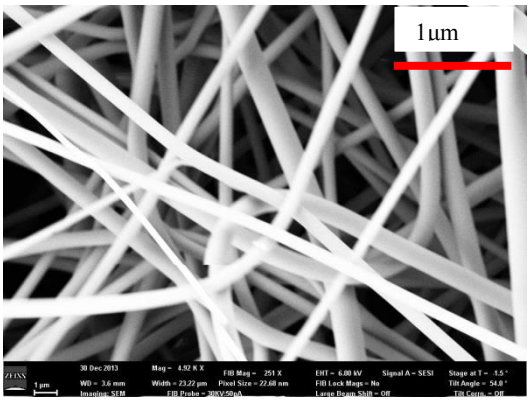


*Figure 2.6.* SEM micrograph of electrospun TEOS nanofibers before sintering

### *2.5.1.1 Sintering of TEOS ENFs*

The TEOS nanofibers mats were folded stacked together and put in the furnace as shown in Figure 2.6 they were sintered at a temperature of 600 $^{0}$ C for 6 hours (Shendokar et al., 2008)using am model Furnace 6000 supplied by Barnstead Thermodlyne Inc. After sintering, the TEOS nanofiber became brittle pre-sintered diameter range 300-600nm to from 250–450 nm after sintering and is shown in Figure 2.7.

The non-woven mats of TEOS nanofibers were then examined by SEM in order to perform geometric characterization.

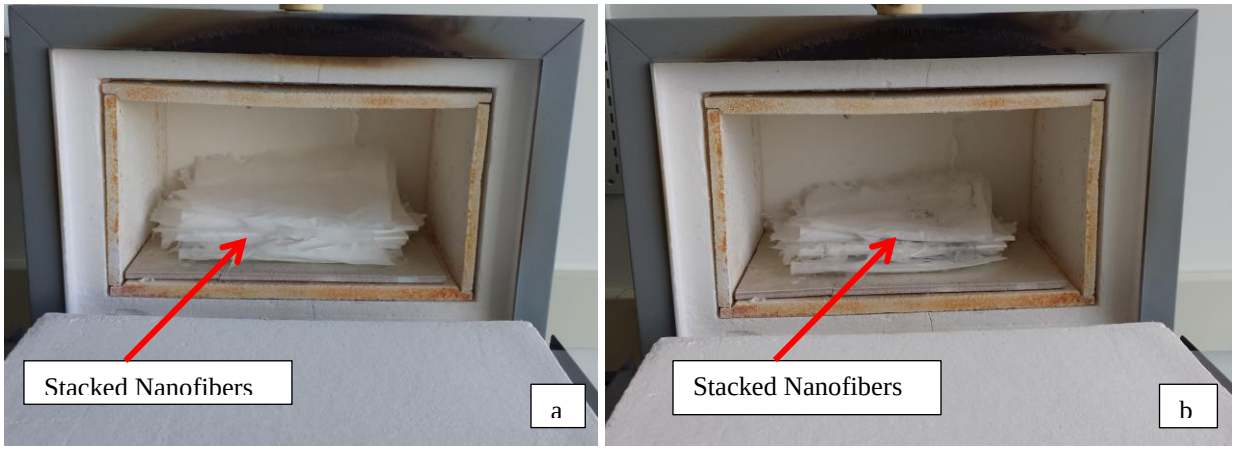


*Figure 2.7.* TEOS nanofibers mats were folded and stacked together in sintering furnace a) before b) after 600 $^{0}$ C

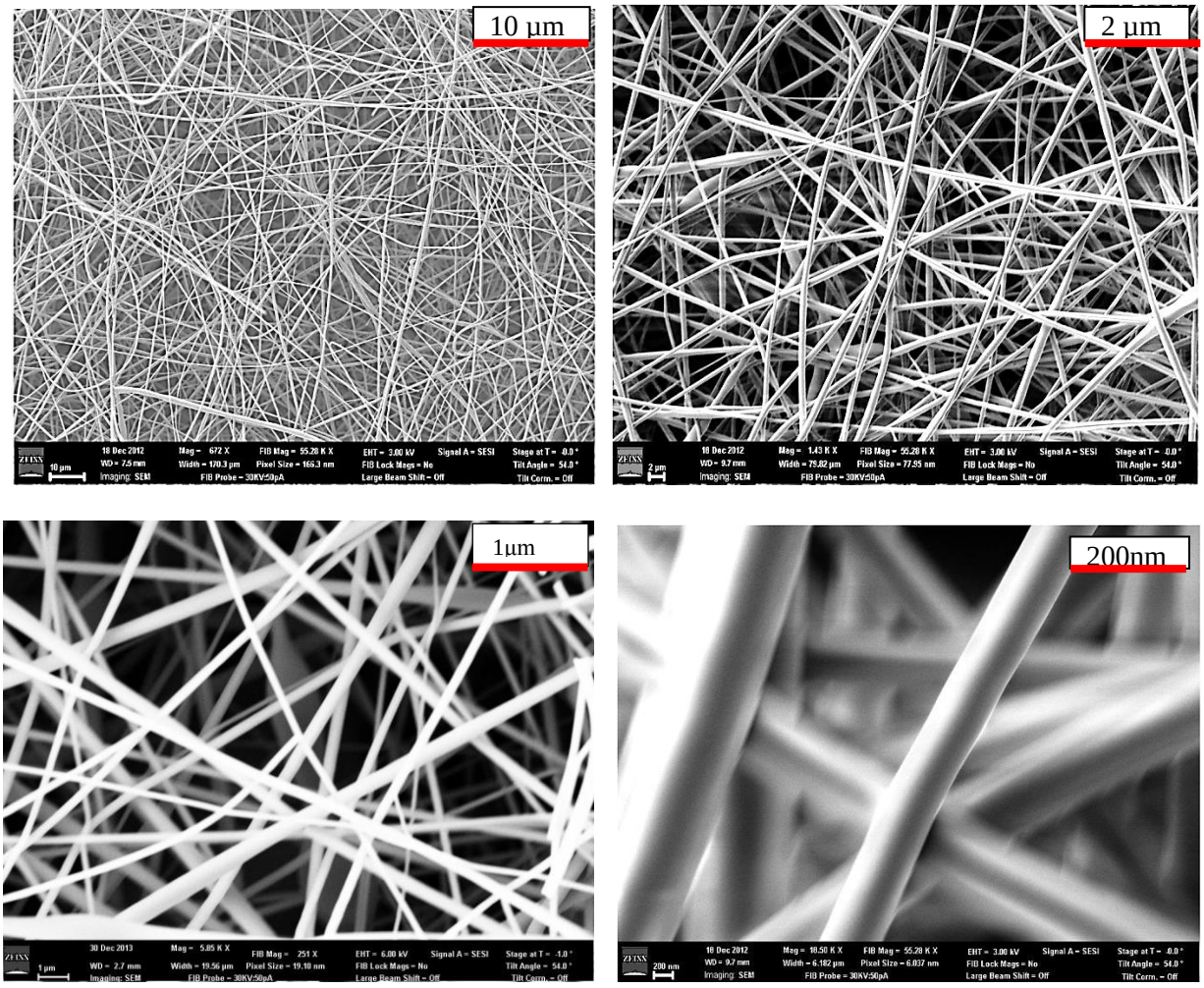


*Figure 2.8.* SEM micrograph of electrospun TEOS nanofibers after sintering at 600 $^{0}$C

This reduction in fibers diameter produces high surface to volume ratios and more porosity on the surface of the nanofibers as is shown in Figure 2.8.

### 2.5.2 Chemical characterization

Using a scanning electron microscope (SEM) (Zeiss EVOLS10), the EDX method was used to determine the chemical composition, and was used to measure weight percentages of the chemical element in the TEOS ENFs. Figure 2.9 shows that purely glass nanofibers were produced by the electrospinning.

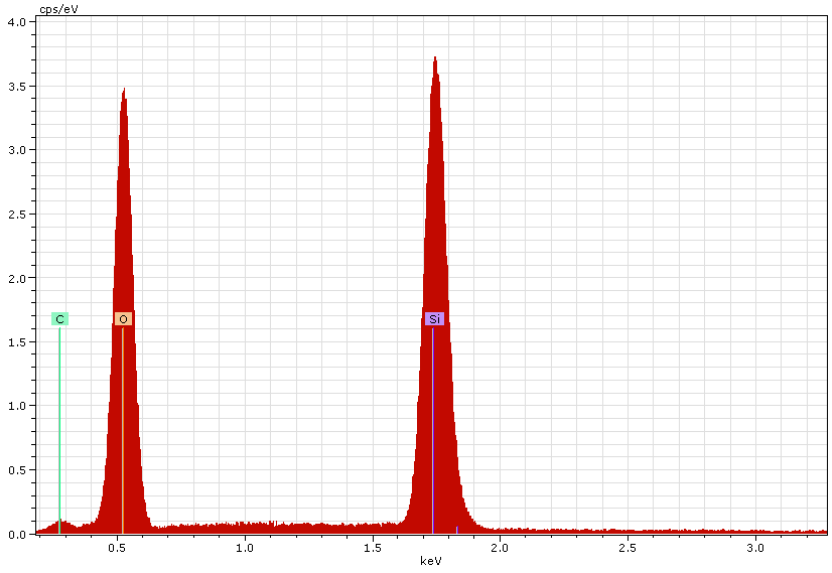


*Figure 2.9.* EDX data analysis with chemical content in the TEOS ENFs

The weight percentages for the nanofibers are shown in the Figure 2.10 after sintering. Only silicon and oxygen were present in the glass nanofibers.

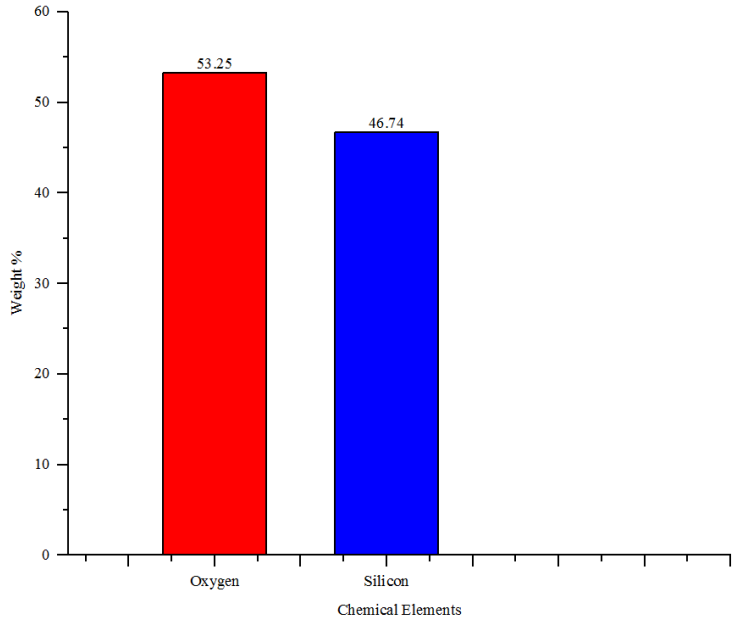


*Figure 2.10.* Weight percentage of chemical element in the TEOS ENFs.

### 2.5.3 Mechanical characterization

Because of the difficulties associated with the determination of mechanical properties of individual ENFs, only the percentage change of mechanical properties can be evaluated using resin matrix nanocomposites. Mechanical testing was performed as per ASTM standard and the nanocomposite panels were fabricated using the out of autoclave vacuum bagging method.

#### *2.5.3.1 Vacuum bagging process steps*

In this method, NB101epoxy resin film was purchased from Mitsubishi Rayon, Carbon fibers & composites, 1822 Reynolds Avenue, Irvine, CA 92614. This epoxy resin film was in the form of roll stored in a deep refrigerator and has a specific density 1.2 g/cc, gel time at 275 $^{0}$F was 3-5 min, and had a glass transition temperature of 115 $^{0}$C.

1. Cut 12 sheets of resin film in 12 inch x12 inch.
2. Cut 11 sheets of TEOS non-woven ENFs 12 inch x 12 inch.
3. Use the debulking machine and place one sheet of nanofibers on resin film sheet and apply vacuum pressure of 29 mm of Hg for 10 min.
4. Stack 11 ENFs sheets in between 12 sheets of epoxy resin film.
5. The Stack 12 RFs and 11 ENFs were put on glass plate mold in vacuum bagging without a top breather.
6. Cure the flat plate mold for 250 $^{0}$F for 3 hours.
7. The nanocomposite is visually inspected to assure that it is for free of defects.

Figure 2.11 shown the schematic for the out of autoclave vacuum bagging mold method for the nanocomposite stack of epoxy resin film and TEOS electrospun non-woven mats.

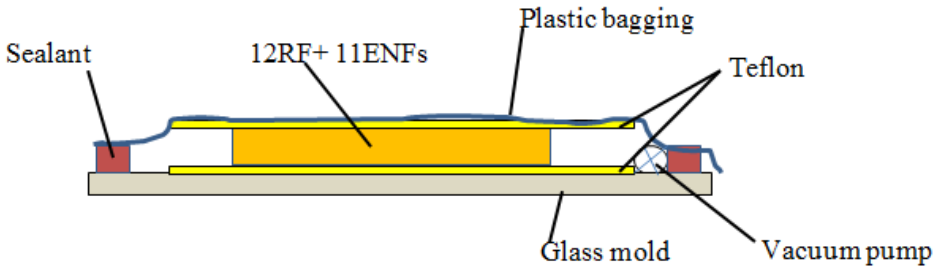


*Figure 2.11.* Out of autoclave vacuum bagging mold

After curing the nanocomposite for 250 $^{0}$ F for 3 hours in the computer controlled oven both the 12 neat epoxy resin film and 12 resin film panel and 11 ENFs panels were removed from the oven and are shown in Figure 2.12. The weight of 12 resin film was 316.1g before curing and 308.1g after curing. The weight of each ENFs sheet used was 2.1g with a total weight of 23.1g in the 12 GF and 11 ENFs nanocomposite.

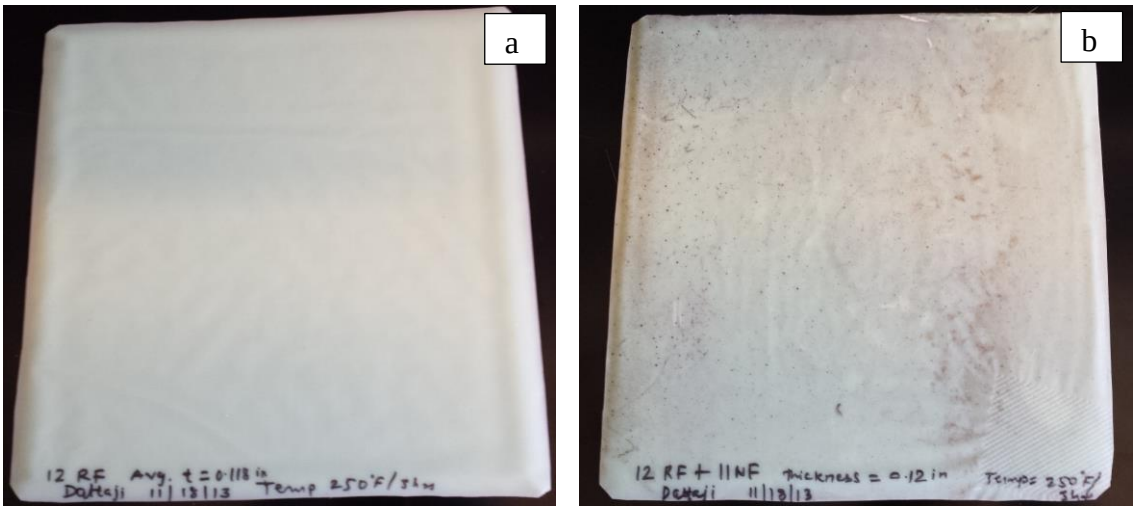


*Figure 2.12.* Composite panel cured at 250 $^{0}$ a) Neat Epoxy resin b) Epoxy with ENFs

The nanocomposite panels were visually inspected and cut using water jet machine as per ASTM standard D638(Designation, 2003) for tensile testing , ASTM D 3410(-95, 1995) for compression testing and ASTM D1002(-95, 1995) so as to obtain the mechanical properties of

epoxy resin and TEOS ENFs. The thickness of the panel with 12 RF was 0.113 inches and 12 RF and 11 ENFs was 0.12 inches.

### *2.5.3.2 Static test*

Specimens were cut as per ASTM standard for tension compression and shear testing and are shown in Figure 2.13 and tested as per the ASTM standards. Result of the tension, compression, and shear tests are shown in Table 2.1 to 2.6. The specimen were prepared according to ASTM standards using strain gages that were fixed on the specimens as shown in Figure 2.14in order to measure Poisson's ratio using lateral and longitudinal strain between the range of 1000 μs to 3000 μs.

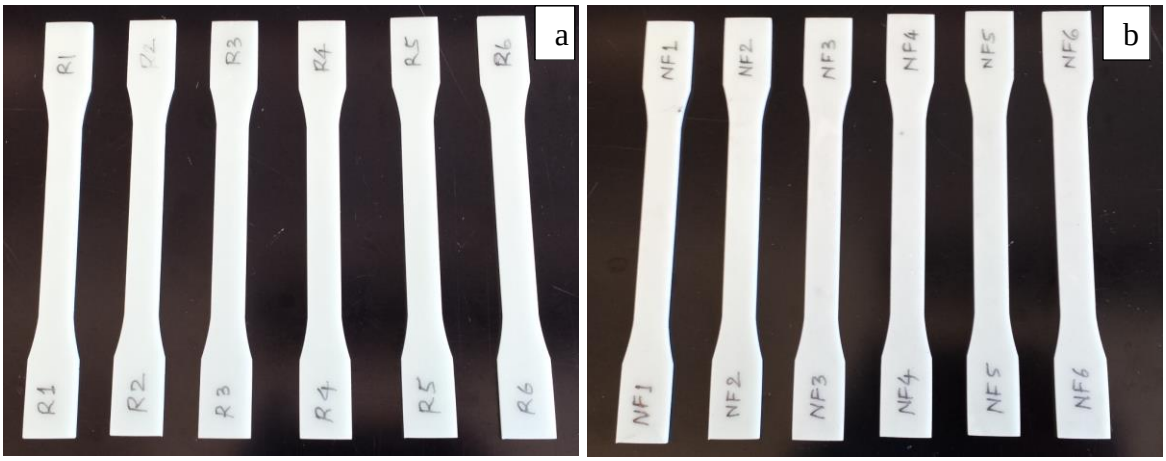


*Figure 2.13.* Specimens for tensile test a) Neat Epoxy resin b) Epoxy and ENFs

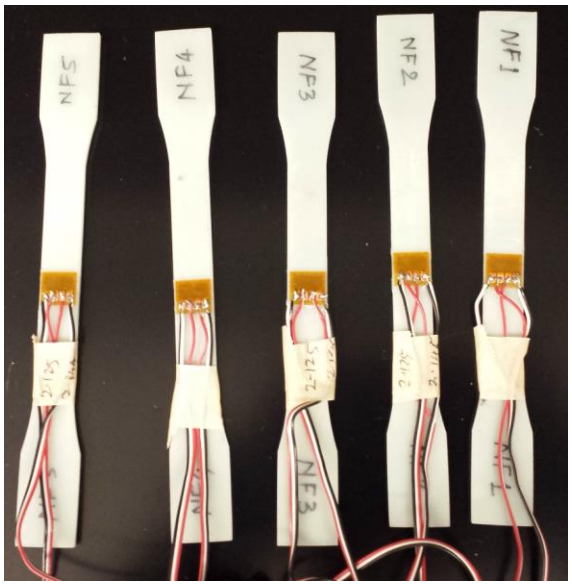


*Figure 2.14.* Nanocomposite specimen fixed with strain gages for tension test

*Table 2.1* Tensile properties of epoxy resin film with ENFs

| | Maximum Load (kip) | Tensile stress (ksi) | Chord Modulus (ksi) | Poisson's Ratio | Area (in^2) |
|---|---|---|---|---|---|
| 1 | 0.491 | 8.302 | 515.50 | 0.3608 | 0.059 |
| 2 | 0.495 | 8.539 | 483.36 | 0.3683 | 0.058 |
| 3 | 0.495 | 8.544 | 482.50 | 0.3682 | 0.058 |
| 4 | 0.508 | 8.733 | 477.52 | 0.3678 | 0.058 |
| 5 | 0.558 | 9.418 | 480.21 | 0.3668 | 0.059 |
| Mean | 0.5094 | 8.7072 | 487.82 | 0.3663 | 0.058 |
| SD | 0.0279 | 0.425739 | 15.63 | 0.0031 | 0.00 |

*Table 2.2* Tensile properties of epoxy resin film

| | Maximum Load (kip) | Tensile stress (ksi) | Chord Modulus) (ksi) | Poisson's Ratio | Area (in^2) |
|---|---|---|---|---|---|
| 1 | 0.493 | 8.80 | 432.18 | 0.3501 | 0.056 |
| 2 | 0.483 | 8.80 | 444.41 | 0.3532 | 0.055 |
| 3 | 0.475 | 8.34 | 443.21 | 0.361 | 0.057 |
| 4 | 0.473 | 8.31 | 444.72 | 0.3613 | 0.057 |
| 5 | 0.524 | 8.66 | 445.41 | 0.3523 | 0.060 |
| Mean | 0.4896 | 8.58 | 441.99 | 0.3555 | 0.057 |
| SD | 0.0211 | 0.24 | 5.53 | 0.0052 | 0.00 |

*Table 2.3* Compression properties of epoxy resin

| Specimen Number | Compressive stress (ksi) | Compressive load(lbf) | Area (in^2) | Failure Mode |
|---|---|---|---|---|
| C-Rf-2 | 4.79 | 565.35 | 0.118 | broken at middle into two pieces |
| C-RF-3 | 5.98 | 657.53 | 0.11 | broken at middle into two pieces |
| Mean | 5.38 | 611.44 | 0.114 | broken at middle into two pieces |
| SD | 0.83 | 65.18 | 0.005 | |

*Table 2.4* Compression properties of epoxy resin with ENFs

| Specimen Number | Compressive stress (ksi) | Compressive load(lbf) | Area (in^2) | Failure Mode |
|---|---|---|---|---|
| NF1 | 6.82 | 807.28 | 0.1184 | broken at middle into two pieces |
| NF4 | 6.42 | 728.9 | 0.1134 | broken at middle into two pieces |
| NF2 | 5.81 | 670.6 | 0.1154 | broken at middle into two pieces |
| Mean | 6.35 | 735.59 | 0.1157 | broken at middle into two pieces |
| SD | 0.51 | 68.58 | 0.0024 | |

*Table 2.5* Shear properties of ENFs

| Specimen label | Maximum Load (lbf) | Shear Strength P/(L*W) (psi) | Shear Area (in^2) | Nature Failure |
|---|---|---|---|---|
| NF-LS-1 | 3634.32 | 2690.10 | 1.35100 | shear failure |
| NF-LS-2 | 3633.37 | 2536.51 | 1.43243 | shear failure |
| NF-LS-3 | 3164.26 | 2322.63 | 1.36236 | shear failure |
| NF-LS-4 | 2965.09 | 2227.41 | 1.33118 | shear failure |
| Mean | 3349.26 | 2444.16 | 1.36924 | |
| SD | 338.52 | 208.77 | 0.04405 | |

*Table 2.6* Shear properties of neat epoxy resin

| Specimen label | Maximum Load (lbf) | Shear Strength P/(L*W) (psi) | Shear Area (in^2) | Nature of Failure |
|---|---|---|---|---|
| RF-LS-2 | 3775.87 | 3386.43 | 1.11500 | shear failure |
| RF-LS-3 | 4281.09 | 4281.09 | 1.00000 | shear failure |
| RF-LS-4 | 3779.17 | 3348.15 | 1.12873 | shear failure |
| RF-LS-5 | 4018.84 | 3385.05 | 1.18723 | shear failure |
| Mean | 3963.74 | 3600.18 | 1.10774 | |
| SD | 240.21 | 454.28 | 0.07836 | |

***2.5.3.3 Fiber volume fraction***

Overall fiber volume fraction $V_f$ is an important parameter to evaluate for a composite panel after manufacturing. Since fibers are the main load carrying element in the composite, their percentage has a direct effect on mechanical properties of the composites. Three methods may be used to determine fiber volume fraction $V_f$

1. The ignition method(ASTM 2584-68)
2. The areal weight method (ASTM D792-86)
3. The density method

*2.5.3.3.1 Ignition method*

The matrix is burned off in a high temperature furnace ( for epoxy resin, burned at 600 $^0$ C for 6 hours is used). The ash is rinsed from the remaining fiber using acetone or alcohol and the fiber is dried and weighed. The volume of the fiber is calculated by dividing the mass of the fiber by the density of the fiber material.

*2.5.3.3.2 Areal weight method*

The fiber volume fraction is determined from the areal weight of the reinforcing fibers and the volume of the composite using the following formula.

$V_f = \frac{(V)_{fiber}}{(V)_{Composite}} = \frac{(n * W * A)/\rho_f}{(A * t)} = \frac{n * W}{t * \rho_f}$ where

$(V)_{fiber}$ = Volume of the fiber material in the specimen

$(V)_{composite}$ = Volume of the composite specimen

$n =$ Number of layers or plies in the composite specimen

$W =$ Areal weight of the fabric

$A =$ Cross-sectional area of the composite specimen

$t =$ Thickness of the composite specimen

$\rho_f =$ Mass density of fiber material

*2.3.3.3.3 Density method*

The fiber volume fraction is determined from the densities of the composite assuming that voids are negligible or may be less than 1% (Daniel et al., 1994). The density of post cured composite was found using the ASTM D792-08 method. The expression for fiber volume fraction based on the density of the composite is

$V_f = \frac{\rho_c - \rho_m}{\rho_f - \rho_m}$ where

$\rho_f, \rho_m, \rho_c$ = Densities of fibers, matrix, and composite. For the characterization of resin film and TEOS ENFs, the density of NB 301 neat epoxy resin film is 1.22g/cc. The weight of of 1

inch X 1 inch X 0.1162 inch specimen of nanocomposite was measured and is shown Table 2.7 along with the weight fraction and volume fraction. The density of composite was calculated using the matrix burn method (ASTM D3171) and determined to be 1.4644 g/cc

*Table 2.7* Weight fraction of composite element

| Fraction element in composite | Weight (g) |
|---|---|
| Resin | 3.0743 |
| ENFs | 0.1451 |
| Composite | 3.2193 |

Weight fraction of Matrix $W_m = \frac{3.0743}{3.2193} = 0.96$

Volume fraction of Matrix $V_m = \frac{W_m}{\frac{\rho_c}{\rho_m}} = \frac{0.96}{1.22} * 100 = 78.11\%$

Using rule of mixture, fiber volume fraction is, $V_f = (1 - V_m) = (100.78.65) = 21.89\%$

***2.5.3.4 Rule of mixture***

The general rule of mixtures is used to predict various properties of composite materials made up of continuous and unidirectional fibers. It provides a theoretical upper- and lower-bound on properties such as the elastic modulus, mass density, and ultimate tensile strength. In axial loading, Voigt model gives the material properties(Alger, 1997). The rule of mixtures gives the overall modulus of elasticity in the direction parallel to the fibers and may be as high as is given by following expression(Voigt, 1889)

$E_C = V_f * E_f + (1 - V_f) * E_m$ where

$E_C$ = Modulus of elasticity of composite

$E_f$ = Modulus of elasticity of fibers

$E_m$ = Modulus of elasticity of matrix-resin

For tensile strength, $\sigma_C = V_f * \sigma_f + (1 - V_f) * \sigma_m$ where

$\sigma_C$ = Tensile strength of composite

$\sigma_f$ = Tensile strength of fibers

$\sigma_m$ = Tensile strength of matrix-resin

For Poisson's ratios, $\nu_C = V_f * \nu_f + (1 - V_f) * \nu_m$ where

$\nu_C$ = Poisson's ratios of composite

$\nu_f$ = Poisson's ratios of fibers

$\nu_m$ = Poisson's ratios of matrix-resin

For isotropic materials shear modulus is $G = \frac{E}{2*(1+\nu)}$ , and must be determined because both RF and RF+ NF materials are isotropic. Where $G$= shear modulus, $E$= moludus of elasticity, and $\nu$ = Poisson's ratio, the rule of mixture for calculation of shear modulus is $G_c = \frac{G_m * G_f}{(V_m * G_m + V_f * G_f)}$ where

$G_c$ = Shear Modulus of composite

$G_f$ = Shear Modulus of fibers

$G_m$ = Shear Modulus of matrix

For shear strength, $\tau_C = V_f * \tau_f + (1 - V_f) * \tau_m$ where

$\tau_C$ = Shear strength of composite

$\tau_f$ = Shear strength of fibers

$\tau_m$ = Shear strength of matrix-resin

Using Tables 2.1 to 2.6 the modulus of elasticity, tensile strength, compressive strength, Poisson's ratios, shear modulus, shear strength of ENFs in the nanocomposite are determined using the rule of mixtures and , are $E_f$= 657.45 ksi, $\sigma_{tf}$ = 9.15 ksi, $\sigma_{cf}$ = 9.92 ksi, $\nu_f$= 0.4054, $G_f$= 275.18ksi, and $\tau_f$ = 0.952 ksi respectively. A summary of the characterization date for epoxy resin and non-woven TEOS ENFs mat are shown in Table 2.8

*Table 2.8* Mechanical properties of GF, RF and non-woven TEOS ENFs

| Mechanical Properties | Materials | | |
|---|---|---|---|
| | RF | TEOS ENFs | RF-ENFs nanocomposite |
| $E_x$ (msi) | 0.442 | 0.658 | 0.488 |
| $\boldsymbol{\nu}_{xy}$ | 0.3558 | 0.4058 | 0.36 |
| $G_{xy}$ (ksi) | 163.03 | 275.18 | 178.57 |
| $\sigma_{xt}$ (ksi) | 8.58 | 9.15 | 8.71 |
| $\sigma_{xc}$ (ksi) | 5.38 | 9.92 | 6.35 |
| $\tau$ (ksi) | 3.6 | 0.952 | 2.44 |

**2.6 Conclusions**

The following conclusions were drawn from the experimental study regarding the electrospinning and characterization of TEOS nanofibers.

1. 95% deposition was achieved on a Teflon sheet (size 20" x 16") using approximately 1 ml of feed rate with optimal viscosity sol-gel (200 Centipoise) without clogging at the spinneret tip and adequate evaporation of the solution due to Teflon sheet.

2. Utilization of the sol-gel formed bulk solution was increased to 85% as compared to 15% to 20% of the formed solution was usable for electrospinning previously.
3. Optimum viscosity can be maintained without the beading effect.
4. Time required for deposition on one sheet (size 20 inch x 16 inch) is reduced to approximately 2 hour from the 4 to 6 hours as observed previously.
5. Approximately 4 sheets (size 20 x 16 inches) were deposited using 120 gm of the TEOS sol-gel prepared.
6. Geometrical characterization showed that before sintering TEOS nanofibers were soft and had ethanol contaminant even after drying for one week at room temperature. The pre-sintered nanofibers were 300- 600 nm in diameter with little bead formation on the nanofibers. After sintering at 600 $^{0}$C, the fiber become more brittle and porosity increased, the nanofiber diameter was decreased to 250-450 nm, thereby producing higher surface to volume ratio. Chemical characterization showed that stoichiometry of the electrospun fibers remained the same after sintering.
7. 12 sheets of epoxy resin film and 11 sheets of TEOS ENFs were used to make the nanocomposite using Vacuum bagging. Initially a breather was placed on the top of the stacked laminates, however most of the resin was absorbed during the vacuum in the curing process and little resin was left in the panel after curing. In the next experiment, the breather was not used and we did not lose any resin after curing of the panels. 12 RF and 11 ENFs sheets were chosen to obtain adequate thickness of the specimen for testing as per ASTM standards.
8. Mechanical characterization was done using ASTM standards for tension, compression, and shear testing. Volume fraction was calculated using the density method. The rule of

mixtures was used to determine the mechanical properties of the TEOS ENFs. The epoxy resin properties as well as the composite properties were calculated. Strain gages were used to measure the precise Poisson's ratio in neat epoxy resin specimens and nanocomposite specimens. The mechanical properties of the epoxy resin, TEOS ENFs, and nanocomposites were determined and could be useful for finite element analysis of the three point bend test of for short beam specimens.

Chapter 3 will discuss the characterization of the unidirectional fiberglass prepreg composite mechanical characterization.

# CHAPTER 3

## Fabrication and Characterization of Unidirectional of Fiberglass Prepreg Composite

### 3.1 Introduction

There are various methods used to manufacture composite laminates such as wet lay-up, autoclave processing, filament winding, pultrusion, resin transfer molding (RTM), and vacuum assisted resin transfer molding (VARTM). The motivation to use out-of-autoclave processing technology, due to the limitations of autoclave process such as high capital investment, large factory infrastructure, high cost of nitrogen, poor energy efficiency and, long turnaround time. Heated vacuum assisted resin transfer molding (H-VARTM), and out of autoclave processing are comparatively new processes and have proven to be cost effective compared to RTM. The unidirectional fiberglass prepreg laminated in the present research are manufactured using out-of-autoclave processing.

In out-of-autoclave processing, fiberglass prepreg was stacked together using the delbulking process. The stacked laminates are placed on a tool mold and vacuum bagged in conjunction with peel ply, release film, and breather. A vacuum was established in order to apply the pressure on the laminates. The laminates were then and cured under the same pressure for the required designed curing time temperature cycle in a computer controlled oven.

### 3.2 Vacuum-bagging Process

Vacuum-bagging is a clamping method that uses atmospheric pressure to hold the adhesive or resin-coated components of a lamination in place until the adhesive cures. The envelope can be an airtight mold on one side and an airtight bag on the other. The bag is sealed to the mold, pressure on the outside and inside of this envelope is equal to atmospheric pressure (approximately 29 inches of mercury (Hg), or 14.7 psi). As a vacuum pump evacuates air from

the inside of the envelope, atmospheric pressure forces the sides of the envelope and everything within the envelope together, putting equal and even pressure over the surface of the envelope. The pressure differential between the inside and outside of the envelope determines the amount of clamping force on the laminate, the schematic of the vacuum-bagging set-up is shown in Figure 3.1(Cantwell, 2011).

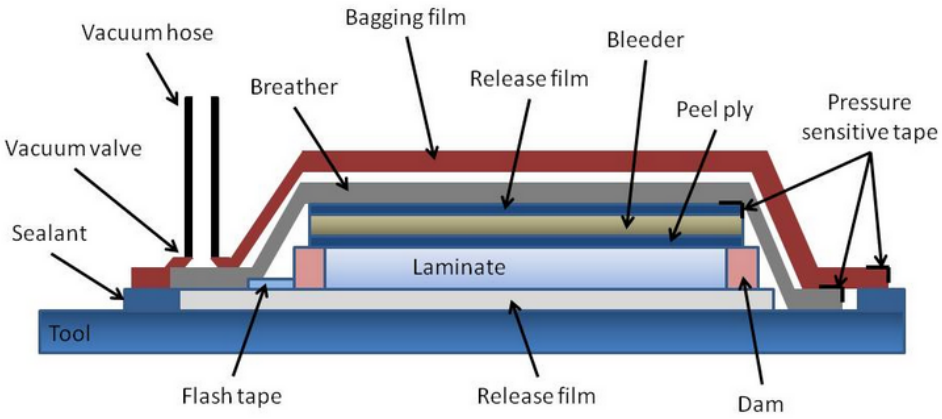


*Figure 3.1.*Vacuum-bagging process

Theoretically, the maximum possible pressure that can be exerted on the laminate, if it were possible to achieve a perfect vacuum and remove all of the air from the envelope, is one atmosphere, or 14.7 psi.

### 3.2.1 Debulking process

A process for debulking a fiberglass prepreg composite structure before curing involves forming a stack-up of a breather pad on a vacuum plate, a mandrel on the breather pad, a first release layer on the mandrel, a plurality of prepreg plies on the first release layer, a second release layer on the top ply, a breather sheet on the second release layer, and flexible vacuum bag sealed over the breather sheet to the vacuum plate. The stack-up sealed within a pressure vessel including flexible membrane which engages the vacuum bagging, drawing a vacuum from within the vacuum bag through the breather pad and the vacuum plate, pressurizing the pressure vessel

between the shell and the membrane; and maintaining the combination of vacuum and pressure for an interval of time to remove voids and porosity from the laminated prepreg (Cumings et al., 2008). The debulking processes set-up is shown in Figures 3.2 and 3.3.

*Figure 3.2.* Debulking set-up for fiberglass prepreg tape

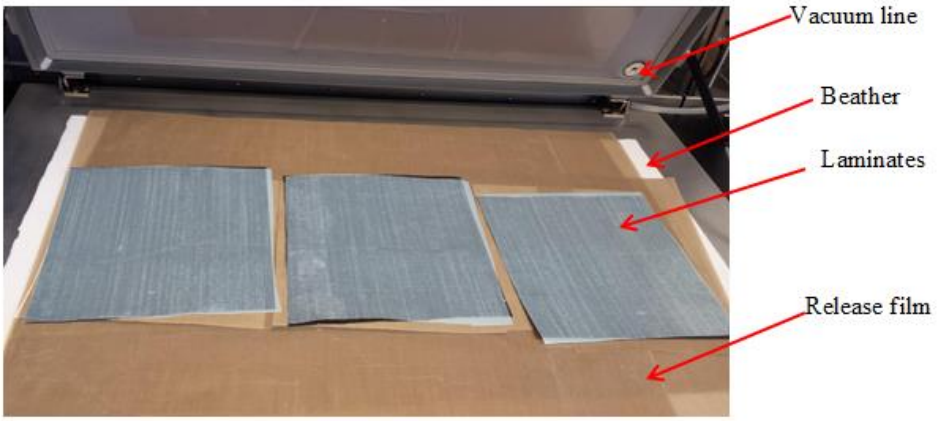


*Figure 3.3.* Debulking fiberglass prepreg tape with epoxy resin film

### 3.2.2 Selection of fibers

Unidirectional prepreg tape composite is used in structural applications such as sports goods, aircraft, primary structures, wind energy and, load carrying structures. We started with S-2 fiberglass for the study of inter-laminar stresses; however, the fiberglass used was woven

plain-weave. This structure causes undulation of fibers and fiber bridging effect on the interlaminar strength and prevent observation of delamination occurred in the fiberglass composite. Therefore, it was decided to use the unidirectional fiberglass prepreg tape to manufacture the composite. The architecture of fiberglass prepreg tape is shown in Figure 3.4(Hexcel, January 2013)

The NCT307 fiberglass prepreg was purchased from Mitsubishi Rayon, Carbon fibers & Composites, 1822 Reynolds Avenue, Irvine, CA 92614. This prepreg was in the form of a roll stored in a deep refrigerator having specific density 1.22 g/cc, gel time at 275 $^{0}$ F was 11-18 min, and a glass transition temperature was of 115 $^{0}$ C. The properties of the fiberglass prepreg tape are shown in Table 3.1. This prepreg tape is impregnated with epoxy resin and is compatible with epoxy resin film. In the case of interleaving of TEOS ENFs mats an additional epoxy resin film is required.

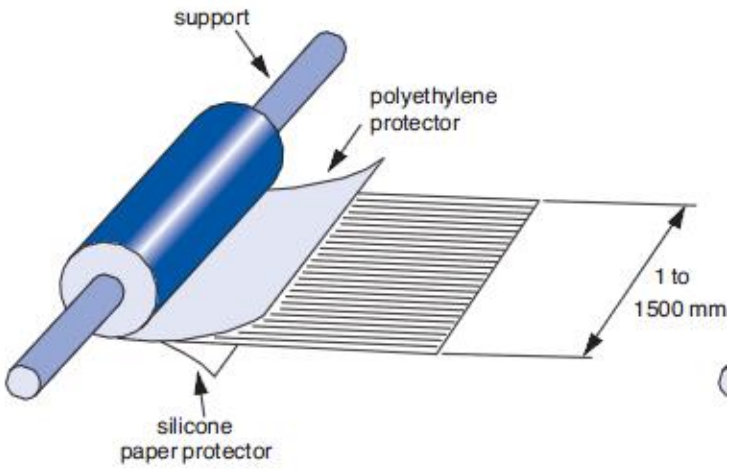


*Figure 3.4.* Architecture of fiberglass prepreg tape

*Table 3.1* Mechanical Properties of unidirectional fiberglass prepreg tape 7781 E-Glass reinforcement

| Property | Test Method | RT* | 160°F* | 200°F* |
|---|---|---|---|---|
| 0° Tensile strength, ksi | ASTM D-638 Type I | 63 | 55 | 54 |
| 0° Tensile modulus, Msi | | 3.3 | 3.1 | 3.0 |
| Poisson's ratio | | 0.11 | 0.11 | 0.11 |
| Strain, μ in/in | | 23,300 | 21,000 | 21,000 |
| 0° Compressive strength, ksi | SACMA 1R-94 | 61 | 58 | 54 |
| 0° Compressive modulus, Msi | | 3.4 | 3.3 | 3.4 |
| Strain, μ in/in | | 19,000 | 18,300 | 16,700 |
| 0° Flexural strength, ksi | ASTM D-790 | 88 | 75 | 64 |
| 0° Flexural modulus, Msi | | 3.3 | 3.4 | 3.0 |
| 0° Short Beam Shear strength, ksi | SACMA 8R-94 | 7.7 | 5.6 | 4.3 |

** Values are average and do not constitute a specification*

Mechanical properties of unidirectional fiberglass prepreg tape 7781 E-Glass reinforcement are average values obtained from NB 307 with style 7781 woven fiberglass. All values are based on using a vacuum bag oven cure, 1.5°F (0.8°C)/min ramp, 250°F (121°C) hold for 3 hours. Results are as tested, not normalized.

## 3.3 Steps in the Vacuum Bagging Process and Consolidation of Laminates

The vacuum bagging process involved the following steps to manufacture fiberglass composite:

1. Cutting of prepreg tape
2. Debulking of prepreg tape
3. Preparation of mold and vacuum bagging
4. Curing of mold in out-of-autoclave oven

### 3.3.1 Cutting of prepreg tape

Fiberglass prepreg tape was bought from Mitsubishi Rayon Carbon Fibers & Composites with product code Newport 307. The properties are shown in Table 3.1. Prepreg can be stored in the refrigerator 30 days out (time at $70^0$ F ($21^0$ C)). Prepreg tapes were taken out of the

refrigerator for two hours to defrost it. The tapes were cut into 20 sheet 24inch by 20 inch size in $0^0$ direction, then the all 20 pieces were debulked using debulking machine.

### 3.3.2 Debulking of pregregs tapes

The polyethylene protector is peeled from the face of the prepreg tape stacked with one piece and placed on the bottom plate of the debulking machine. The polyethylene protector is peeled from another sheet and two pieces are gently stick together put in the debulking set-up show in Figure 3.2. In order to remove the trapped air and void between two laminates, a 29 mm of Mercury (Hg) vacuum is applied for 10 minutes and then vented. The top face sheet silicone paper protectors of another piece is peeled and stick to another tapes, and put under the vacuum for 10 minutes. Similarly, the process is continued until all 20 pieces of prepreg tape were attached and debulked. When 20 sheet laminate is flat and debulked the laminates is weighted before it is put in the mold. The weight was 1483.9 g.

### 3.3.3 Preparation of mold and vacuum bagging

Put the debulked laminate in the flat plate glass mold. The mold is prepared followed the steps below and the schematic is shown in Figure 3.4:

1. Clean the glass plate with glass cleaner and apply wax and let it dry and then remove the wax using cotton gauze.
2. Apply release agent on the glass surface and let it dry.

   Stick the sealant tape around the inside area (26 inch by 22inch).
3. Prepare the vacuum line inlet for vacuum-bagging using spiral tubing through a connecting polyethylene pipe
4. Place the Teflon sheet that acts as a peel ply cut exactly inside dimension of the mold.

5. Place the debulked laminated fiberglass tape (20 sheets) after weighing on the Teflon sheet.
6. Place the Teflon sheet that acts as a peel ply cut exactly to the inside dimension of the mold on the laminates
7. Place the breather sheet that will help to take out the air and void from the laminated and also remove the excess resin that builds up during the curing of the mold.
8. Place a polyethylene plastic sheet on the mold and make sure the size of the plastic sheet will be more than the size of the sealant outer area.
9. Take out the silicone protector sheet from the sealant tape and stick the plastic sheet diagonally initially, and then stick firmly so that there will not be any leak in between the sealant tape and the plastic.
10. Apply a vacuum of 29 mm of Hg and close the vacuum line and wait for 15 min. for leakage identification.

These steps are followed for the vacuum-bagging process for fiberglass prepreg composites are shown in Figure 3.5.

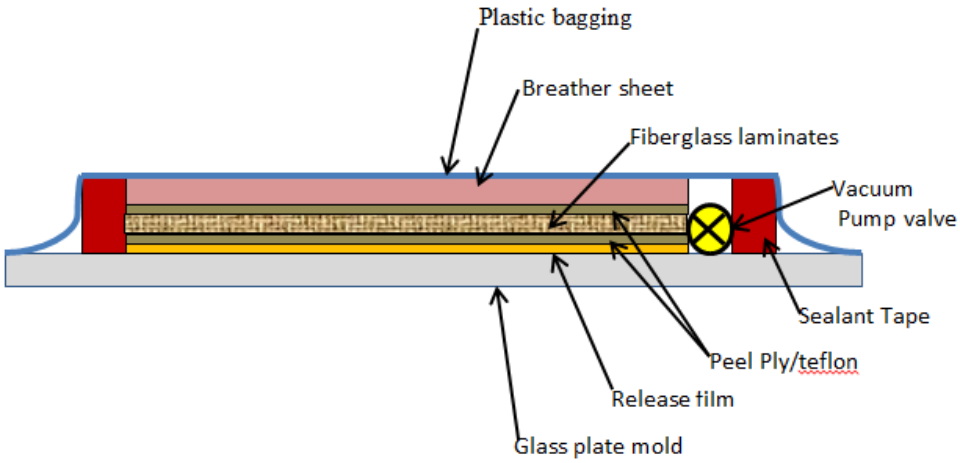


*Figure 3.5.* Schematic of Vacuum-bagging

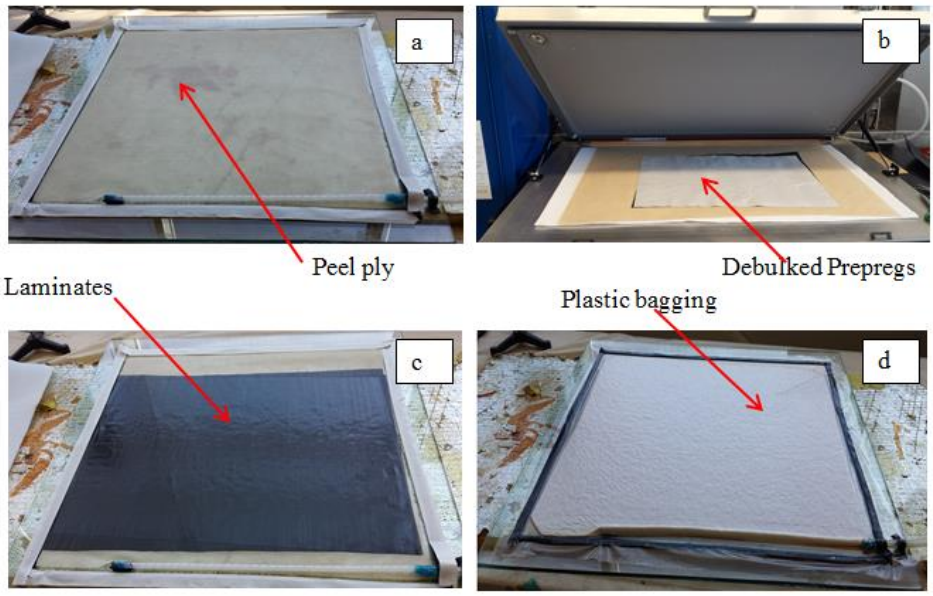


*Figure 3.6.* Process steps in the vacuum bagging of fiberglass prepreg in the $0^{0}$ direction a) lay-up of bottom peel ply, b) debulking of prepreg, c) prepreg laminates, and d) breather with outer bagging under vacuum

### 3.3.4 Curing of the mold in an out-of-autoclave process

Figure 3.7 shows the curing cycle for a mold was in the computer controlled oven. The laminated composite was consolidated and the cross linking of the resin completed during the curing cycle. The excess resin was absorbed by breather during curing cycle

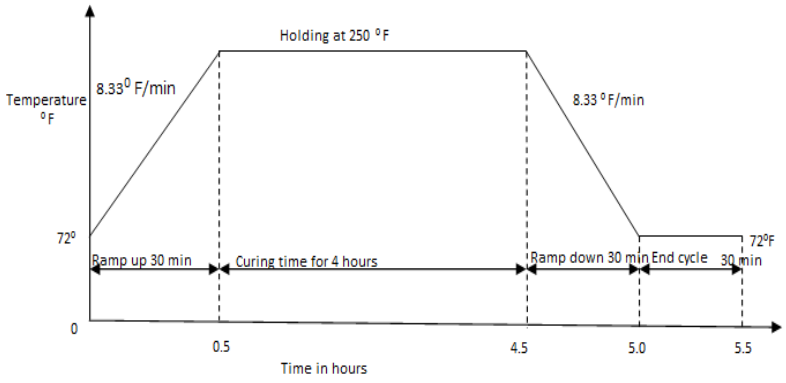


*Figure 3.7.* Cure and post cure time–temperature cycle

The laminated composite was taken out of the oven after curing and inspected visually for defects and voids on the surface. A sound test was performed and there were no voids and defects found in the composite panel. The composite panel was weighed after curing. The weight was 1293.6 g. A loss of approximately 190 g of resin was observed during curing. The lost resin was absorbed by the breather. The composite after curing was visually inspected and the composite panel is shown in Figure 3.8. The average thickness of the composite was 0.104 inches and its overall size was 24 inch by 20 inch. Later this composite panel was cut using the water jet.


*Figure 3.8.* Fiberglass composite after curing and inspection

**3.4 Overall Fiber Volume Ratios**

The overall fiber volume ratio was calculated using ASTM D3171 for fiberglass composite fabricated with prepreg tape. The fiber volume fractions for 20GF, 12GF + 11RF+11ENF, and 12GF+11RF samples were 62.13%, 39.86%, and 36.21% respectively.

**3.5 Static Test**

In order to perform the static test, the composite panel is cut in to specimens on the water jet machine as per ASTM standards for both $0^0$ and $90^0$ directions of the fibers in the composite.

The size of the specimens for the ASTM D3039 tensile test was 10 inches by 1 inch by 0.11 inches, the size of the specimens for the ASTM D 3410 compression tests was 6 inches by 1 inch by 0.11 inch, for the ASTM D 3518 ± $45^0$ tension to measure the shear strength and shear modulus, the specimens were of 10 inches by 1 inch by 0.11 inches. The ASTM D5379 test for the double v-notched shear test to measure the shear strength and modulus was done using 3 inch by 0.75 inch by 0.11 inch samples.

### 3.5.1 Preparation of specimens for testing

All specimens for tensile, compression, and shear test were cut using water jet machine as per the ASTM standards. The cutting layout of the specimens is shown in Figure 3.9.

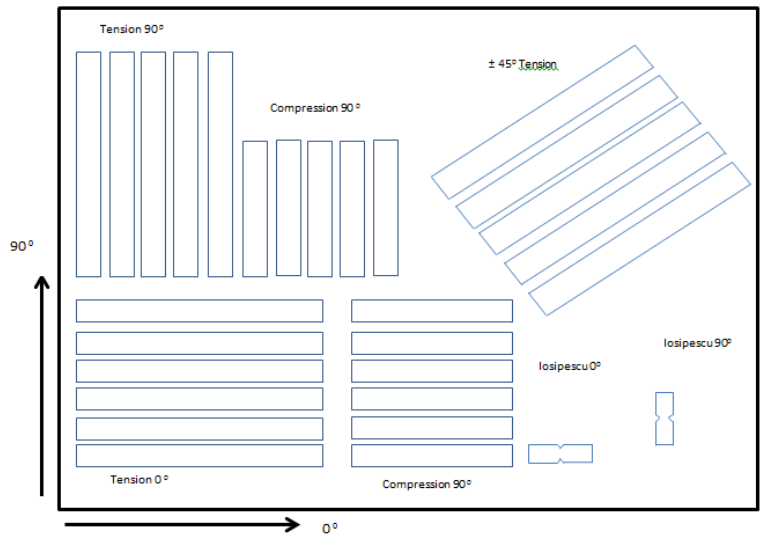


*Figure 3.9.* Composite panel layout for specimens to cut on water jet machine

Strain gages were attached to the specimens with gain factors 2.115 and 2.145 in longitudinal and lateral directions respectively as shown in Figure 3.10.

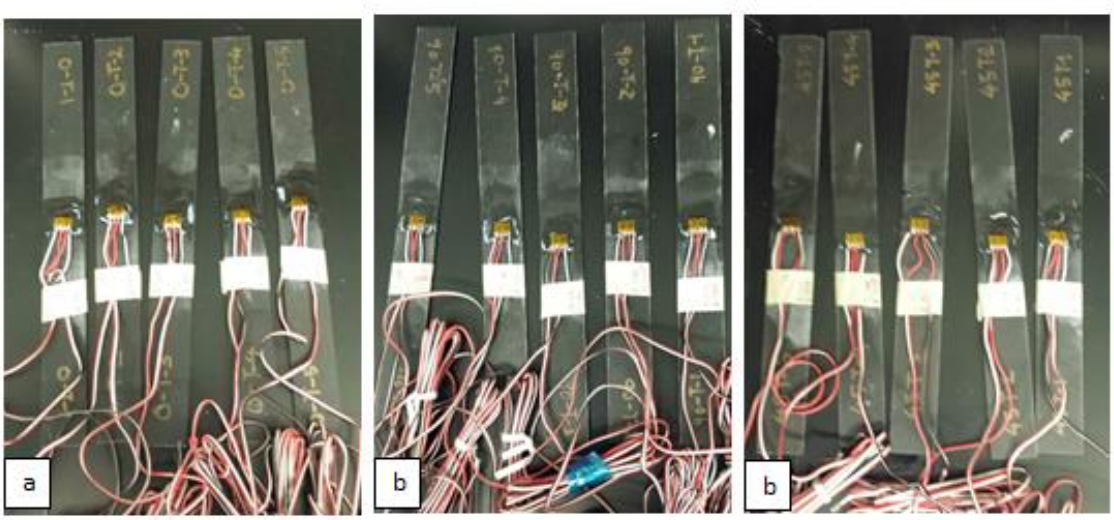


*Figure 3.10.* Specimens with strain gages for tensile testing a) $0^0$ b) $90^0$ and c) $\pm 45^0$

### 3.5.2 Tension test

The tension test was performed as per ASTM standards using ASTM D 3039(D. Astm, 2000) with a pull rate of 0.05 in/min on an Instron testing machine a 150kN load cell. The strain gages were connected through the signal processing amplifier channels to measure the strains. The gain factor was adjusted using Wheatstone bridge circuit resistance strain gages purchased from Micro-measurements, 951 Wendell Blvd., Wendell, NC 27591 USA. These strain gages were calibrated using the shut calibration method. Tables 3.2 and 3.3 show the tensile properties of the fiberglass composite in $0^0$ and $90^0$ direction. The Chord modulus was measured in the 1000 to 3000 μs range and the corresponding Poisson's ratios was calculated. The maximum strength was determined and the tension test was carried out on an Instron testing machine (shown in Figure 3.11) and the tensile failure of the fiberglass composite is shown in Figure 3.12.

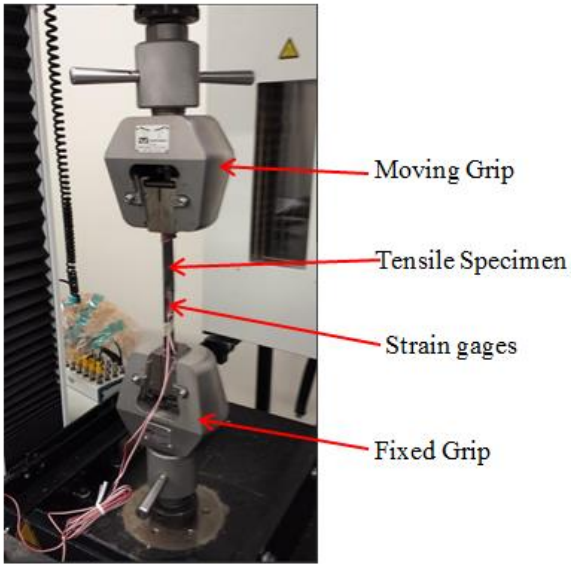


*Figure 3.11.*Tension test setup on the Instron testing machine

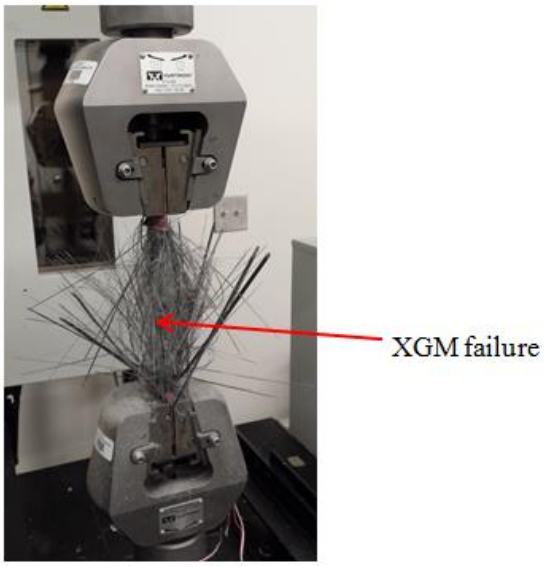


*Figure 3.12.* Nature of failure in tension test for fiberglass composites

*Table 3.2* Tensile properties of fiberglass prepreg composite in $0^0$ direction

| Specimens ID | Tensile stress (ksi) | Maximum Load (kpi) | Chord Modulus (msi) | Poisson's Ratio | Area (in^2) | Failure Mode |
|---|---|---|---|---|---|---|
| 0-T-1 | 172.73 | 17.1 | 5.97 | 0.2535 | 0.099 | XGM |
| 0-T-2 | 169.82 | 16.81 | 5.81 | 0.2561 | 0.099 | XGM |
| 0-T-3 | 159.44 | 15.94 | 5.82 | 0.2547 | 0.1 | XGM |
| 0-T-5 | 162.16 | 16.22 | 5.84 | 0.2549 | 0.1 | XGM |
| Mean | 166.03 | 16.51 | 5.86 | 0.2548 | | |
| SD | 6.262 | 0.531 | 0.07 | 0.0018 | | |

*Table 3.3* Tensile properties of fiberglass prepreg composite in $90^0$ direction

| Specimens ID | Tensile stress (ksi) | Maximum Load (kpi) | Chord Modulus (msi) | Poisson's Ratio | Area (in^2) | Failure Mode |
|---|---|---|---|---|---|---|
| 90-T-1 | 5.74 | 0.57 | 1.50 | 0.06133 | 0.1 | LAT |
| 90-T-2 | 5.29 | 0.56 | 1.26 | 0.06211 | 0.106 | LGM |
| 90-T-5 | 5.21 | 0.54 | 1.34 | 0.06399 | 0.103 | AGM1 |
| 90-T-4 | 4.87 | 0.5 | 1.42 | 0.06033 | 0.103 | AGM1 |
| 90-T-5 | 4.76 | 0.48 | 1.44 | 0.0609 | 0.1 | AGM1 |
| Mean | 5.17 | 0.53 | 1.39 | 0.061732 | 0.1024 | |
| SD | 0.38 | 0.03 | 0.08 | 0.00142 | 0.00251 | |

The tensile behavior of the fiberglass prepreg composite is shown in Figure 3.13. The behavior of the Tensile Stress as function of the Displacement data indicates that the tensile failure is an explosive type resulting in the specimen breaking in the form of a broom type of failure.

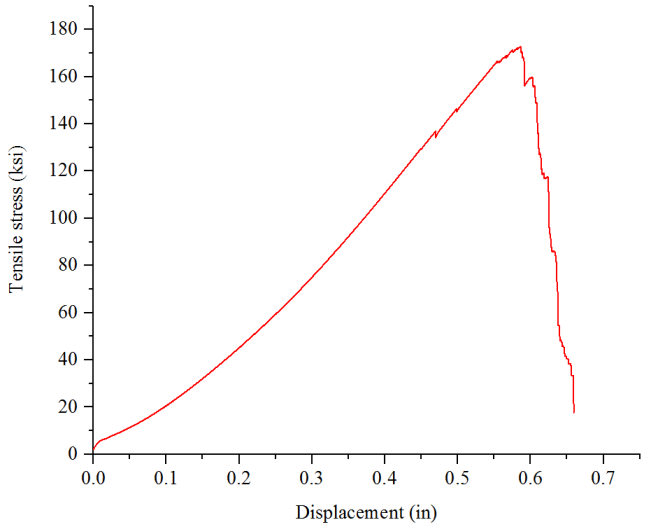


*Figure 3.13.*Tensile behavior of fiberglass prepreg composites

### 3.5.3 Compression test

The compression test was performed as per ASTM standards ASTM D 3410(ASTM, 2002) with a pull rate of 0.05 in/min using an Instron testing machine with a 150kN load cell. The strain gages were connected through the signal processing amplifier channels to record strains. The gain factor was adjusted using Wheatstone bridge circuit resistance. Table 3.4and 3.5 show the compressive properties of the fiberglass composite in the $0^0$ and $90^0$ directions. The Chord modulus was measured in the 1000 to 3000 μs range and the corresponding Poisson's ratios were calculated and the maximum strength was determined. The laboratory set-up for the Compression test as per ASTM D3410 on an Instron testing machine is shown in Figure 3.12.

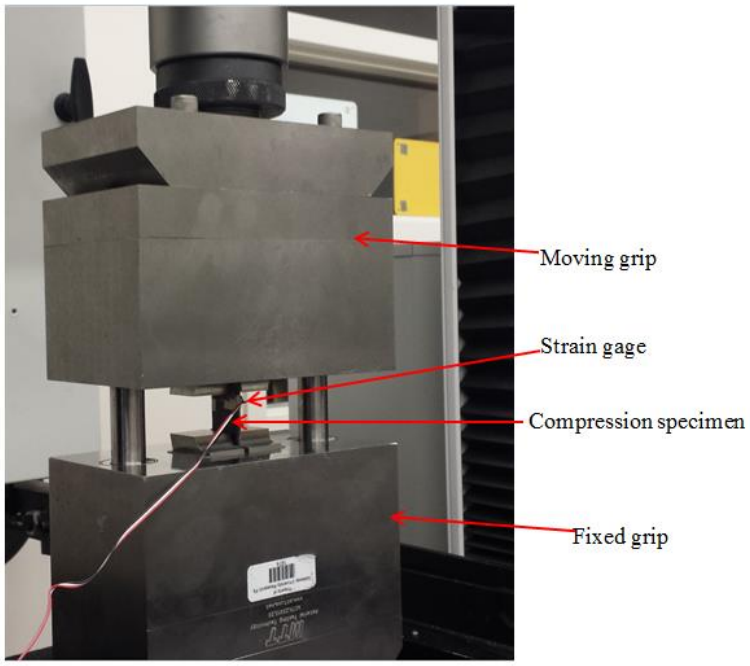


*Figure 3.14.* Compression test set-up on an Instron testing machine

*Table 3.4* Compressive properties of fiberglass prepreg composite the in $0^0$ direction

| Specimen Number | Compressive stress (ksi) | Compressive load (lbf) | Area (in^2) | Failure Mode |
|---|---|---|---|---|
| 0-C-3 | 50.08 | 4907.79 | 0.098 | failed at TAT |
| 0-C-4 | 38.23 | 3735.18 | 0.09771 | failed at TAT |
| 0-C-5 | 50.91 | 4994.2 | 0.09811 | failed at TAT |
| 0-C-11 | 50.15 | 4522.95 | 0.09018 | failed at HAT |
| Mean | 47.34 | 4540.03 | 0.096 | |
| SD | 6.08 | 574.34 | 0.003 | |

*Table 3.5* Compressive properties of fiberglass prepreg composite in the $90^0$ direction

| Specimen Number | Compressive stress (ksi) | Compressive load (lbf) | Area (in^2) | Failure Mode |
|---|---|---|---|---|
| 90-C-1 | 11.98 | 1251.59 | 0.10448 | middle broken |
| 90-C-3 | 11.25 | 1117.04 | 0.0993 | middle broken |
| 90-C-4 | 9.77 | 970.74 | 0.0994 | middle broken |
| 90-C-5 | 10.76 | 1066.56 | 0.0991 | middle broken |
| Mean | 10.94 | 1101.48 | 0.10057 | |
| SD | 0.92 | 117.032 | 0.00261 | |

Compressive behavior of a fiberglass composite is shown in the Figure 3.15. All specimens broke at the middle of gauge the length that corresponds to the expected type of failure mode in the ASTM standard.

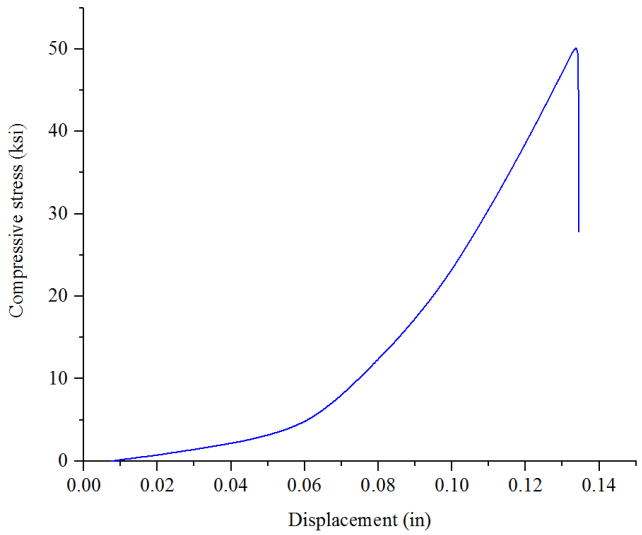


*Figure 3.15.* Compressive behavior of fiberglass prepreg composites

The tension test for ± $45^0$ (A. Standard, 2001) was performed and the results are shown in Table 3.6. The failure in the ± $45^0$ fiber orientation is in (Figure 3.14) is pure shear failure.

Table 3.6 *In plane shear properties of fiberglass prepreg composite for G12 at ± $45^0$ tension*

| Specimen Number | Tensile stress (ksi) | Maximum Load(kip) | Area (in^2) | In-plane shear strength (ksi) | G12(ksi) |
|---|---|---|---|---|---|
| 45-T-1 | 9.144 | 0.882 | 0.096 | 4.59 | 493.46 |
| 45-T-2 | 8.552 | 0.85 | 0.099 | 4.29 | 465.69 |
| 45-T-3 | 8.62 | 0.874 | 0.101 | 4.326 | 425.93 |
| 45-T-4 | 7.881 | 0.815 | 0.103 | 3.95 | 431.55 |
| 45-T-5 | 7.696 | 0.78 | 0.101 | 3.86 | 420.96 |
| Mean | 8.3786 | 0.8402 | 0.1 | 4.21 | 447.518 |
| SD | 0.589 | 0.0425 | 0.0026 | 0.2973 | 31.0935 |

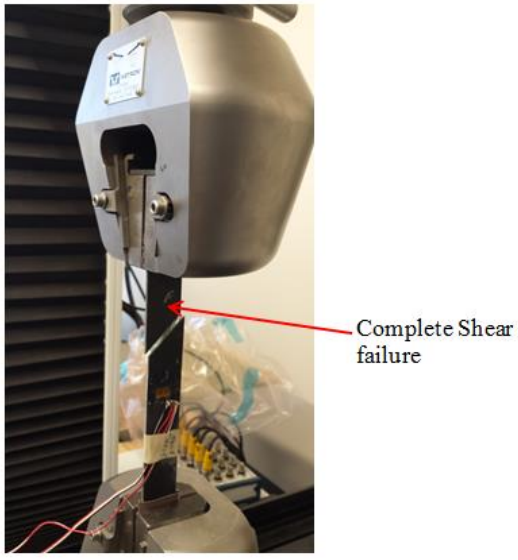


*Figure 3.16.* Nature of failure in tension test for fiberglass composites at ± $45^0$

### 3.5.4 Shear test

The shear properties of fiberglass prepreg composite materials are determined using double V-notched beam under the shear loading method described in ASTM D D5379/D5379M(A. Standard, 2005). The set-up for the Iosipescu is shown in Figure 3.15 and the shear strength and shear modulus $G_{12}$ is shown in Tables 3.7 and 3.8.

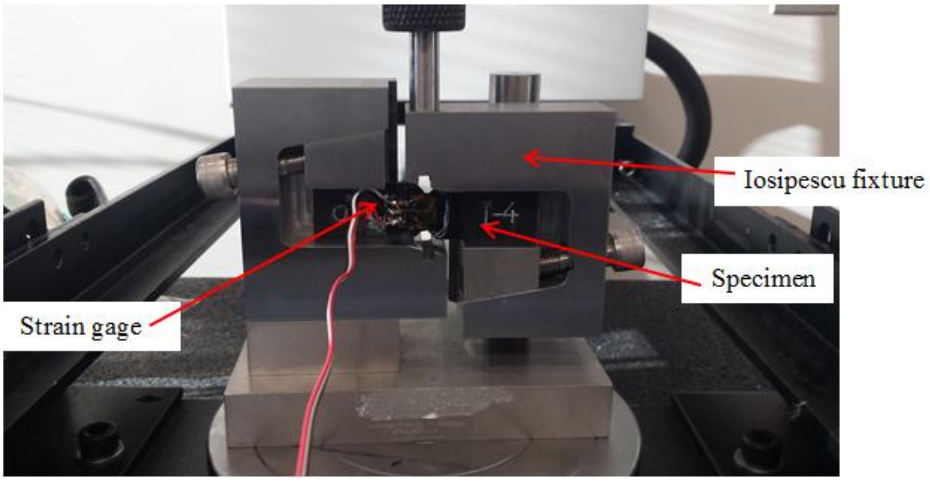


*Figure 3.17.* Iosipescu shear test setup on an Instron testing machine

*Table 3.7* Shear properties of fiberglass prepreg composites in the $0^0$ direction

| Specimen ID | Maximum load (lbf) | Max shear Strength (ksi) | Shear Modulus $G_{12}$(ksi) |
|---|---|---|---|
| I-4 | 689.04 | 13.06 | 463.41 |
| I-3 | 639.88 | 12.53 | 473.16 |
| I-5 | 638.88 | 11.89 | 439.63 |
| I-1 | 605.29 | 12.41 | 441.35 |
| I-2 | 621.12 | 12.73 | 456.23 |
| Mean | 638.84 | 12.52 | 456.39 |
| SD | 31.46 | 0.43 | 23.70 |

*Table 3.8* Shear properties of fiberglass prepreg composites in the $90^0$ direction

| Specimens ID | Maximum load (lbf) | Max shear Strength (ksi)) | Shear Modulus $G_{21}$(ksi) |
|---|---|---|---|
| 90-I-1 | 229.45 | 4.36 | 385.39 |
| 90-I-2 | 214.09 | 4.44 | 392.15 |
| 90-I-3 | 230.75 | 4.58 | 373.96 |
| 90-I-4 | 205.09 | 3.90 | 393.85 |
| 90-I-5 | 259.17 | 5.50 | 387.52 |
| Mean | 227.71 | 4.56 | 386.65 |
| SD | 20.61 | 0.58 | 11.02 |

Using the simplified composite micromechanics equation for mechanical properties proposed by Chamis, the Poisson ratios and shear modulus in the y-z and x-z planes are determined and are $G_{yz} = G_{xz} = 0.669$ msi and $\nu_{yz} = \nu_{xz} = 0.33$.

**3.6 Short Beam Strength Test**

The short beam strength of the laminated fiberglass composite was performed using the ASTM D 2344 test. The results of the test are shown in Table 3.9.

*Table 3.9* Short beam strength of fiberglass laminated composite

| Specimen | Maximum Compressive load (lbf) | Area (in^2) | Short Beam Strength (psi) |
|---|---|---|---|
| 1 | 141.14 | 0.02272 | 4658.84 |
| 2 | 130.16 | 0.02394 | 4078.42 |
| 3 | 127.27 | 0.02233 | 4275.44 |
| 4 | 132.54 | 0.02364 | 4204.49 |
| 6 | 124.43 | 0.02211 | 4220.27 |
| Mean | 131.11 | 0.02295 | 4287.49 |
| SD | 6.379 | 0.00081 | 219.75 |

## 3.7 Conclusions

The following conclusions were drawn from the experimental study of out of autoclave vacuum-bagging process and fiberglass prepreg composites.

1. The 10 minute debulking of the prepreg tape may not be adequate to remove 100% of the voids in the laminates
2. The vacuum pressure used (assumed to be 29 mm of Hg) was often less than 29 mm of Hg, hence constant vacuum pressure and longer time are required to debulk in order to reduce void in the composite panels.
3. The bottom surface of the mold had Teflon that created a smooth surface whereas the top has Teflon and a breather. The top surface became rougher. Also there was variation in thickness of the panel.

4. Vacuum-bagging process, although simple in concept, can be, quite complicated due to the equipment that is used many variables must controlled in order to produce a satisfactory result. The variables are as below:
    a. Processing temperature
    b. Vacuum pressure during the curing
    c. Temperature of the mold
    d. Proper placement of prepreg tape on the bottom tape
    e. Void and defects control.
5. After visual inspection, the composite panel was cut into the specimens as per ASTM standards. There were some voids found in the edges of some specimens, so by extension, it is expected that there were some voids in the panels.
6. During the tensile test the failure observed was quite different from normal fiberglass composites due to the proper alignment of the prepreg tape during the debulking. Also the standard deviation of the tensile test results was slightly higher than expected.

The mechanical properties of the fiberglass prepreg composites were determined using ASTM standard testing methods. All testing was performed on calibrated-Instron testing machines with precision. Failure occurring in the compression and shear tests matched the expected failure type of the standards. The prepreg material manufacturer did not test this fiberglass prepreg and hence we do not have data to compare to the experimental testing results. The mechanical properties of the fiberglass prepreg composites were tested and their properties are listed in the Table 3.9.

*Table 3.10* The mechanical properties of fiberglass prepreg composites

| Mechanical Properties | GF |
|---|---|
| $E_x$ (msi) | 5.86 |
| $E_y$ (msi) | 1.39 |
| $E_z$ (msi) | 1.39 |
| $\boldsymbol{\nu}_{xy}$ | 0.2548 |
| $\boldsymbol{\nu}_{yz}$ | 0.33 |
| $\boldsymbol{\nu}_{xz}$ | 0.33 |
| $G_{xy}$ (ksi) | 456.39 |
| $G_{yz}$ (ksi) | 669.12 |
| $G_{xz}$ (ksi) | 669.12 |
| $\sigma_{xt}$ (ksi) | 166.03 |
| $\sigma_{yt}$ (ksi) | 5.174 |
| $\sigma_{xc}$ (ksi) | 47.34 |
| $\sigma_{yc}$ (ksi) | 10.94 |
| $\tau$ (ksi) | 4.21 |
| $F^{sbs}$ (ksi) | 4.28 |

These mechanical properties will be useful for analytical and finite element analysis for the study of short beam strength in the laminated composite made with fiberglass prepreg with and without TEOS ENFs. The mechanical characterization of epoxy resin and TEOS ENFs are carried out in the chapter 2.

Chapter 4 will discuss the manufacturing of fiberglass prepreg composite with and without TEOS ENFs interleaved between fiberglass tapes with additional epoxy resin. Also, the experimental study of short beam strength of composites will be discussed.

# CHAPTER 4

## Experimental Investigation of Progressive Failure in Short Beam Fiberglass Composite Specimen with and without TEOS ENFs

### 4.1 Introduction

This chapter presents experimental investigation of progressive failure in short beam fiberglass composite specimens with and without TEOS ENFs. Chapter 3 presented the selection unidirectional fiberglass prepreg in the present study. Because of the unique fiber architectures in laminated polymer composites, the matrix materials which acts as a bond and protects the fibers reinforcements, also dominates out-of-plane mechanical properties, such as inter-laminar shear strength and mode I toughness, which are much lower than in-plane mechanical properties which are typically controlled by the reinforcement fibers(Zhu et al., 2007). In consequence, the most common type of failure mode in polymer matrix composite is the inter-laminar fracture (Todo et al., 2000).

To mitigate this problem substantial research has been carried for interface-toughening of composites in the last several decades. Recent investigations have revealed that nanoscale reinforcements could distinguishably enhance the toughness and damage tolerance of traditional structural composites used broadly in aerospace structures. One of the interesting approach is based upon incorporation of nano-reinforcement agents/fillers between composite plies/prepreg to form hybrid multi-scale composites(Chen et al., 2013). This approach has been predicted in theory and validated by experiments that the hybrid multi-scale fiber-reinforced composites with uniformly distributed nano-reinforcement agents between neighboring composite laminas/prepreg, would possess much enhanced mechanical properties (Dzenis et al., 2001). The

fabrication of fiberglass composite with unidirectional prepreg as discussed in the chapter 3, was used to manufacture the composite with TEOS ENFs interleaved between the fiberglass plies.

**4.2 Fabrication of Hybrid Composite with TEOS ENFs**

The fabrication of fiberglass prepreg composite with and without interleaving of TEOS electrospun nanofibers mat was done using vacuum bagging method. Initially, we used TEOS ENFs non-woven mat between the two laminates of the fiberglass prepreg and consolidated using out of autoclave vacuum bagging process. This composite was visually inspected and it was observed that the laminate contained several dry spots due to starvation of the epoxy resin. In order to alleviate this problem and additional resin film were used along with the nanofibers mats as shown in Figure 4.1. In the beginning nanofibers mats were sandwiched between the two resin films, but that gave resin rich interface with reduced fiber volume fraction ratio for the hybrid composite. To improve these fiber volume fraction ratios, one sheet of resin film and one non-woven TEOS ENFs sheet was used in between two prepreg of the fiberglass tapes. The flow chart for the optimization of soaking of TEOS ENFs sheet in between the prepreg tapes with one resin film is shown in Figure 4.1.

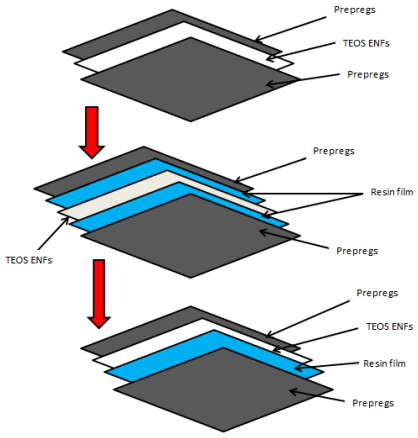


*Figure 4.1.* Flow chart for the optimization of soaking TEOS ENFs sheet in the resin of prepreg tapes

Once the optimization of resin film for the hybrid composite manufacturing was performed, the hybrid composite panels were fabricated using out f autoclave vacuum bagging process as shown in Figure 4.2.

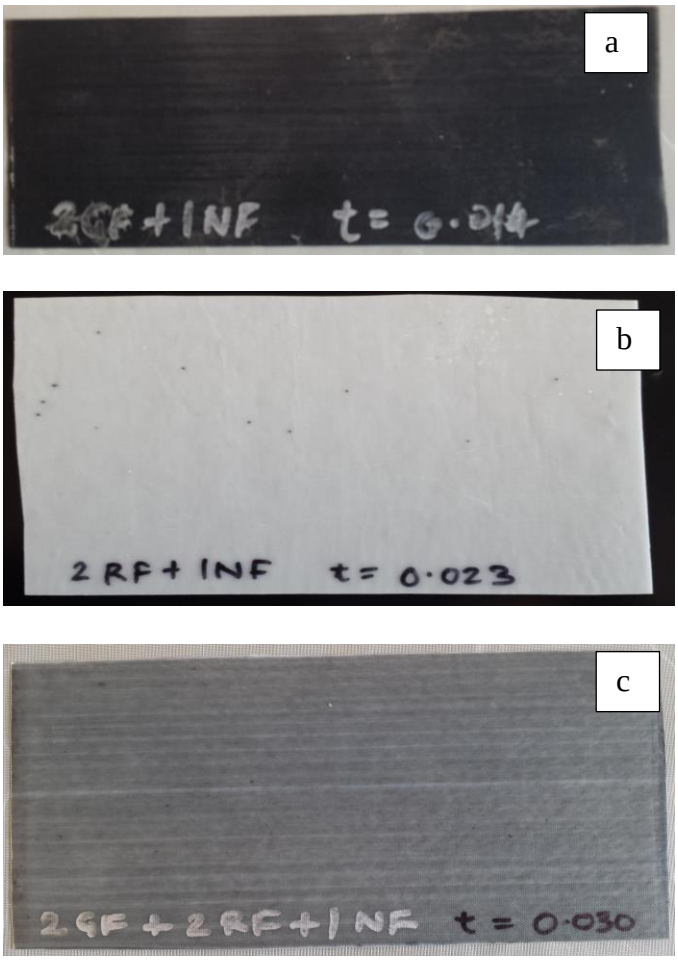


*Figure 4.2.* Steps in optimization of thickness and the proper soaking of sandwiched TEOS ENFs mat in a hybrid composite a) between two prepreg, b) between two epoxy resin film, and c) two prepreg with two resin film

The thicknesses of hybrid composites fabricated using various nanofibers mats/resin film configurations are shown in Table 4.1.

*Table 4.1* Thickness of hybrid composite

| Hybrid composite laminates | Thickness(in) |
|---|---|
| 2 fiberglass prepreg and 1 TEOS ENFs mat | 0.014 |
| 2 epoxy resin film and 1 TEOS ENFs mat | 0.023 |
| 2 fiberglass prepreg and 2 epoxy resin film and 1 TEOS ENFs mat | 0.030 |

**4.3 Stacking Sequence for the Short Beam Samples**

The following symmetrically balanced stacking sequence was chosen for the experimental study of short beam of the fiberglass prepreg composites that were fabricated, with and without TEOS ENFs is used as follow:

a. $[0/0/0/0/0/0]_s$

b. $[0/90/90/0/0/90]_s$

c. $[0/60/-60/-60/60/0]_s$

d. $[+45/-45/45/-45/+45/-45]_s$

**4.4 Fabrication of Hybrid Composite Panel**

For all stacking sequences, fiberglass prepreg tape and epoxy resin films were cut exactly of the size of 8 inches by 6 inches, and were stored in the fridge. Next day, the prepreg were taken out of the fridge and were defrosted for 2 hours, and, then debulked for 10 minutes under 29 mm of hg vacuum pressure as per the process outlined in Chapter 3. The manufacturing of composites and debulking steps are shown in Figure 4.3. The same curing cycle as described in Chapter 3 was used to fabricate the panels.

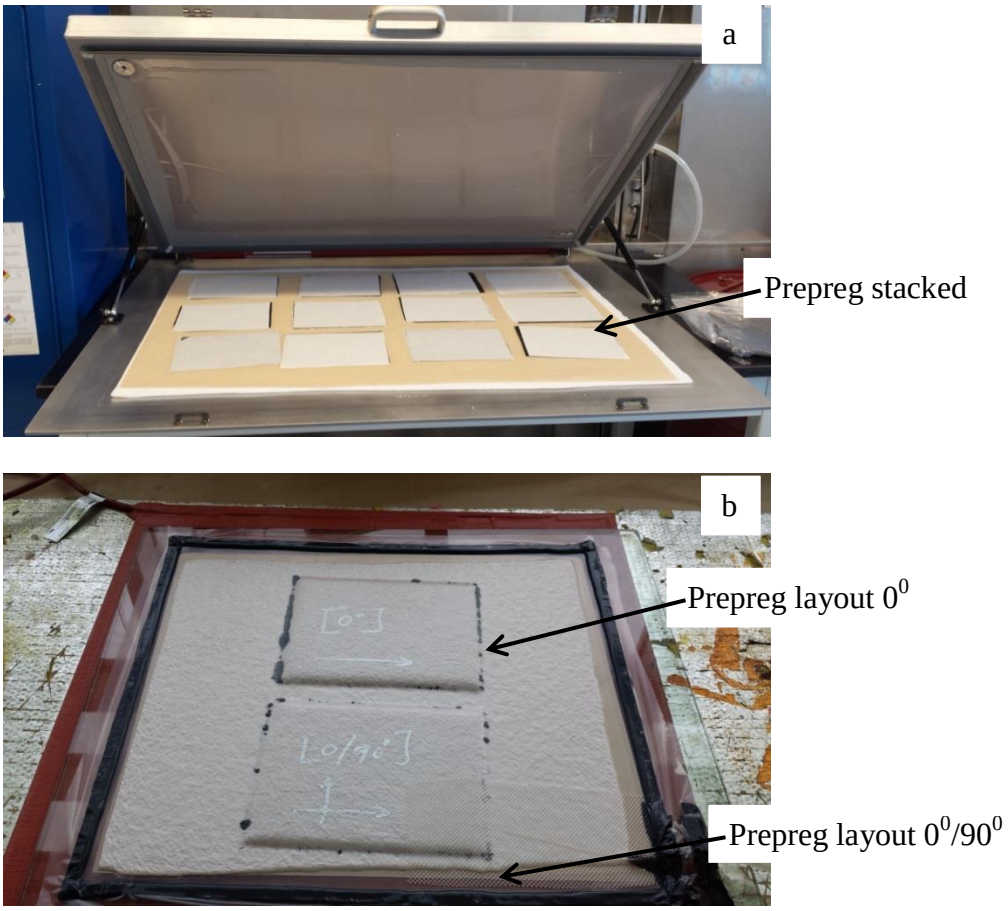


*Figure 4.3.* Manufacturing of hybrid composite a) debulking steps b) cured composite panels

The hybrid composite with a TEOS ENFs and fiberglass composite manufactured with four different symmetric stacking sequences is shown in Figure 4.4. After curing the panels were visually inspected for voids and defects.

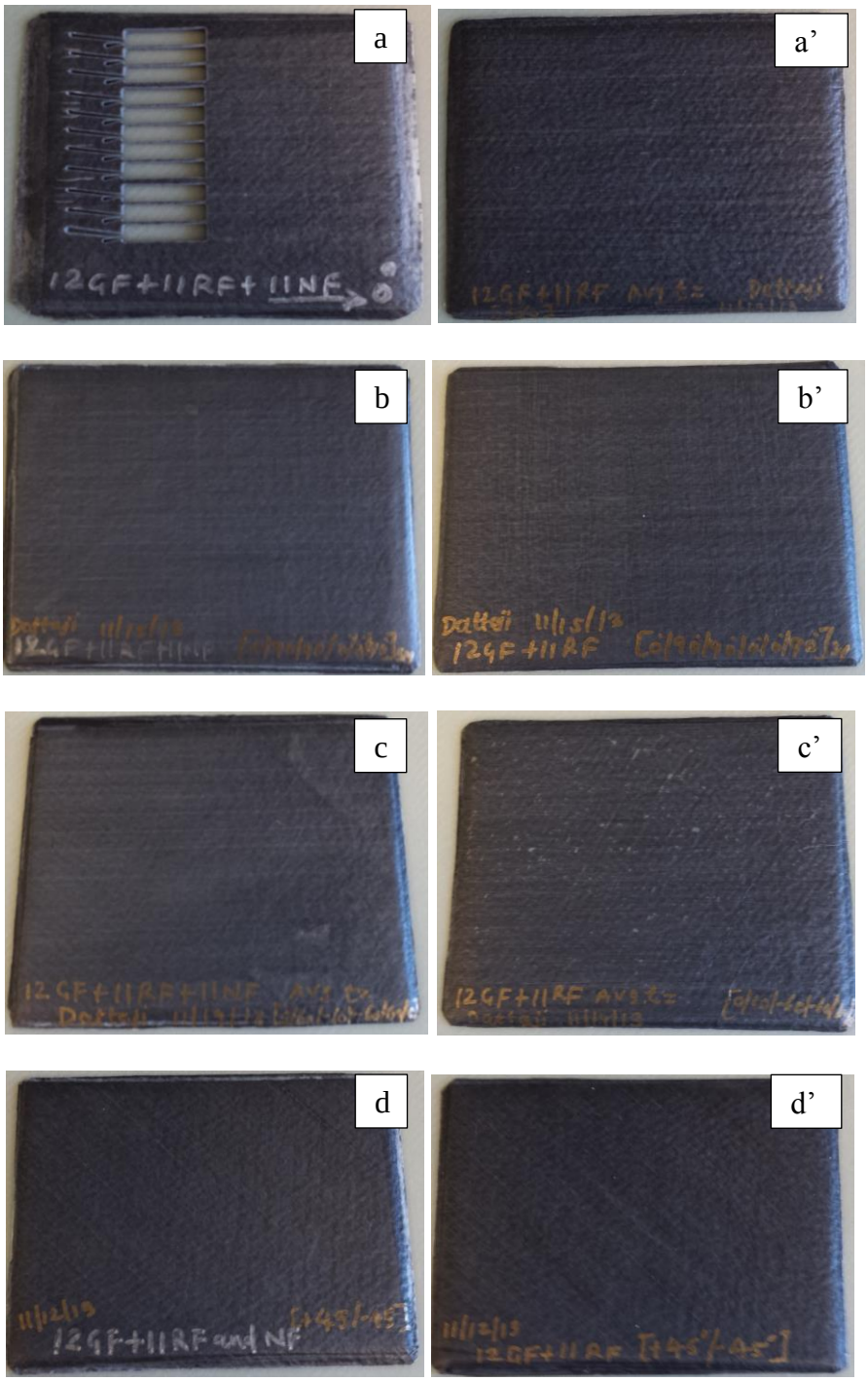


*Figure 4.4.* Fiberglass composite panels with and without TEOS ENFs mat for stacking sequences a , a') $[0/0/0/0/0/0]_s$ , b, b ')$[0/90/90/0/0/90]_s$, c, c ')$[0/60/-60/-60/60/0]_s$, and d, d ')$[+45/-45/45/-45/+45/-45]_s$

Each fabricated panel was weighted before and after curing and weights are shown in Table 4.2.In all four panels of hybrid composite sandwiched that were fabricated using TEOS ENFS non-woven mats, the nanofibers mats were sintered at sintered at 600 $^{0}$ C for 6 hours before the use. The weight of non-woven TEOS ENFs mats was maintained constant of 0.35g in each sheet and total weight of 11 sheets was 3.52g for all four hybrid fiberglass composite panels with different stacking sequences.

*Table 4.2* Weight of composite laminates before and after curing and loss of resin

| Stacking sequence | Composite Laminates | Weight of laminates (g) | | Loss of resin(g) |
|---|---|---|---|---|
| | | Before curing | After curing | |
| [0/0/0/0/0/0]s | 12 GF + 11RF | 170.1 | 160.9 | 9.2 |
| | 12 GF + 11RF + 11 ENFs | 220.7 | 214.8 | 5.9 |
| [0/90/90/0/0/90]s | 12 GF + 11RF | 193.3 | 186.4 | 6.9 |
| | 12 GF + 11RF + 11 ENFs | 197.4 | 190.0 | 7.4 |
| [0/60/-60/-60/60/0]s | 12 GF + 11RF | 188.08 | 180.03 | 8.05 |
| | 12 GF + 11RF + 11 ENFs | 194.3 | 187.5 | 6.8 |
| [+45/-45/45/-45/+45/-45]s | 12 GF + 11RF | 189.8 | 180.7 | 9.1 |
| | 12 GF + 11RF + 11 ENFs | 192.4 | 185.7 | 6.7 |

After visual inspection all panels were water jet cut to obtain the specimens according to the three point bend test ASTM D2344 standard(A. T. Standard, 2000), ASTM D2344 method is a modified short beam shear strength- MSBS test. From each panel 20 specimens were cut using water jet machine of the size 1.5 inches by 0.25 inches. Overall fiber volume fraction ratio of 12GF + 11RF+11ENF, and 12GF+11RF was 39.86%, and 38.21% respectively.

### 4.5 Short Beam Strength Test

According to the ASTM D 2344, the rate of crosshead movement of 1.0 mm (0.05 in.)/min was maintained throughout the test. The pan length of the specimen was 1 inch and the overhang length of the beam was 0.25 inches and width of specimen was 0.25 inches. The schematic diagram for the set up of three point bend test with modified short beam shear test is shown in Figure 4.5(A. T. Standard, 2000) . The laboratory set up to perform the three points bend test is shown in Figure 4.6.

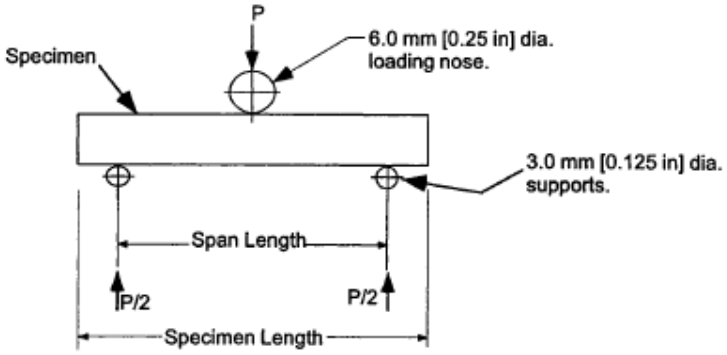


*Figure 4 5.* Schematic diagram for three points bend test

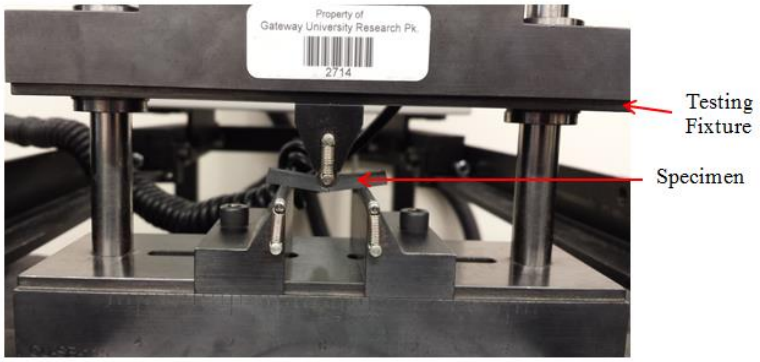


*Figure 4.6.*Three point bend test set-up on an Instron Machine

The short beam strength is calculated using the following equation

$$F^{sbs} = 0.75 * \frac{P_m}{b*h} \qquad (4.1)$$

Where:

$F^{sbs}$= short bean strength, MPa (psi);

$P_m$= maximum load observed during the test, N (lbf)

$b$= measured specimen width, mm (in), and

$h$ = measured specimen thickness, mm (in).

The test was performed for stacking sequence $[0/0/0/0/0/0]_s$, $[0/90/90/0/0/90]_s$, $[0/60/-60/-60/60/0]_s$, and $[+45/-45/45/-45/+45/-45]_s$ direction of fiberglass composites with and without TEOS ENFs. The three points bend test results of the 12 GF+ 11 RF composite and 12 GF+ 11 RF+ 11ENFs hybrid composite are shown in Tables 4.2 - 4.9, respectively. The behavior of the short beam under the three point bend test are shown for the stacking sequence $[0/0/0/0/0/0]_s$, $[0/90/90/0/0/90]_s$, $[0/60/-60/-60/60/0]_s$, and $[+45/-45/45/-45/+45/-45]_s$ are shown in Figures 4.7, 48, 4.9, and 4.10 respectively.

*Table 4.3* Short beam shear strength of 12GF+ 11RF fiberglass composite for $[0/0/0/0/0/0]_s$

| Specimen Number | Nanofibers Y/N? | Maximum Compressive load (lbf) | Area (in^2) | Short Beam Strength (psi) |
|---|---|---|---|---|
| G1 | N | 325.08 | 0.04378 | 5569.43 |
| G2 | N | 268.07 | 0.04378 | 4592.71 |
| G5 | N | 342.78 | 0.04462 | 5760.97 |
| G7 | N | 318.52 | 0.04446 | 5373.00 |
| G8 | N | 311.28 | 0.04386 | 5322.80 |
| Mean | | 301.84 | 0.04416 | 5126.45 |
| SD | | 37.18 | 0.00039 | 443.94 |

*Table 4.4* Short beam shear strength of 12GF+ 11RF +11 ENFs hybrid composite for $[0/0/0/0/0/0]_s$

| Specimen Number | Nanofibers Y/N? | Maximum Compressive load (lbf) | Area (in^2) | Short Beam Strength (psi) |
|---|---|---|---|---|
| N1 | Y | 335.78 | 0.04335 | 5809.31 |
| N2 | Y | 360.92 | 0.04463 | 6064.69 |
| N3 | Y | 325.38 | 0.04343 | 5618.51 |
| N5 | Y | 315.65 | 0.04412 | 5366.03 |
| N8 | Y | 314.25 | 0.04533 | 5199.75 |
| Mean | | 330.40 | 0.04417 | 5611.66 |
| SD | | 19.13 | 0.00083 | 344.36 |

*Table 4.5* Short beam shear strength of 12GF+ 11RF fiberglass composite for $[0/90/90/0/0/90]_s$

| Specimen Number | Nanofibers Y/N? | Maximum Compressive load (lbf) | Area (in^2) | Short Beam Strength (psi) |
|---|---|---|---|---|
| 1 | N | 296.17 | 0.04488 | 4949.90 |
| 3 | N | 265.19 | 0.04575 | 4347.43 |
| 4 | N | 270.45 | 0.04516 | 4491.58 |
| 5 | N | 269.24 | 0.04372 | 4618.74 |
| 6 | N | 262.44 | 0.04575 | 4302.27 |
| Mean | | 272.70 | 0.04505 | 4541.98 |
| SD | | 13.50 | 0.00084 | 259.87 |

*Table 4.6* Short beam shear strength of 12GF+ 11RF +11 ENFs hybrid composite for $[0/90/90/0/0/90]_s$

| Specimen Number | Nanofibers Y/N? | Maximum Compressive load (lbf) | Area (in^2) | Short Beam Strength (psi) |
|---|---|---|---|---|
| 1 | Y | 247.06 | 0.04473 | 4142.47 |
| 2 | Y | 229.90 | 0.04443 | 3881.02 |
| 3 | Y | 228.13 | 0.04350 | 3933.27 |
| 4 | Y | 230.50 | 0.04443 | 3891.26 |
| 5 | Y | 221.26 | 0.04425 | 3750.19 |
| 7 | Y | 220.46 | 0.04443 | 3721.75 |
| Mean | | 229.55 | 0.04429 | 3886.66 |
| SD | | 9.60 | 0.00042 | 150.65 |

*Table 4.7* Short beam shear strength of 12GF+ 11RF fiberglass composite for $[0/60/-60/-60/60/0]_s$

| Specimen Number | Nanofibers Y/N? | Maximum Compressive load (lbf) | Area (in^2) | Short Beam Strength (psi) |
|---|---|---|---|---|
| 1 | N | 125.00 | 0.04312 | 2173.85 |
| 2 | N | 120.74 | 0.04242 | 2134.83 |
| 3 | N | 118.55 | 0.04301 | 2067.18 |
| 4 | N | 99.89 | 0.04242 | 1766.11 |

Table 4.7 Short beam shear strength of 12GF+ 11RF fiberglass composite for $[0/60/-60/-60/60/0]_s$ *Cont.*

| Specimen Number | Nanofibers Y/N? | Maximum Compressive load (lbf) | Area (in^2) | Short Beam Strength (psi) |
|---|---|---|---|---|
| 5 | N | 102.50 | 0.04192 | 1834.06 |
| 7 | N | 105.83 | 0.04326 | 1834.72 |
| Mean | | 112.09 | 0.04269 | 1968.46 |
| SD | | 10.61 | 0.00052 | 176.91 |

*Table 4.8* Short beam shear strength of 12GF+ 11RF +11 ENFs hybrid composite $[0/60/-60/-60/60/0]_s$

| Specimen Number | Nanofibers Y/N? | Maximum Compressive load (lbf) | Area (in^2) | Short Beam Strength (psi) |
|---|---|---|---|---|
| 1 | Y | 116.89 | 0.04394 | 1995.03 |
| 2 | Y | 95.92 | 0.04275 | 1682.91 |
| 3 | Y | 106.27 | 0.04386 | 1817.18 |
| 4 | Y | 104.44 | 0.04356 | 1798.10 |
| 5 | Y | 97.05 | 0.04398 | 1654.91 |
| 8 | Y | 92.38 | 0.04326 | 1601.46 |
| Mean | | 102.16 | 0.04356 | 1758.26 |
| SD | | 8.93 | 0.00048 | 142.87 |

*Table 4.9* Short beam shear strength of 12GF+ 11RF fiberglass composite for $[+45/-45/45/-45/+45/-45]_s$

| Specimen Number | Nanofibers Y/N? | Maximum Compressive load (lbf) | Area (in^2) | Short Beam Strength (psi) |
|---|---|---|---|---|
| 1 | N | 140.97 | 0.04405 | 2400.17 |
| 2 | N | 133.04 | 0.04271 | 2335.92 |
| 3 | N | 141.82 | 0.04503 | 2361.80 |
| 4 | N | 126.01 | 0.04355 | 2170.15 |
| 5 | N | 124.19 | 0.04275 | 2178.78 |
| 6 | N | 125.47 | 0.04364 | 2156.28 |
| 7 | N | 127.68 | 0.04419 | 2167.13 |
| Mean | | 131.31 | 0.04370 | 2252.89 |
| SD | | 7.44 | 0.00082 | 107.60 |

*Table 4.10* Short beam shear strength of 12GF+ 11RF +11 ENFs hybrid composite $[+45/-45/45/-45/+45/-45]_s$

| Specimen Number | Nanofibers Y/N? | Maximum Compressive load (lbf) | Area (in^2) | Short Beam Strength (psi) |
|---|---|---|---|---|
| 1 | Y | 142.36 | 0.04460 | 2393.72 |
| 2 | Y | 126.52 | 0.04305 | 2204.08 |
| 3 | Y | 126.77 | 0.04288 | 2217.13 |

Table 4.10 Short beam shear strength of 12GF+ 11RF +11 ENFs hybrid composite [+45/-45/45/-45/+45/-45]s Cont.

| Specimen Number | Nanofibers Y/N? | Maximum Compressive load (lbf) | Area (in^2) | Short Beam Strength (psi) |
|---|---|---|---|---|
| 4 | Y | 129.91 | 0.04377 | 2226.06 |
| 5 | Y | 120.12 | 0.04394 | 2050.12 |
| 6 | Y | 119.53 | 0.04415 | 2030.60 |
| Mean | | 127.54 | 0.04373 | 2186.95 |
| SD | | 8.32 | 0.00066 | 133.15 |

**4.6 Effect of TEOS ENFs on Short Beam Strength of Laminated Fiberglass Composite**

After testing all four types of specimens, the behavior of the specimens under three point bending is plotted as short beam strength vs transverse displacement. The results of the short beam strength of the fiberglass prepreg composite with and without TEOS ENFs interleaving is shown in Figure 4.11 The strain energy absorbed in each sequence of stacking fiberglass is more in case of interleaving of TEOS ENFs before it fails is shown in Figure 4.7, 4.8, 4.9, and 4.10 . The fractography examination of the failed specimens gives the type of failure mechanics and energy absorbed before complete failure. Load displacement for $[0/0/0/0/0/0]_s$, $[0/90/90/0/0/90]_s$, $[0/60/-60/-60/60/0]_s$, and $[+45/-45/45/-45/+45/-45]_s$ orientation of are shown in Figure 4.6, 4.7, 4.8, and 4.9 respectively.

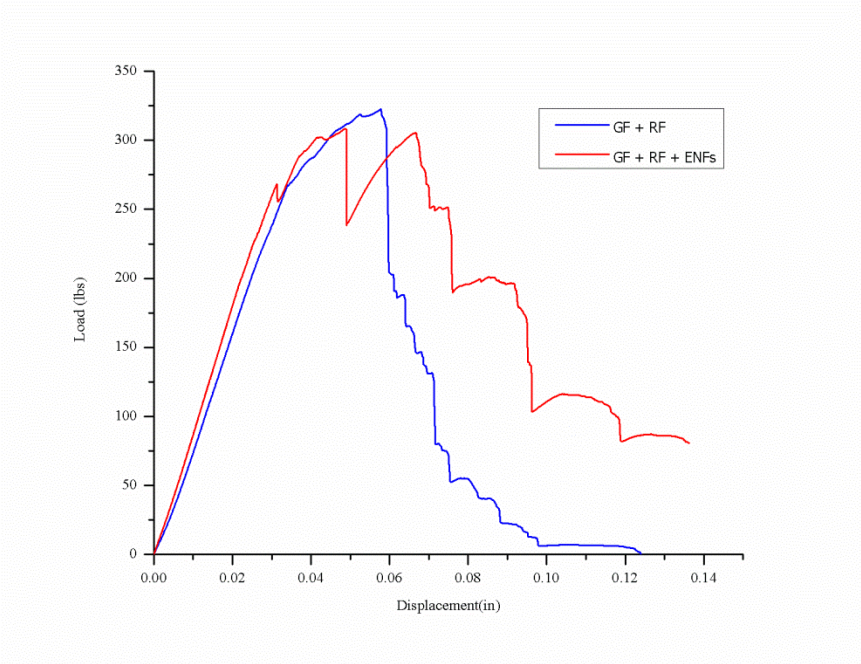


*Figure 4.7.* Behavior of Short beam under the three point bend loading for fiberglass composite with and without ENFs for $[0/0/0/0/0/0]_s$

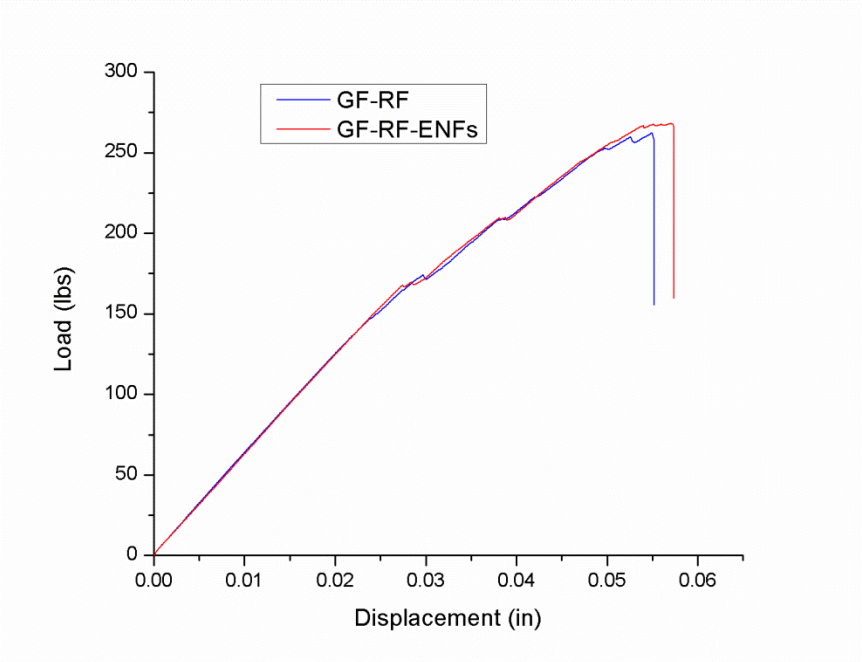


*Figure 4.8.* Behavior of short beam under three point bend loading for fiberglass composite with and without ENFs for $[0/90/90/0/0/90]_s$

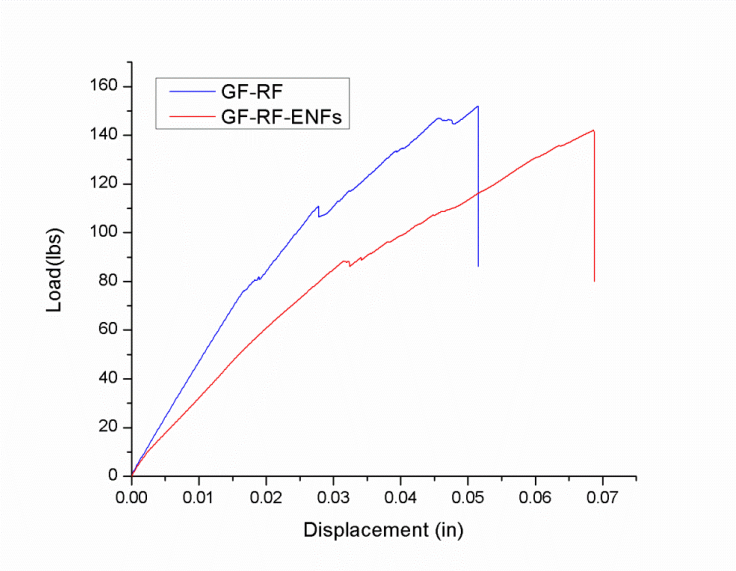


*Figure 4.9.* Behavior of short beam under three point bend loading for fiberglass composite with and without ENFs for $[0/60/-60/-60/60/0]_s$

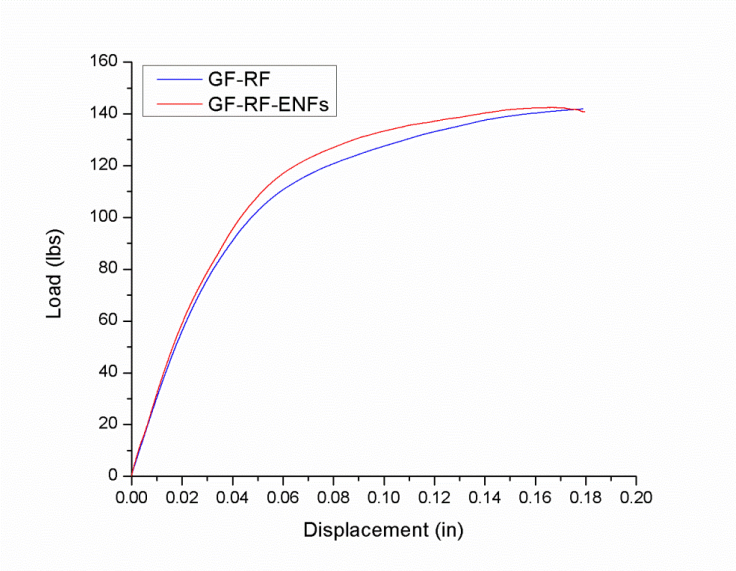


*Figure 4.10.* Behavior of short beam under three point bend loading for fiberglass *composite* with and without ENFs for [+45/-45/45/-45/+45/-45]s

The short beam strength of composite with electrospun TEOS nanofibers were compared with the result available in literature and is shown in Table 4.11(Kelkar et al., 2008). The and the

comparison shows that the present results well agreed well with the results available from the literature for the stacking sequence of $[0]_s$.

*Table 4.11* Computation of Short Beam Strength

| Sample | Avg. Short Beam Strength (psi) |
|---|---|
| Set - I for three specimen as per MSBS without nanofibers | 5.51E+03 |
| Set - II for three specimen as per MSBS with nanofibers cured at 300 $^0$ C | 5.17E+03 |
| Set - III for three specimen as per SBS with nanofibers cured at 900° C per MSBS | 6.42E+03 |
| Set - IV for four specimen as per MSBS with nanofibers cured at 900 $^0$ C | 7.01E+03 |

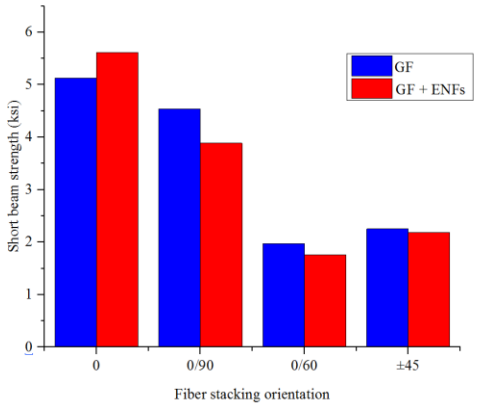


*Figure 4.11.* Comparison of short beam strength fiberglass prepreg composite with and without TEOS ENFs interleaving

Comparison of the short beam strength of the fiberglass woven composite with and without TEOS ENFs, showed that the in 0 $^0$ direction of unidirectional laminated fiberglass

composite, short beam strength is improved with the presence of nanofibers. These results were comparable to the one available in the literature, where an improvement of 16% was reported in short beam strength when beam was interleaved with nanofibers.

The strain energy (area under the load-displacement curve) is more for the laminates with the presence of nanofibers mats and this may be due to the interlocking mechanism of nanofibers through thickness of the laminates creating a strong adhesive bond between the two fiberglass plies. Further, the additional layer of resin film plays significant role to resulting into a strong adhesive bond and help to avoid the dry area of the TEOS ENFs during the curing reaction.

### 4.6.1 Fractography of Failed MSBS Specimens

Fractography is a method used for detailed analysis of a fracture surface to determine the cause of the fracture and the relationship of the fracture mode to the micro and macro structure of the material. Fractography techniques are used to find the crack initiation and to determine what type of loading and/or outside forces that caused the crack to initiate.
It also helps to determine the direction of crack propagation. Other data can also be extracted such as structure-property relationship involving strength and failure of materials. Fractography provides useful information in evaluating new materials and in defining their response to mechanical, chemical, and thermal environments(Cheremisinoff et al., 1995).

Optical images of the failed MSBS specimens of fiberglass composite with resin film and fiberglass composite with TEOS ENFS sandwiched between the two prepreg of the fiberglass and resin film are shown in Figures 4.12 and 4.13 respectively.

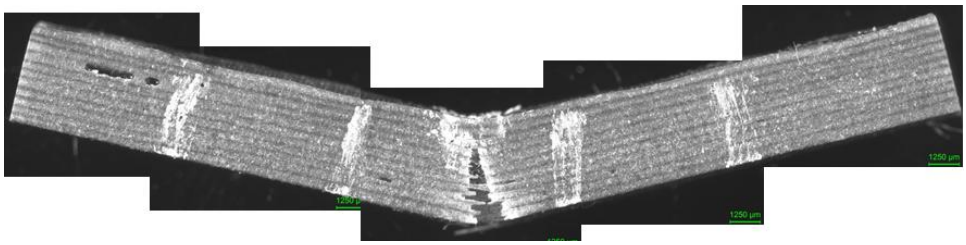

*Figure 4.12.* Optical image of fiberglass prepreg with resin film composite

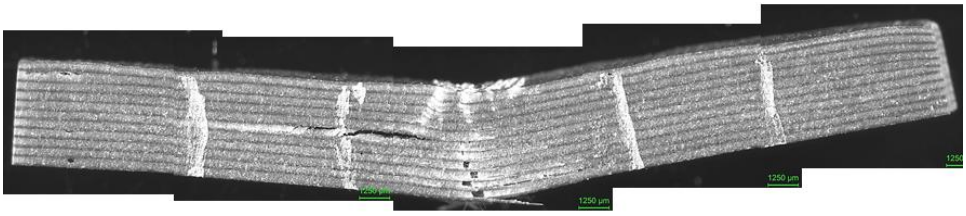

*Figure 4.13.* Optical image of fiberglass prepreg sandwiched with TEOS ENFs and additional resin film in a composite

#### *4.6.1.1 Sample preparation*

The failed specimens from three point bend test were cut at the middle section of the specimen where the major failure was visible using the diamond cutter model 650 low speed diamond wheel saw, supplied by South Bay Technology Inc., as shown in Figure 4.14 and specimens with ethanol and dried.

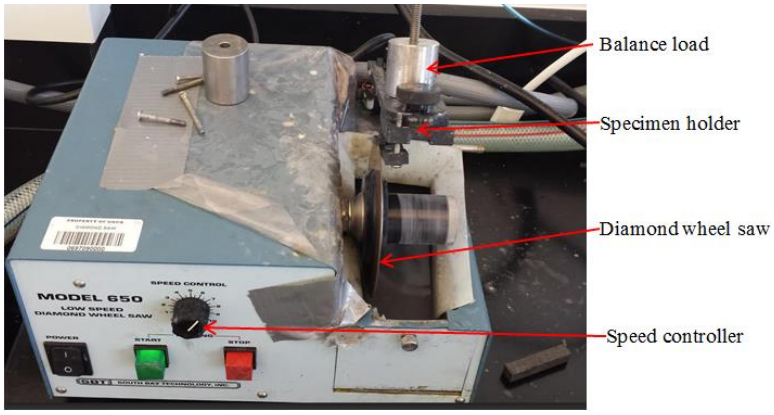


*Figure 4.14.* Diamond wheel saw for composite specimens for SEM sample preparation

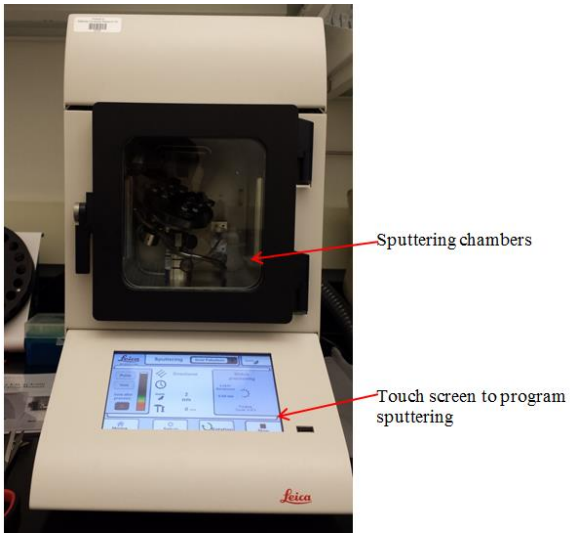


*Figure 4.15.* Sputtering machine for metal coating on the specimen

The samples were prepared for the scanning electron microscope (SEM) examination. The samples were cut to fit exact spokes used in the SEM machine fixture. Since the specimens were non-conductive, the conductive coating was necessary on the failed surface. For all specimens, the gold palladium coating of 3-4nm was applied using the sputtering machine supplied by Leica Inc. as shown in Figure 4.15.

#### *4.6.1.2 SEM imaging of failed specimens*

The SEM imaging was performed using the scanning electron microscope supplied by Zeiss model EVOLS10. The SEM images shown in Figure 4.16a-g are the fractography of progressive failures of images of the fiberglass specimens of all $0^0$ orientation which were subjected to 40% to 90% of the maximum applied load.

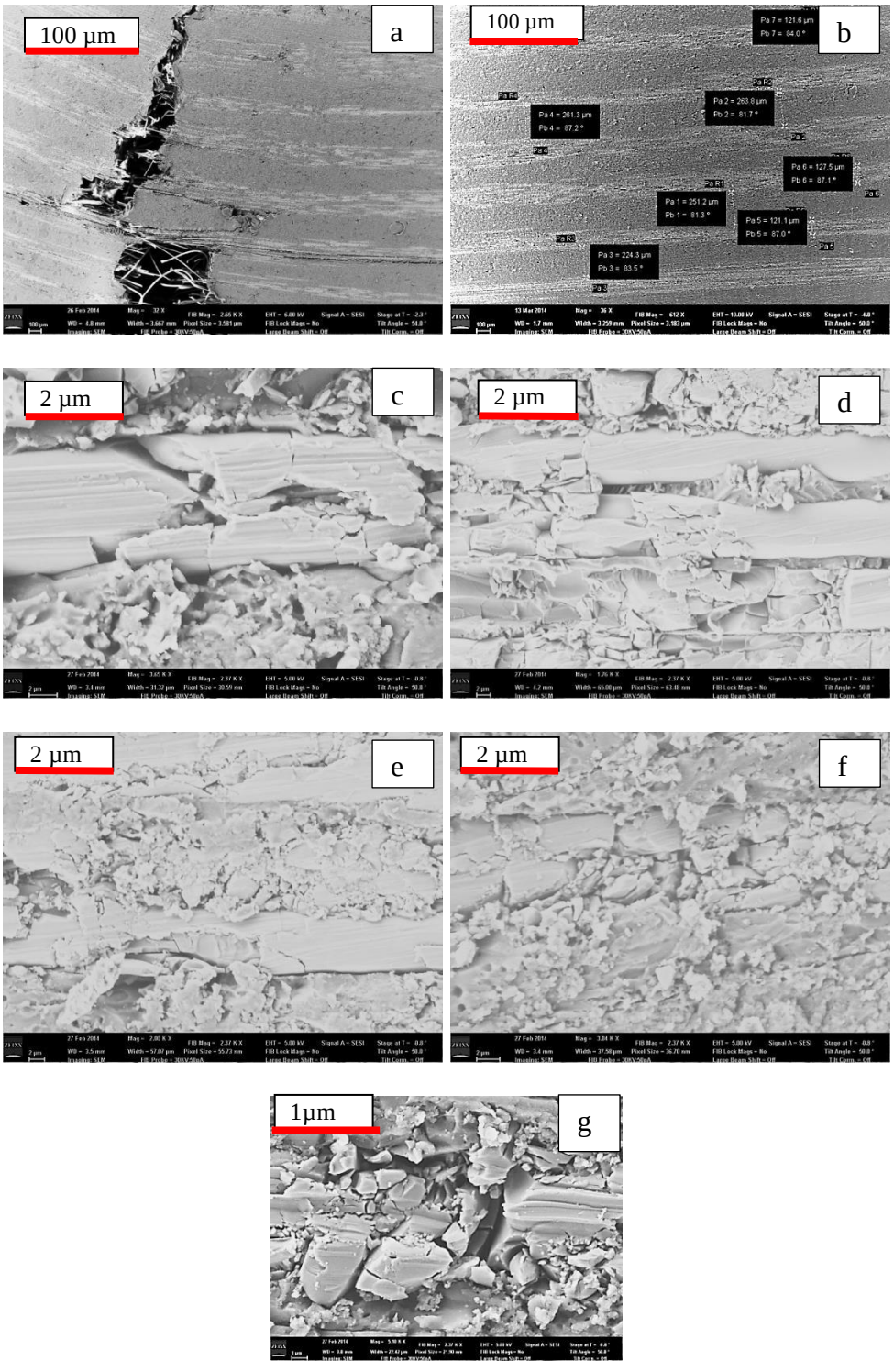


*Figure 4.16.* SEM images of failed specimens of fiberglass prepreg composite a) through the thickness penetration b) 40% load, c) 50% load, d) 60% load, e) 70% load, f) 80% load, and g) 90% of maximum load

The SEM images shown in Figure 4.17 a-g are the fractography progressive failures images of specimens of all $0^0$ orientations of fiberglass with through thickness head displacement, and 40 to 90% of the maximum load applied to fiberglass prepreg with TEOS ENFs composite specimen.

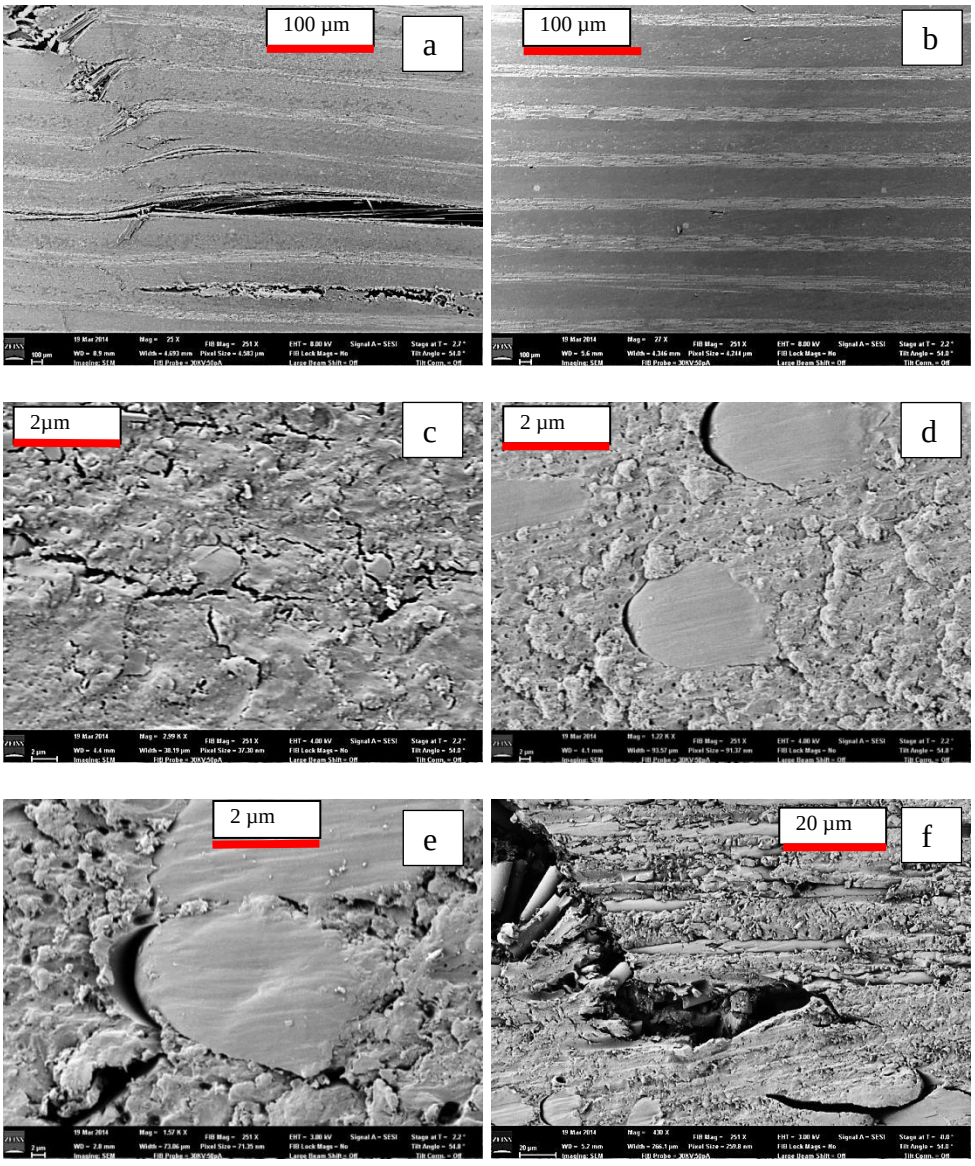

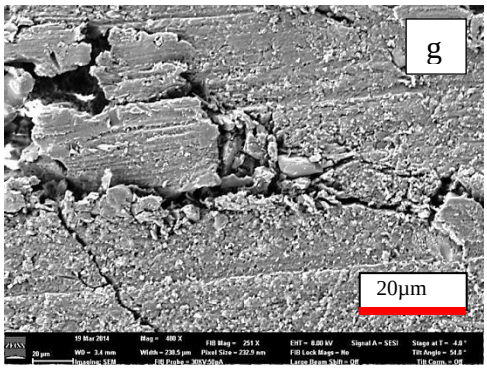


*Figure 4.17.* SEM images of failed specimens of fiberglass prepreg with TEOS ENFs composite a) through the thickness penetration, b) 40% load, c) 50% load, d) 60% load, e) 70% load, f) 80% load, and g) 90% of maximum load

The SEM images shown in Figure 4.18a-g are the fractography progressive failures images of specimens of all $0^0/90^0$ orientations of fiberglass with through thickness head displacement, and 40 to 90% of the maximum load applied to the fiberglass prepreg composite specimen.

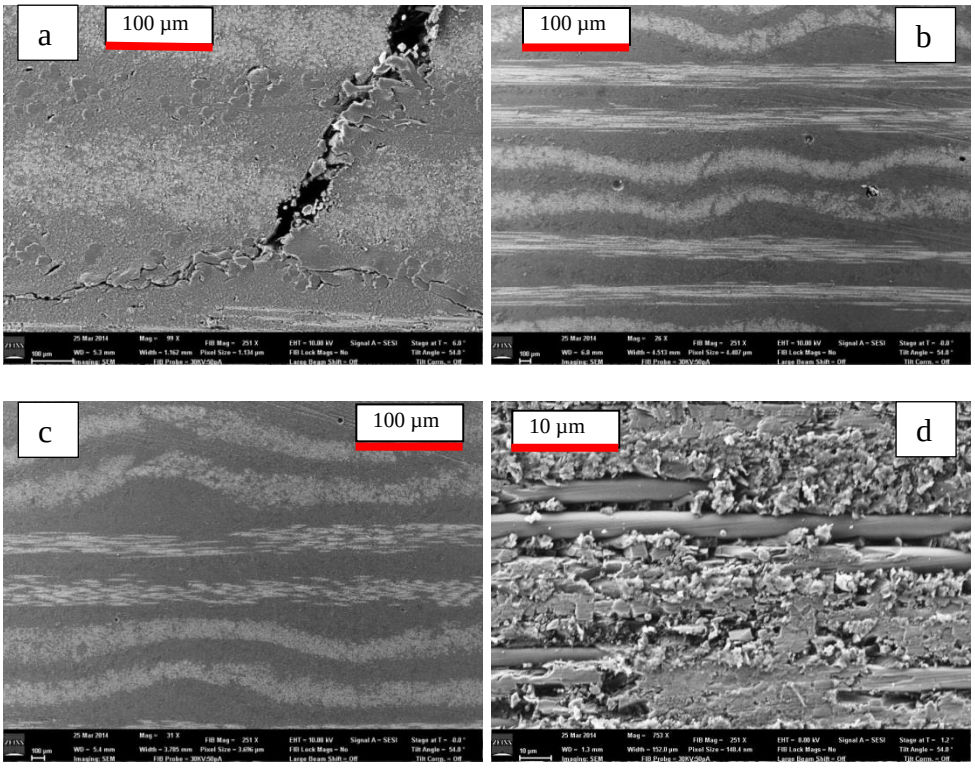

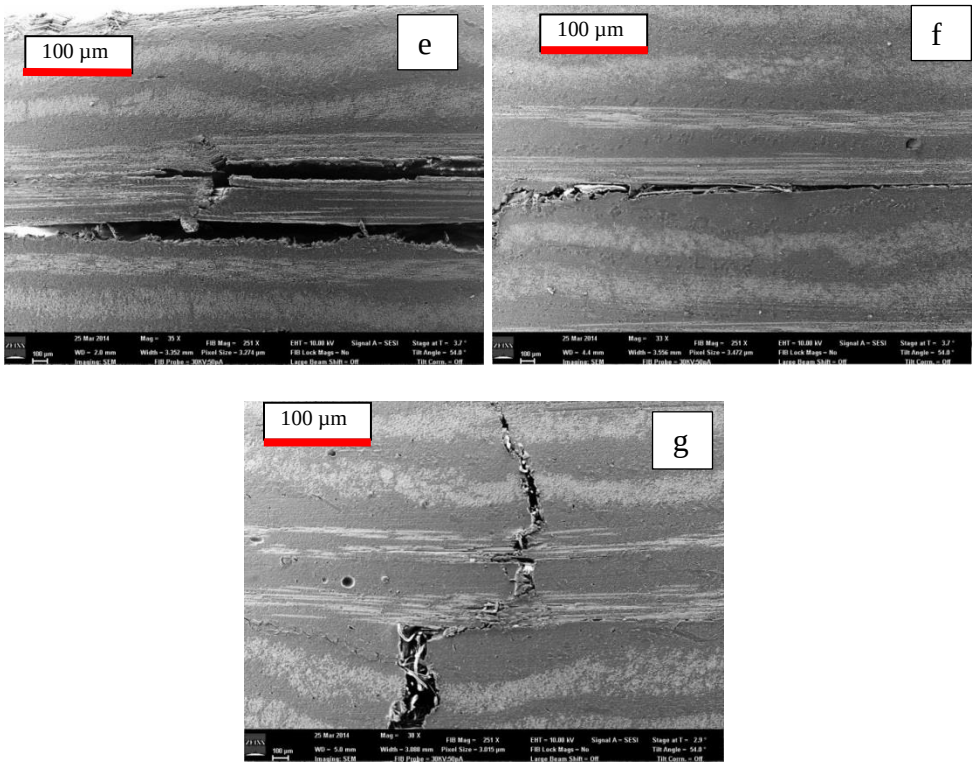


*Figure 4.18.* SEM images of failed specimens of fiberglass prepreg $0^0/90^0$ orientation composite a) maximum load, b) 40% load, c) 50% load, d) 60% load, e) 70% load, f) 80% load, and g) 90% of maximum load

The SEM images shown in Figure 4.19 a-g presents the progressive failure for specimens with orientation of $0^0 / 90^0$ with TEOS ENFs through the thickness penetration, and 40% to 90% of the applied maximum load.

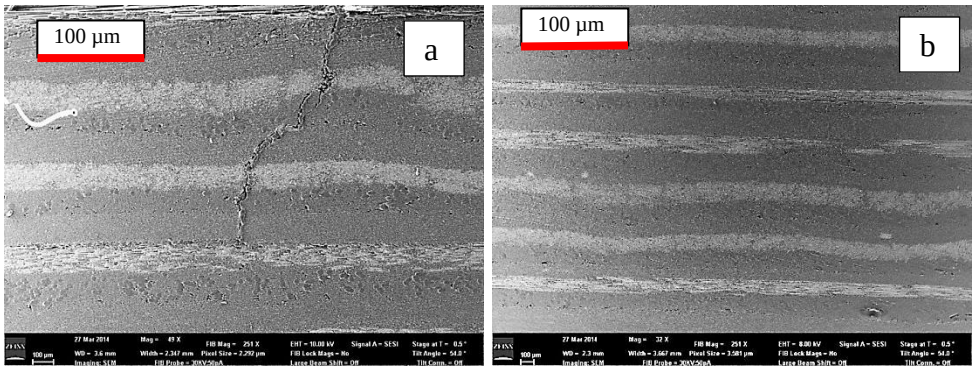

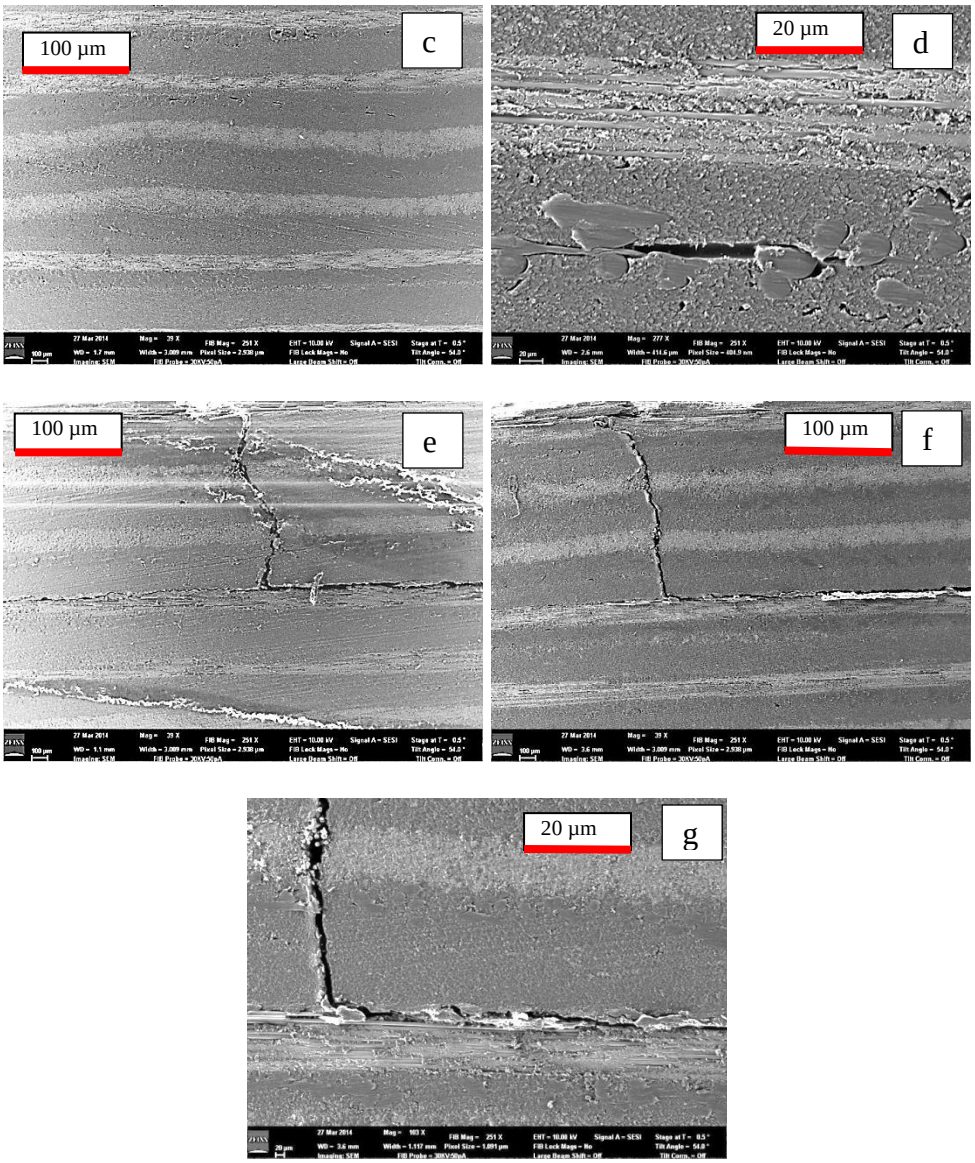


*Figure 4.19.* SEM images of failed specimens of fiberglass prepreg $0^0/90^0$ orientation with TEOS ENFs composite a) maximum load, b) 40% load, c) 50% load, d) 60% load, e) 70% load, f) 80% load, and g) 90% of the maximum load.

The SEM images shown in Figure 4.20 a-g presents the progressive failure for specimens with orientation of $0^0/60^0$ with TEOS ENFs through the thickness penetration, and 40% to 90% of the applied maximum load.

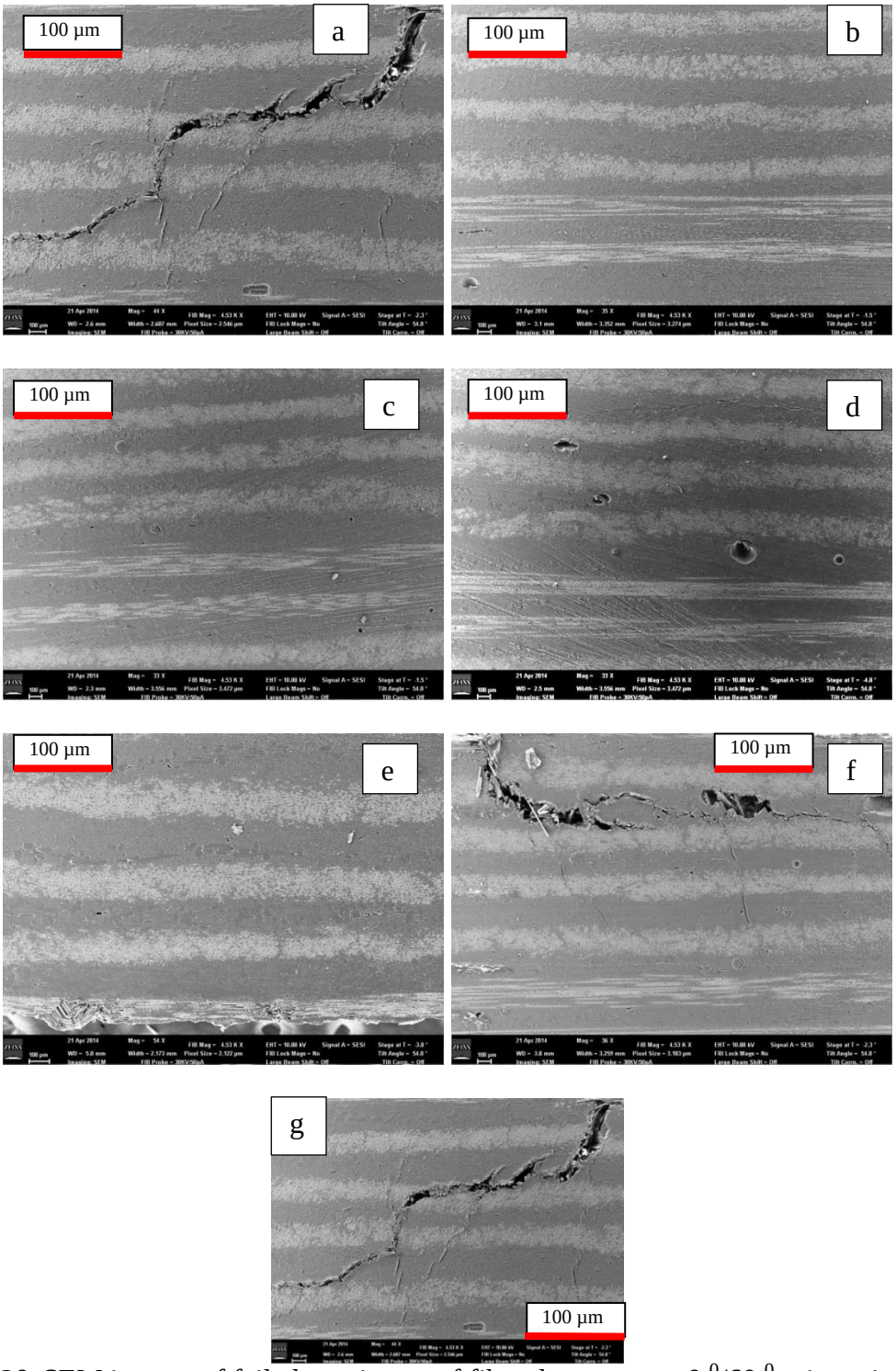


*Figure 4. 20.* SEM images of failed specimens of fiberglass prepreg $0^{0}/60^{0}$ orientation composite a) maximum load, b) 40% load, c) 50% load, d) 60% load, e) 70% load, f) 80% load, and g) 90% of the maximum load

The SEM images shown in Figure 4.21 a-g presents the progressive failures for specimens with orientation of $0^0/60^0$ with TEOS ENFs through the thickness penetration, and 40% to 90% of the applied maximum load.

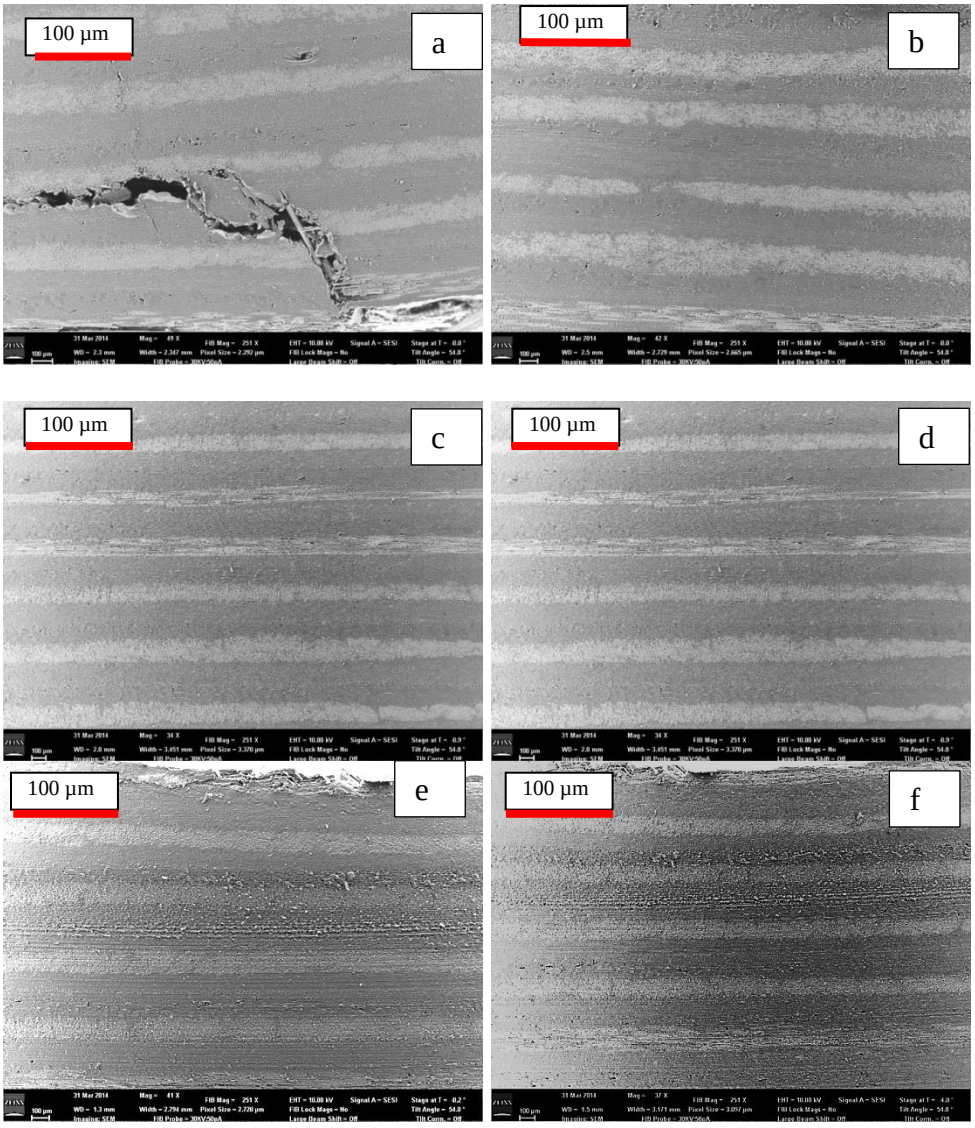

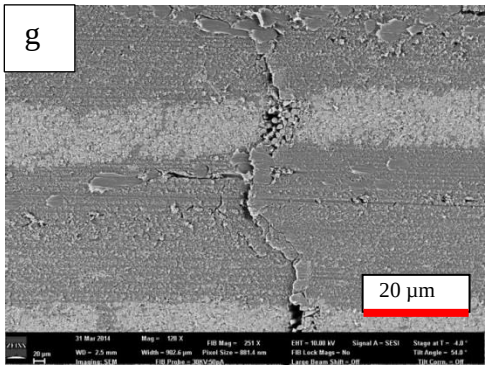


*Figure 4.21.* SEM images of failed specimens of fiberglass prepreg with TEOS ENFs $0^0/60^0$ orientation composite a) maximum load, b) 40% load, c) 50% load, d) 60% load, e) 70% load, f) 80% load, and g) 90% of the maximum load

The SEM images shown in Figure 4.22 a-b presents the progressive failures for specimens with orientation of $\pm 45^0$ without TEOS ENFs through the thickness penetration, and 90% of the applied maximum load.

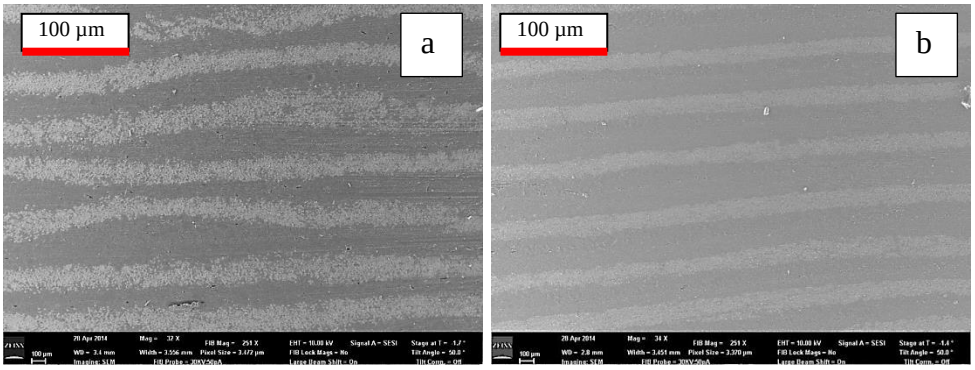


*Figure 4.22.* SEM images of failed specimens of fiberglass prepreg composite a) through thickness, b) 90% of maximum load

The SEM images shown in Figure 4.23 a-b presents the progressive failures for specimens with orientation of $\pm 45^0$ with TEOS ENFs through the thickness penetration, and 90% of the applied maximum load.

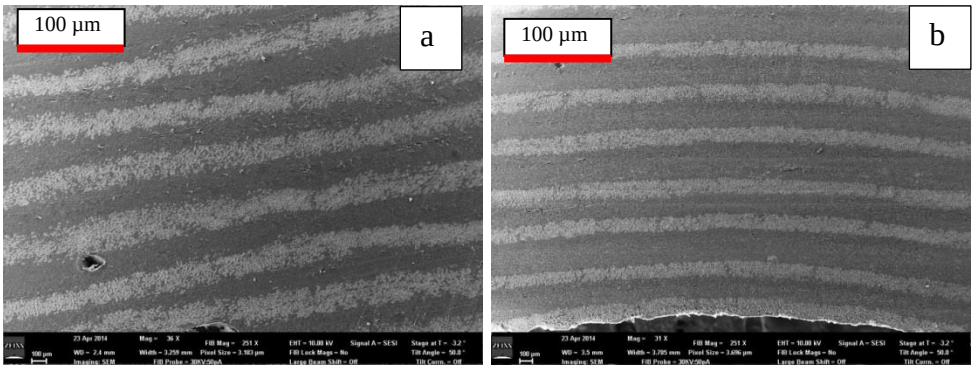


*Figure 4.23.* SEM images of failed specimens of fiberglass prepreg with TEOS ENFs composite a) through thickness the head displacement, b) 90% of maximum load

**4.7 Conclusions**

Following conclusions are noted after performing the experimental study for short beam strength of the fiberglass prepreg composites with and without TEOS ENFs.

1. To ensure wetting of interleaved nanofibers mats, one ply of resin film sheet and one TEOS ENFs sheet was sandwiched between two fiberglass prepreg. The composite panel was then fabricated using out of autoclave vacuum bagging process.
2. Four different symmetric ply orientations were to investigate effect of nanofibers mats on the short beam strength of the laminates.
3. Thickness of each ply in the composite panel was evaluated using SEM imaging and found fiberglass ply thickness was 0.00627 inches, epoxy resin film thickness was of 0.00802 inches
4. The energy absorbed by the fiberglass composites with TEOS ENFs during the failure was more, for all four stacking sequences as compared to the energy absorbed by corresponding composite laminates without TEOS ENFs.
5. The progressive failure of the specimens was investigated and the corresponding SEM images were captured, to analyze the mode of fracture at each load.

6. Fractographic examination of the failed specimens revealed that the failure modes in fiberglass composites with and without presence of TEOS nanofibers were entirely different. In the case of fiberglass laminates with the presence of TEOS nanofibers, failure initiated in the interlaminar region in the form of nanofibers mat failures leading to delaminations. On the other hand the failure in conventional fiberglass composites the failure occurred due to transverse shear cracking.

Next chapter will present detailed 3-D finite element model of the fiberglass composites with and without presence of nanofibers mats. This chapter also presents comparison of experimental and finite element results

# CHAPTER 5

## Finite Element Modeling and Analysis for Short Beam Strength of the Laminated Fiberglass Composites

### 5.1 Introduction

Every day in the area of composite technology new materials are developed or the materials are being designed using different nanomaterials, to enhance the properties of the hybrid composites. It is time consuming and expensive to test all the new materials which are designed and fabricated using nanomaterials. Thus there is need for the powerful tool to analyze the properties of nanoengineered composite materials using analytical methods. The failure of nanocomposites can provide insight for the effects of nanomaterials on the properties of nanoengineered composites.

Classical laminate theory (CLT) is well established as a method to compute the properties of the multidirectional laminates, However CLT is based upon two dimensional analyses and in real life stresses are three dimensional. In composites materials typical failure occur due to matrix cracking, fiber failure and delamination. For the complete understanding of the progressive failure mechanism in composite requires consideration of all the three dimensional properties and stresses. The closed form solutions are too complex for textile composites, alternate is detailed 3-D finite element analysis. The finite element method is fairly accurate and is the most elegant method of modeling complex three –dimensional fiberglass composites. This chapter presents detailed of 3-D finite element modeling and analysis to simulate the progressive failures in laminated composites for three points bend test to study the effects of TEOS ENFs on short beam strength of the hybrid composites. The models were developed using ANSYS finite element software and details are provided in the next section.

## 5.2 Solid 186 Element Model Validation

The element used in the presents ANSYS model was SOLID186, which is a higher order 3-D 20-node solid element that exhibits quadratic displacement behavior. The element is defined by 20 nodes having three degrees of freedom per node: translations in the nodal x, y, and z directions as shown in Figure5.1.

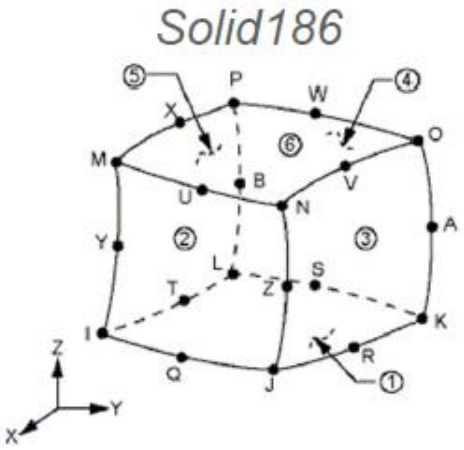


*Figure 5.1.* Solid 186 homogenous structural solid geometry

### 5.2.1 Validation of Solid 186 using Aluminum material beam

A three dimensional finite element model with dimension of 1.5 inches(along X) by 0.25 inches(along Y) by 0.175 inches (along Z) of aluminum with modulus of elasticity, E = 10 Msi, Poisson's ratio ν = 0.33 was created using ANSYS 14.0 as shown in Figure 5.1. Following the boundary conditions was applied:

At x= 0.25", z=0" and x= 1.25", z = 0" along y-axis, displacement Uz =0,

At y = 0.125", along x-axis Uy = 0" and at, x=0.75", y = 0.125"

At z = 0.0875" Ux = 0 and line force of value 300 lb was applied at x = 0.75", z = 0.175" s as shown Figure 5.2. The maximum deflection of the beam was calculated using close form as

shown in equation 5.1 and is compared with the solution obtained using ANSYS and is shown in Figure 5.3.

$$\delta = \frac{PL^3}{48EI} = \frac{300(1)^3}{48*10^7\frac{1}{12}*0.25*0.175^3} = 0.006563 \text{ inches} \quad (5.1)$$

And the deflection from nodal solution is $\delta = 0.006585\ inches$.

Since the deflections were in excellent agreement it was decided to use 3-D SOLID 186 elements to model the fiberglass laminates with and without TEOS nanofibers.

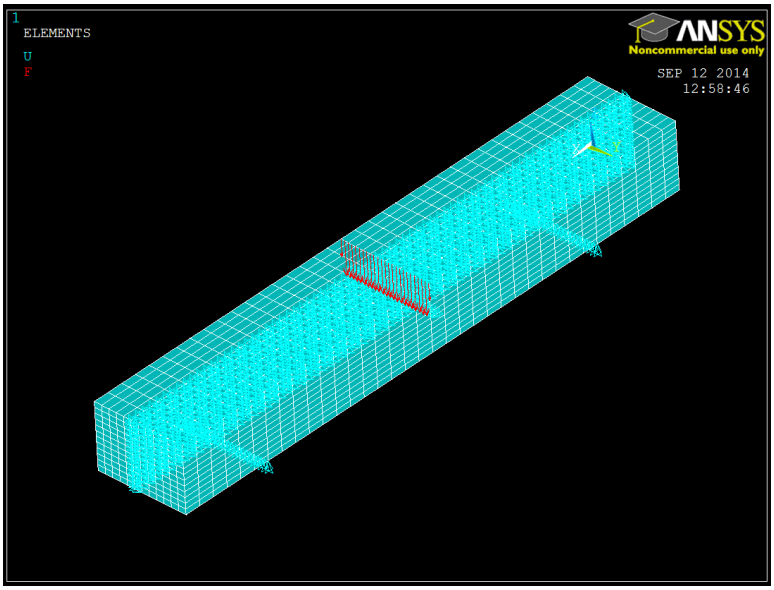


*Figure 5.2.* 3D finite element model for aluminum beam with boundary conditions

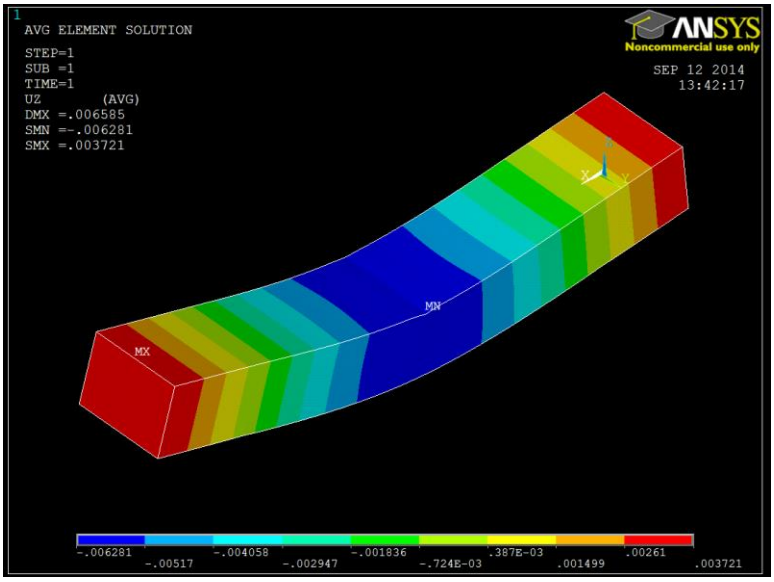


*Figure 5.3.* Deflection of 3D finite element model for aluminum beam with boundary conditions

### 5.2.2 Validation of Solid186 element for fiberglass composite model

A detailed 3-D finite element model of fiberglass composite was developed using 3-D SOLID 186 elements. Using classical laminate theory, the properties of hybrid composites were determined. The classical laminate theory was then used to determine equivalent modulus of elasticity and bending stiffness of the hybrid composite beam. These properties were then used to determine the closed form solution for the composite beam and results were then compared with the solution obtained using 3-D finite element model. The deflection of beam using load equal to $F_z$ = 300 lb for GF-RF and GF-RF and ENFs is shown in Table 6.1. Both deflections were matched and hence verified deflection as shown in Table 5.1.

*Table 5.1* Apparent laminate stiffness properties from laminator analysis and deflection of beam

| Material | $E_{XB}$ (Msi) | FEM- deflection (in) | Equivalent $I_x$ ($in^4$) | Deflection by $\delta = \frac{PL^3}{48EI}$ (in) |
|---|---|---|---|---|
| GF-RF | 3.026 | 0.0392 | 5.7999e-5 | 0.03905 |
| GF-RF and ENFs | 3.173 | 0.0346 | 5.0445e-5 | 0.03561 |

**5.3 Validation of 3D Model for Short Beam Subjected to Uniaxial Loading**

To validate SOLID186 element for three dimensional stress analysis, in the present work an analytical method used for prediction of interlaminar stresses of laminated composite under uniform axial deformation by Yang, and Chen research work (Yang et al., 2013) was chosen.

A solid three dimensional model finite element model was created using dimension of 6 inches by 1 inch by 0.1 inches in size with four laminates of fiberglass prepreg and three laminates of epoxy resin film as shown in Figure 5.4. The composite was divided into 4 fiberglass prepreg laminates and 3 resin film laminates for 0.1 inches of thickness and a solid three dimensional model was created. The model had 77461 and 13824 elements. Following boundary conditions were applied and are shown in the follows and shown in the model in Figure 5.5.

On z face nodes at x= 0, applied x-displacement, $U_x$= 0,

On z-face nodes at x= 6 inches, applied constant strain, x displacement, $U_x$ = 0.5 inches

At y = 0.5 inches and z = 0.05inces all nodes, applied y-displacement $U_y$ =0.

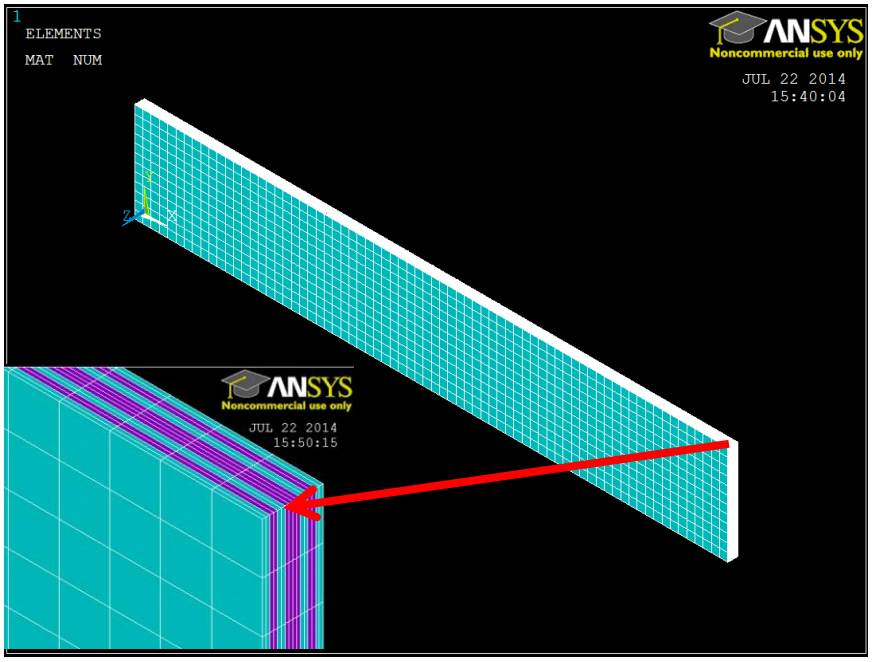


*Figure 5.4.* 3D finite element model with 4 GF and 3 RF

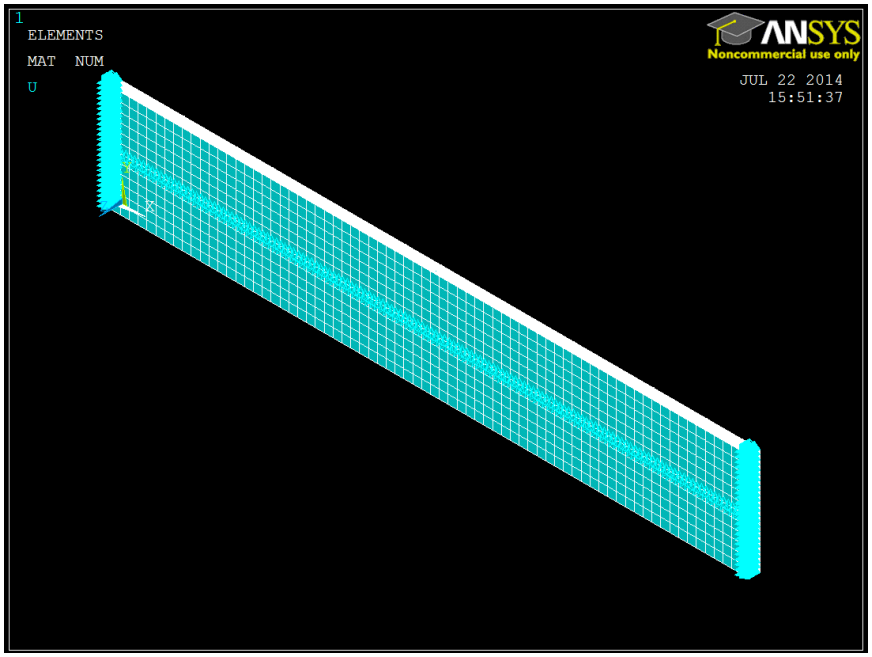


*Figure 5.5.* 3D finite element model with 4 GF and 3 RF and with boundary conditions

### 5.3.1 Distribution of stresses along z-axis

The distributions of stresses from Yang, and Chen paper, $(\sigma_z, \sigma_{xz}, \sigma_{yz})$ along *y*-axis at $z = 0$ and $z = h/2$ of the cross-ply laminated composite plate ($[0/90]_s$) are shown in Figures 5.6 and 5.7. The results are in accordance with the quasi-3D element method (Chorng-Fuh et al., 1993).

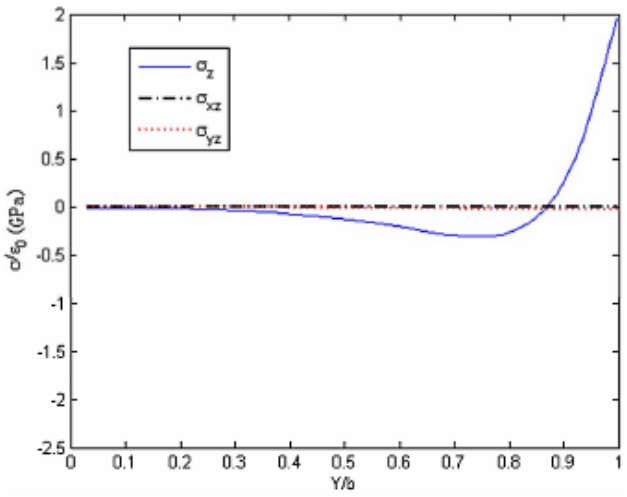


*Figure 5.6.* The stresses along y-axis, z = 0, ($[0/90]_s$)

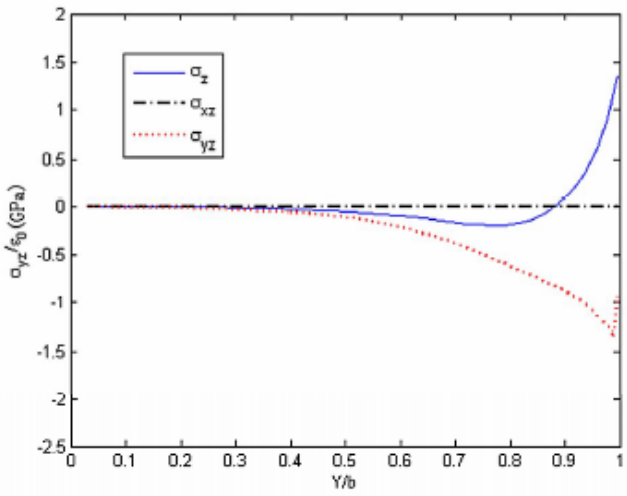


*Figure 5.7.* The stresses along y-axis, z = h/2, ($[0/90]_s$)

Using the present 3-D finite element model, various values of interlaminar stresses were determined and are presented in in Figure 5.8 and 5.9. These values were compared to the stresses given by Yang, and Chen (Yang et al., 2013) as shown Figures 5.6 and 5.7.

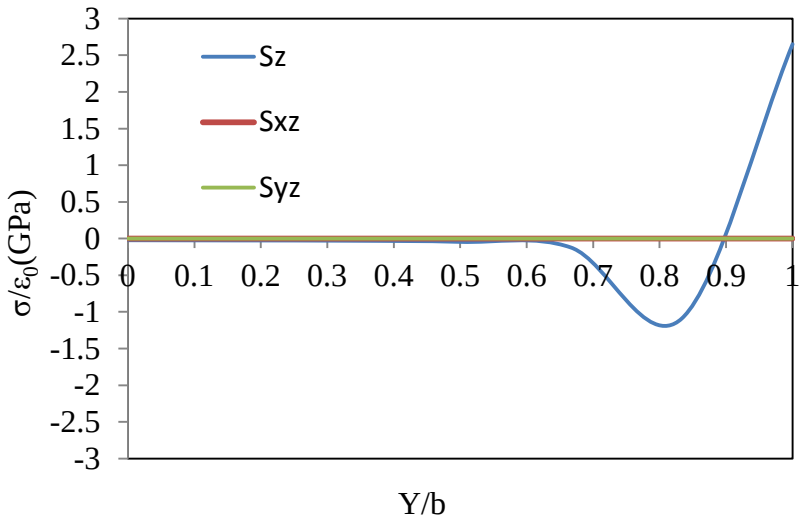


*Figure 5.8.* The stresses along y-axis, z = 0, $([0/90]_s)$ at $U_x$ =0.5 inches

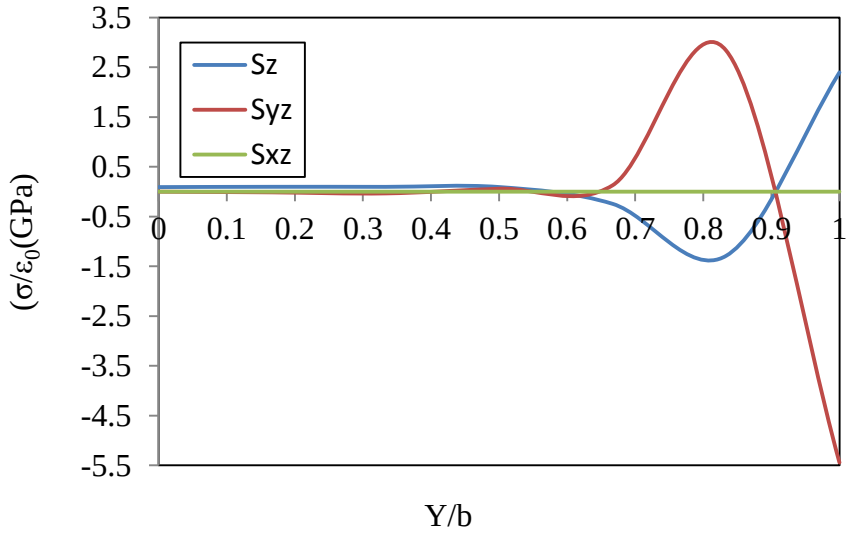


*Figure 5.9.* The stresses along y-axis, z = h/2, $([0/90]_s)$ at $U_y$ =0.5 inches

The comparison of the distributions of stresses $(\sigma_z, \sigma_{xz}, \sigma_{yz})$ and $(S_z, S_{xz}, S_{yz})$ along *y*-axis at $z = 0$ and $z = h/2$ of the cross-ply laminated composite $([0/90]_s)$ from Figures 5.5and 5.6 and Figures 5.8 and5.9, at the interface $z = 0$ or $z = h/2$, in both analysis using numerical and

finite element analysis using ANSYS shows that $\sigma_z$ grows fast near the free edge. Meanwhile, $\sigma_{xz}$ is very close to zero which is same as the theoretical results and the stress $\sigma_{yz}$ approaches to zero gradually in the vicinity of the edge, which is accordance with the boundary condition that $\sigma_{yz}$ is zero at the edge. The nodal solution for the 3D finite element model is shown in Figure 5.10

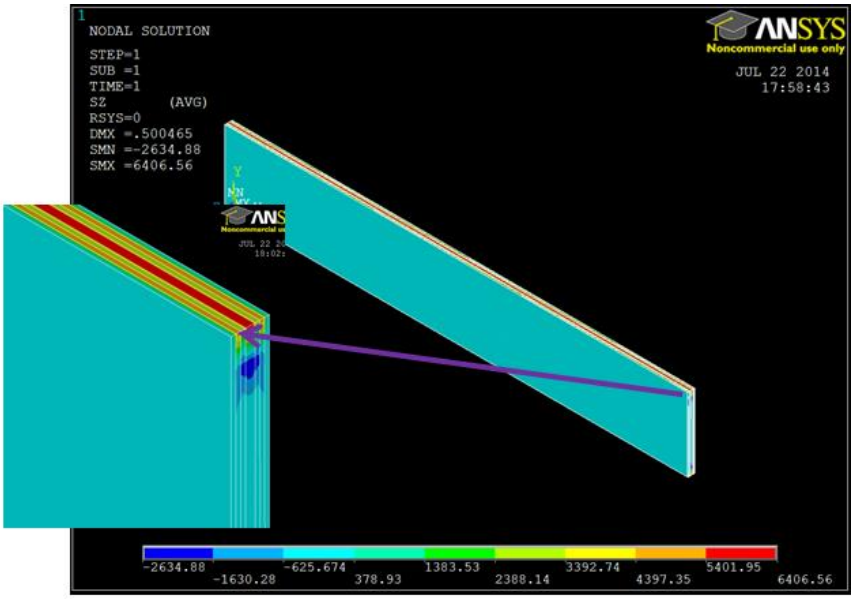


*Figure 5.10.* Nodal solution of the 3D model with Ux =0.5 inches

In summary, 20 noded Solid 186 elements predicted similar distribution of interlaminar stresses in laminated composites as per the closed form solution and hence the SOLID 186 element can be effectively used for 3-D finite element analysis of fiberglass composites. Therefore Solid 186 element was used for the analysis of three point bend test specimens and result obtained by using this element were compared with the experimental results

**5.4 Failure Criteria**

The most general polynomial failure criterion for composite materials is Tensor Polynomial Criterion proposed by Tsai and Wu (Tsai et al., 1971). This criterion can be expressed in tensor notation and is shown in equation (5. 2)

$$F_i\,\sigma_i + F_{ij}\,\sigma_i\,\sigma_j + F_{ijk}\,\sigma_i\,\sigma_j\,\sigma_k \geq 1 \qquad (5.2)$$

where $i,j,k = 1,\dots,6$ for a 3-D case. The parameters $F_i$ , $F_j$ and $F_{ijk}$ are related to the lamina strengths in the principal directions. For practical proposes, and due to the large number of material constants required, the third-order tensor $F_{ijk}$ is usually neglected(Camanho, 2002). Therefore, the general polynomial criterion reduces to a general quadratic expression given in equation (5. 3) as

$$F_i\,\sigma_i + F_{ij}\,\sigma_i\,\sigma_j \geq 1 \qquad (5.\ 3)$$

And when expanded for two dimensional form as in equation (5. 4)

$$F_1\,\sigma_1 + F_2\,\sigma_1\,\sigma_2 + F_{11}\,{\sigma_1}^2 + F_{22}\,{\sigma_2}^2 + +F_{66}\,{\sigma_{12}}^2 + 2F_{12} \geq 1 \qquad (5.4)$$

where $i,j,k = 1,\dots,6$ Considering that the failure of the material is insensitive to a change of sign in shear stresses, all terms containing a shear stress to first power must vanish: $F_4 = F_5 = F_6 = 0$ .Thus the explicit general expression form can be written as in equation (5. 5)

$$F_1\,\sigma_1 + F_2\,\sigma_2 + F_3\,\sigma_3 + 2F_{12}\,\sigma_1\,\sigma_2 + 2F_{13}\,\sigma_1\,\sigma_3 + 2F_{23}\,\sigma_2\,\sigma_3 + F_{11}\,{\sigma_1}^2 + F_{22}\,{\sigma_2}^2 +$$
$$F_{33}\,{\sigma_3}^2 + F_{44}\,{\sigma_4}^2 + F_{55}\,{\sigma_5}^2 + F_{66}\,{\sigma_6}^2 \geq 1 \qquad (5.5)$$

Several other quadratic criteria have been proposed, differing in the way in which the tensor stress components are determined (Camanho, 2002).

Where ${\sigma_1}^u,\ {\sigma_2}^u,\ {\sigma_3}^u$ are normal strength of the lamina in 1, 2, and 3 directions.

${\sigma_{23}}^u,\ {\sigma_{13}}^u,\ {\sigma_{12}}^u$ are shear strength the lamina in 23, 13, and 12 planes.

${\sigma_1}^u,\ {\sigma_2}^u,\ {\sigma_3}^u$: ${\sigma_{1C}}^u,\ {\sigma_{2C}}^u, {\sigma_{3C}}^u\ or\ {\sigma_{1T}}^u,\ {\sigma_{1T}}^u,\ {\sigma_{2T}}^u,\ {\sigma_{3T}}^u$ depending on the sign of $\sigma_1, \sigma_2\ and\ \sigma_3$ respectively.

Where Tsai –Wu factors are as follow in equation (5. 6)

$$F_1 = \frac{1}{{\sigma_{1T}}^u - {\sigma_{1C}}^u}\,,\ F_2 = \frac{1}{{\sigma_{2T}}^u - {\sigma_{2C}}^u}\,,\ F_3 = \frac{1}{{\sigma_{3T}}^u - {\sigma_{3C}}^u}\,,\ F_{12} = \frac{-1}{2\sqrt{{\sigma_{1T}}^u {\sigma_{1C}}^u {\sigma_{2T}}^u {\sigma_{2C}}^u}}\,,$$

$$F_{13} = \frac{-1}{2\sqrt{{\sigma_{1T}}^u {\sigma_{1C}}^u {\sigma_{3T}}^u {\sigma_{3C}}^u}}, F_{23} = \frac{-1}{2\sqrt{{\sigma_{2T}}^u {\sigma_{2C}}^u {\sigma_{3T}}^u {\sigma_{3C}}^u}}, \; F_{11} = \frac{1}{{\sigma_{1T}}^u {\sigma_{1C}}^u}, F_{22} = \frac{1}{{\sigma_{2T}}^u {\sigma_{2C}}^u},$$

$$F_{33} = \frac{1}{{\sigma_{3T}}^u {\sigma_{3C}}^u}, F_{44} = \frac{1}{{\sigma_{23}}^{u^2}}, F_{55} = \frac{1}{{\sigma_{13}}^{u^2}}, F_{66} = \frac{1}{{\sigma_{12}}^{u^2}} . \qquad (5.6)$$

In general, failure criteria can be either interactive is polynomial or non-interactive is independent. An independent criterion gives the mode of failure, for longitudinal or transverse, tensile or compressive or shear mode, and is simple to apply. However, the effect of stress interactions is ignored. The stress interactions are explained by the polynomial failure criteria, and thus the failure mode is disregarded. The laminate may indicate failure using a non-interactive theory. However, the lamina should be checked using the interactive failure. The independent stresses do not initiate failure but their interactions may initiate failure. Thus it is best to check for failure through both independent and non-interactive criteria.

**5.5 Progressive Failure Analysis**

To study the progressive failure in fiberglass composite, Tsai-Wu failure criteria was adopted. Each element was checked for the failure and if no failure was observed then the load was incremented. The properties of the element were degraded using degradation technique which involves reduction of the material properties as shown in Figures 5.11 and 5.12. Thereafter, a check is performed to see whether more elements have failed, if not, a load increment is performed by assigning the reduced element properties based upon Tsai-Wu factor which ranged from 0 to 1. This process was continued till the ultimate failure load occurred.

Total element failure method on reaching the failure, the strength and stiffness of the failed element is totally reduced to zero. This implies that if the element undergoes matrix failure, it will be no longer able to carry load in fiber direction, which, may not be the case and underestimates the laminate strength.

Partial element failure method, the failure mode is taken into account. If the element fails due to fiber failure, the stiffness of the failed element is reduced to zero. However, if it is a matrix controlled failure or shear failure, the longitudinal modulus retains its value but the transverse and shear modulus are set to zero.

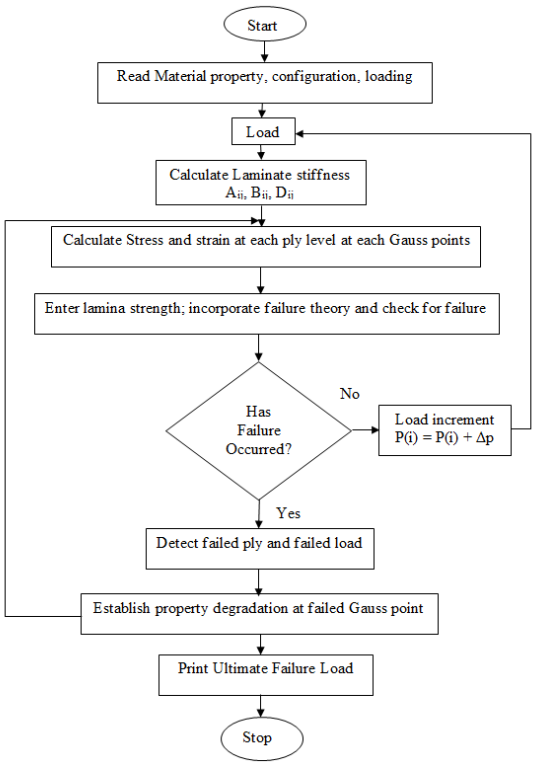


*Figure 5.11.* Flowchart of progressive failure analysis methodology

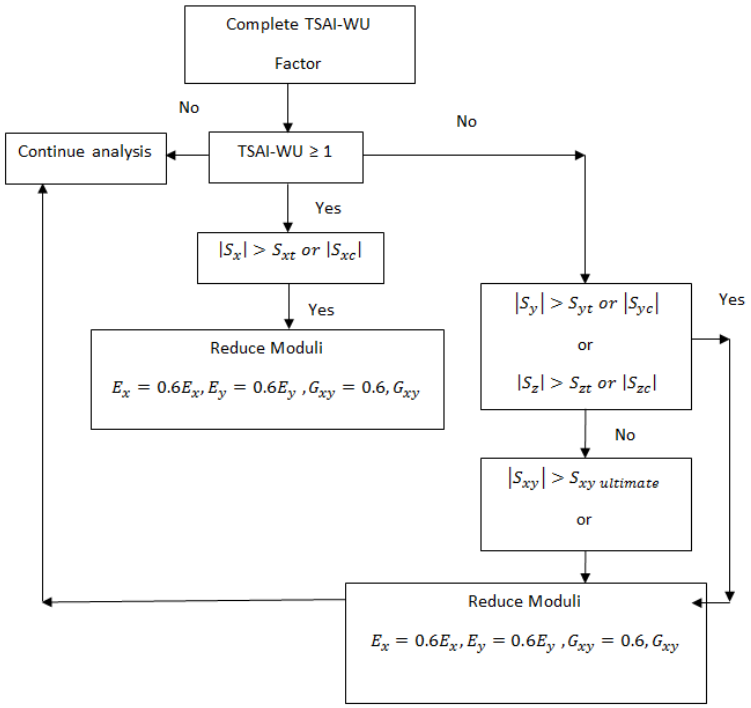


*Figure 5.12.* Degradation of stiffness of the material using Tsai-Wu factor

**5.6 Three Dimensional Finite Elements Model for MSBS Specimen**

In the present work, all models were developed using ANSYS. A modified short beam specimen for three points bend test was created as per ADTM D2344 standard with dimensions: length 1.5 inches width 0.25 inches, and thickness 0.175395 inches and 0.16346 inches for 12GF+11RF and ENFs hybrid composite and 12GF+11RF composite respectively. Full model for three point bend tests with TEOS ENFs non-woven mat in the epoxy resin film and model with boundary conditions are shown in Figure 5.13 and 5.14 respectively and is in Table 5.2.

*Table 5.2* Ply-wise thickness in composites with and without ENFs

| 12GF+11RF and ENFs | | | 12GF+11RF | | |
|---|---|---|---|---|---|
| Ply # | Thickness(in) | Ply at height(in) | Ply # | Thickness(in) | Ply at height(in) |
| 1 | 0.00627 | 0.00627 | 1 | 0.00627 | 0.00627 |
| 2 | 0.009105 | 0.015375 | 2 | 0.00802 | 0.01429 |
| 3 | 0.00627 | 0.021645 | 3 | 0.00627 | 0.02056 |
| 4 | 0.009105 | 0.03075 | 4 | 0.00802 | 0.02858 |
| 5 | 0.00627 | 0.03702 | 5 | 0.00627 | 0.03485 |
| 6 | 0.009105 | 0.046125 | 6 | 0.00802 | 0.04287 |
| 7 | 0.00627 | 0.052395 | 7 | 0.00627 | 0.04914 |
| 8 | 0.009105 | 0.0615 | 8 | 0.00802 | 0.05716 |
| 9 | 0.00627 | 0.06777 | 9 | 0.00627 | 0.06343 |
| 10 | 0.009105 | 0.076875 | 10 | 0.00802 | 0.07145 |
| 11 | 0.00627 | 0.083145 | 11 | 0.00627 | 0.07772 |
| 12 | 0.009105 | 0.09225 | 12 | 0.00802 | 0.08574 |
| 13 | 0.00627 | 0.09852 | 13 | 0.00627 | 0.09201 |
| 14 | 0.009105 | 0.107625 | 14 | 0.00802 | 0.10003 |
| 15 | 0.00627 | 0.113895 | 15 | 0.00627 | 0.1063 |
| 16 | 0.009105 | 0.123 | 16 | 0.00802 | 0.11432 |
| 17 | 0.00627 | 0.12927 | 17 | 0.00627 | 0.12059 |
| 18 | 0.009105 | 0.138375 | 18 | 0.00802 | 0.12861 |

Table 5.2 Ply-wise thickness in composites with and without ENFs *Cont.*

| 12GF+11RF and ENFs | | | 12GF+11RF | | |
|---|---|---|---|---|---|
| Ply # | Thickness(in) | Ply at height(in) | Ply # | Thickness(in) | Ply at height(in) |
| 19 | 0.00627 | 0.144645 | 19 | 0.00627 | 0.13488 |
| 20 | 0.009105 | 0.15375 | 20 | 0.00802 | 0.1429 |
| 21 | 0.00627 | 0.16002 | 21 | 0.00627 | 0.14917 |
| 22 | 0.009105 | 0.169125 | 22 | 0.00802 | 0.15719 |
| 23 | 0.00627 | 0.175395 | 23 | 0.00627 | 0.16346 |

The boundary conditions for 3D Finite element model for 12GF+11RF and ENFs hybrid composite are as follows.

a) At x = 0.25 inches and x = 1.25inches, z = 0 along y- axis on bottom face nodes applied with z-displacement, $U_z = 0$.

b) At y = 0.125 inches along z-axis through thickness line nodes are applied with y-displacement, $U_y = 0$.

c) At z = 0.175395 inches on top surface elements x = 0.7084 to 0.7916 applied with stepwise pressure was applied.

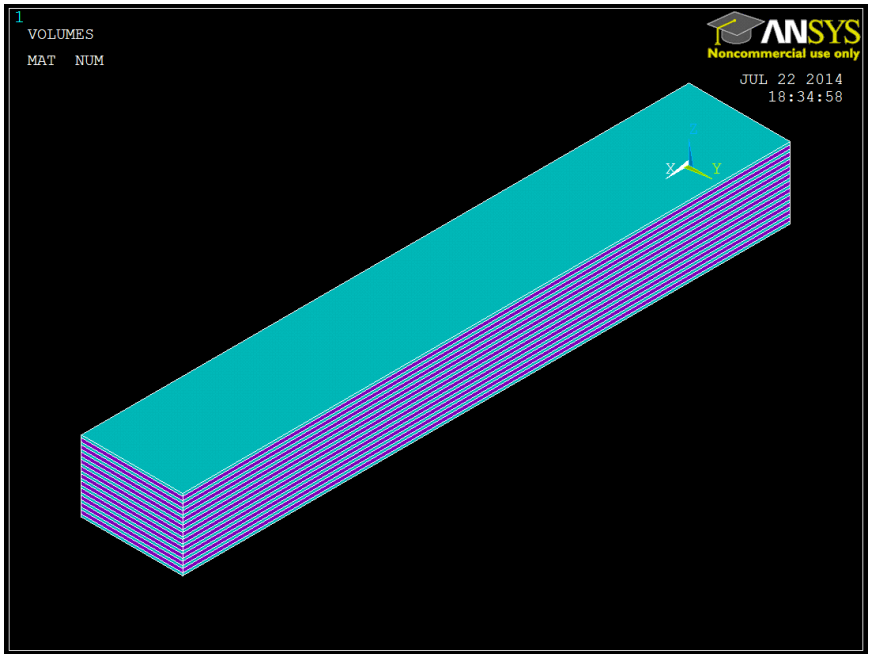


*Figure 5.13.* 3D Finite element Model for 12GF+11RF and ENFs hybrid composite

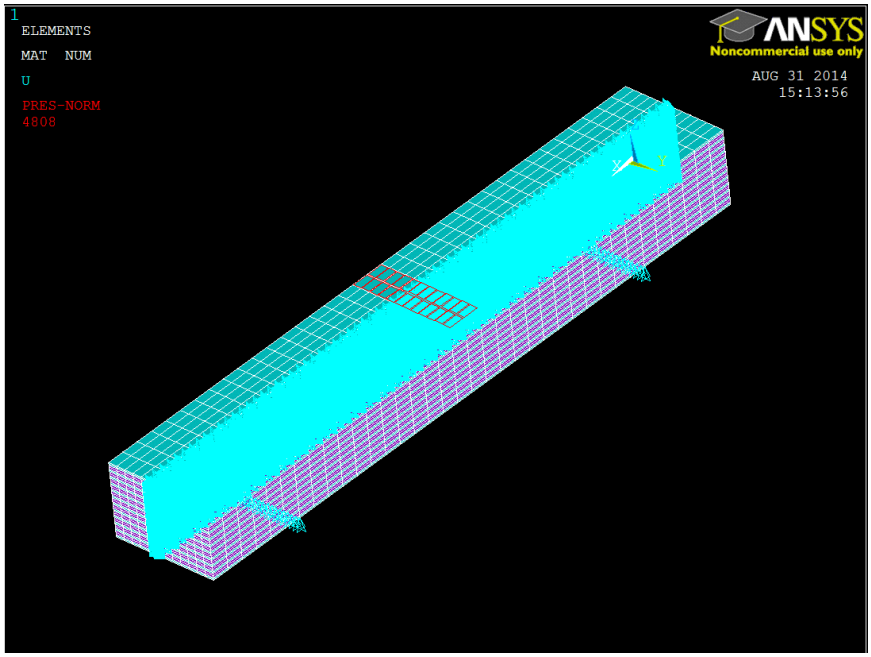


*Figure 5.14.* 3D Finite element meshed model for 12GF+11RF and ENFs hybrid composite with boundary conditions

## 5.7 Progressive Failure in Three Point Bending Test Specimen

In order to study the progressive failure of the MSBS fiberglass composite with and without TEOS ENFs non-woven mat, transverse loads was applied in step-wise as shown in Table 6.3 to analyze the complete failure of elements in each case. The area of the two rows of the elements at the middle line of the specimen was calculated and was 0.02079 $in^2$. The pressure was applied on the top surface of the specimen and the corresponding stepwise pressure is shown in Table 5.3.

*Table 5.3* Stepwise Compressive load applied to 12GF-11RF and 12GF-11RF and ENFs composites

| Step | Force $F_z$ (lb) | Pressure(psi) |
|---|---|---|
| 1 | 100 | 4808 |
| 2 | 125 | 6012 |
| 3 | 150 | 7213 |
| 4 | 200 | 9617 |
| 5 | 250 | 12021 |
| 6 | 300 | 14426 |
| 7 | 325 | 15628 |

### 5.7.1 Failure criteria for elements

The failure of the elements both in 12GF-11RF and 12-GF-11RF and ENFs composites were decided by applying stepwise $P_z$ pressure as shown in Table 5.3, on the top middle nodes of the MSBS specimen model. The model was run with applied boundary conditions and plotted the element solution using the plot contours. When the stresses in elements $\sigma_{xx}, \sigma_{zz}, \tau_{yz}, and\ \tau_{xz},$

exceed the material ultimate strengths $S_{xx}$, $S_{zz}$ ,$S_{xz}$, and $S_{yz}$, in material MAT1 and material MAT2, then the elements are failed either by normal stresses or shear stresses.

#### *5.7.1.1 Progressive failure of elements in 12GF-11RF composite*

In order to perform the progressive failure of MSBS specimens a 3-D finite element model of the 12 GF-11RF composite was applied with incremental load and the corresponding stresses induced in the failed elements were captured. Using Tai-Wu failure criteria, the Tsai-Wu factor was calculated for each of the failed element in the each material.

In the first case, pressure in the z-direction $P_z$ = 4808 lb/in$^2$ were applied and the elemental solution was obtained. It was found that no elements were failed in both MAT1 and MAT2. When $P_z$ = 6012 lb/in$^2$ was applied the element on the top ply of the GF were failed due to the stresses increased in $S_{xc}$.

Using Tsai-Wu failure criteria, failed elements properties were reduced and the model was run with modified material properties and incremental transverse load and the corresponding deflection and the strain energy of failed element and the total energy of the system was calculated. With applying the pressure steps as shown in Table 5.3 the corresponding stresses, deflection and strain energy(SE) was noted Table 5.4.

*Table 5.4* Analysis of stresses in the 12GF-11RF models from the elemental solution

| Pressure (psi) | MAT | $S_{xx}$ (ksi) | $S_{zz}$ (ksi) | $S_{zz}$ (ksi) | Deflection Uz (in) | SE (lb-in) |
|---|---|---|---|---|---|---|
| 4808 | 1 | | - | - | 0.01126 | 0.5528 |
| | 2 | | - | - | | |
| 6012 | 1 | Sxc>Sx | - | - | 0.01408 | 0.8643 |
| | 2 | - | - | - | | |
| 7213 | 1 | Sxc>Sx | - | - | 0.01714 | 1.25 |
| | 2 | Sxc>Sx | Szc>Sz | - | | |
| 9617 | 1 | Sxc>Sx | - | - | 0.02291 | 2.2513 |
| | 2 | - | Szc>Sz | Sxzc ,Sxt>Sxz | | |
| 12021 | 1 | Sxc>Sx | - | Sxzc , Sxt>Sxz | 0.02815 | 3.9021 |
| | 2 | Sxc>Sx | Szc>Sz | Sxzc, Sxt>Sxz | | |
| 14426 | 1 | Sxc>Sx | - | Sxzc , Sxt>Sxz | 0.03378 | 6.277 |
| | 2 | Sxc>Sx | Szc>Sz | Sxzc , Sxt>Sxz | | |
| 15628 | 1 | Sxc>Sx | - | Sxzc, Sxt>Sxz | 0.0366 | 31.3044 |
| | 2 | Sxc,Sxt>Sx | Szc>Sz | Sxzc, Sxt>Sxz | | |

At each pressure step, the failed elements were captured and are shown in Figures 5.15a-e. The strain energy of the failed elements calculated was used to compare finite element analysis results with the area under load-displacement curve of experimental results. The stresses in the

elements exceeded the ultimate strength of that material are shown with red color and the pink color as shown in Figure 5.15f. The pink color indicate the failed element in the top ply of the GF, however in the next incremental load step, the elements were crushing before the load transfer to the bottom elements, therefore top ply element under the pressure were assigned with properties of the MAT1 but defined with another material. The failure occurred basically due to exceed in stresses in x-x, and z-z directions, also the shear stresses exceeded in x-z direction. The failure of the fiberglass composite occurred mainly because of exceed in inter-laminar stresses. The stresses induced in the x-x direction after failure of elements are shown in Figure 5.16.

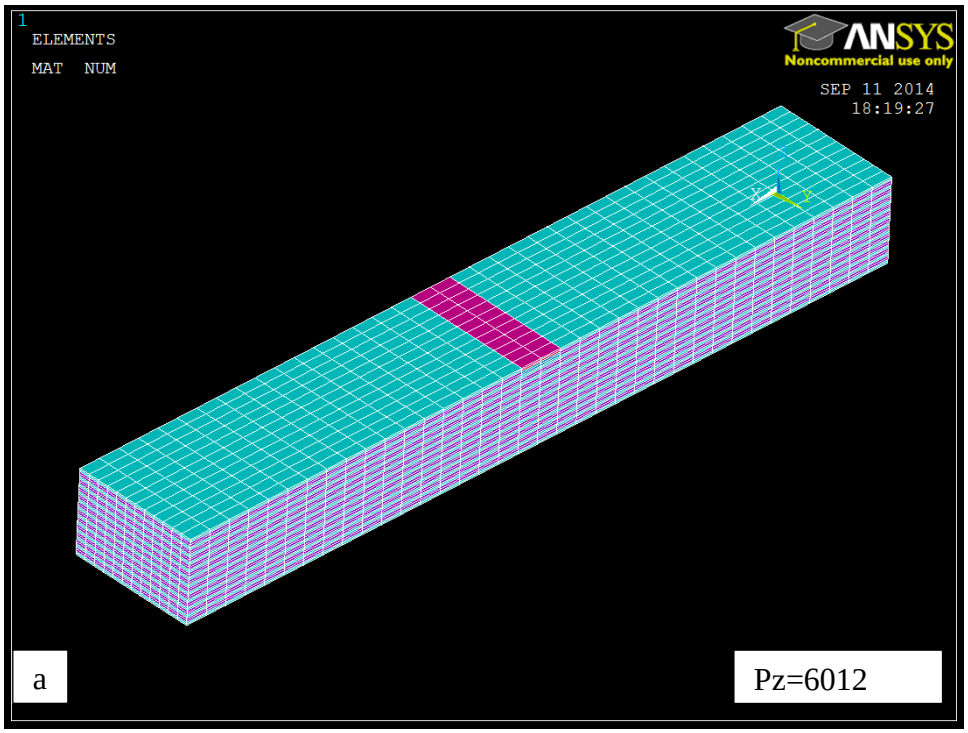

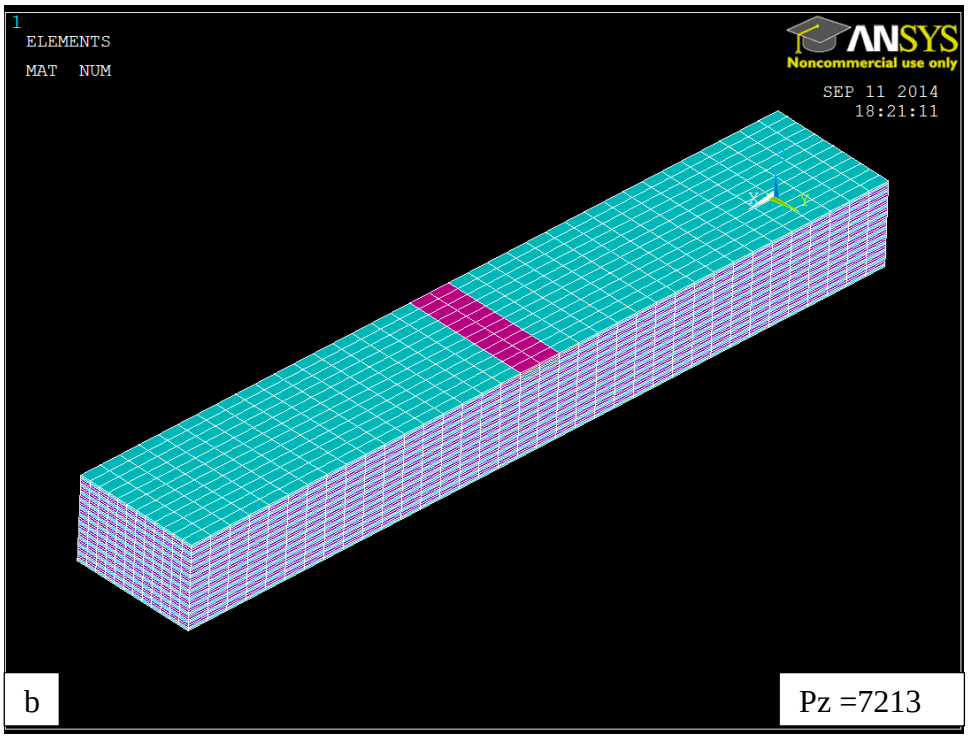
1
ELEMENTS
MAT NUM
ANSYS
Noncommercial use only
SEP 11 2014
18:21:11
b
Pz =7213

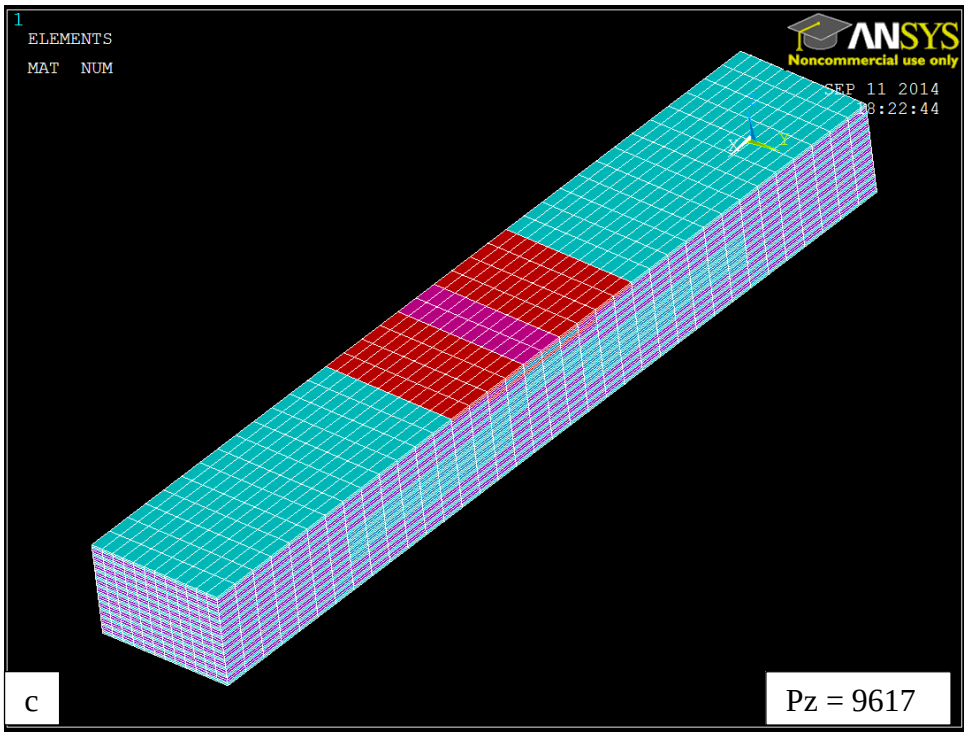
1
ELEMENTS
MAT NUM
ANSYS
Noncommercial use only
SEP 11 2014
18:22:44
c
Pz = 9617

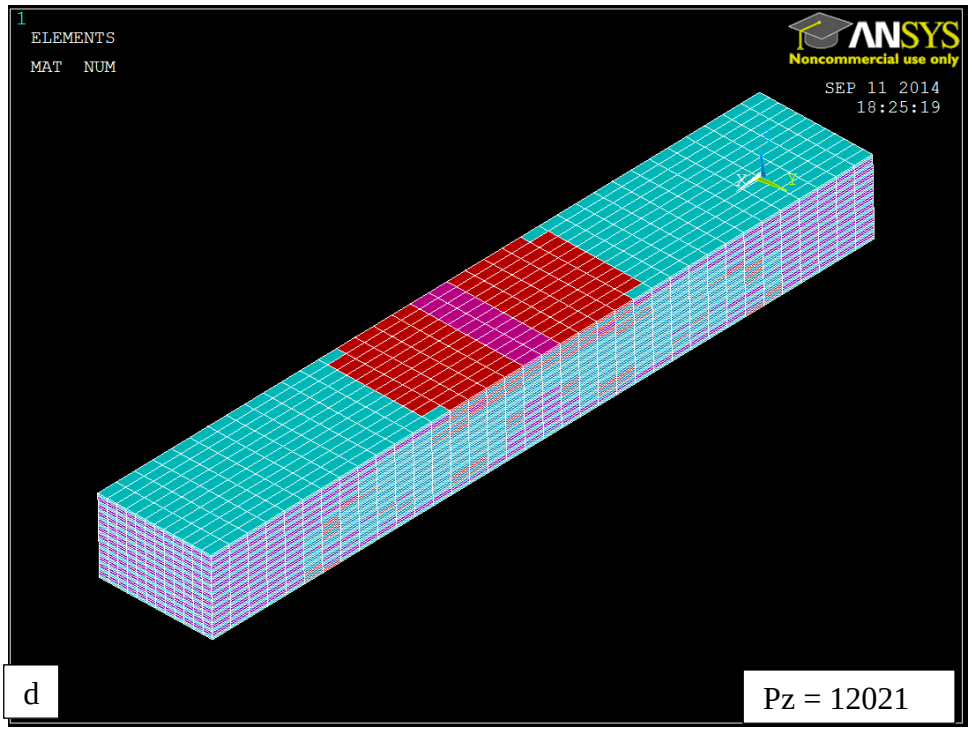
1
ELEMENTS
MAT NUM
ANSYS
Noncommercial use only
SEP 11 2014
18:25:19
d
Pz = 12021

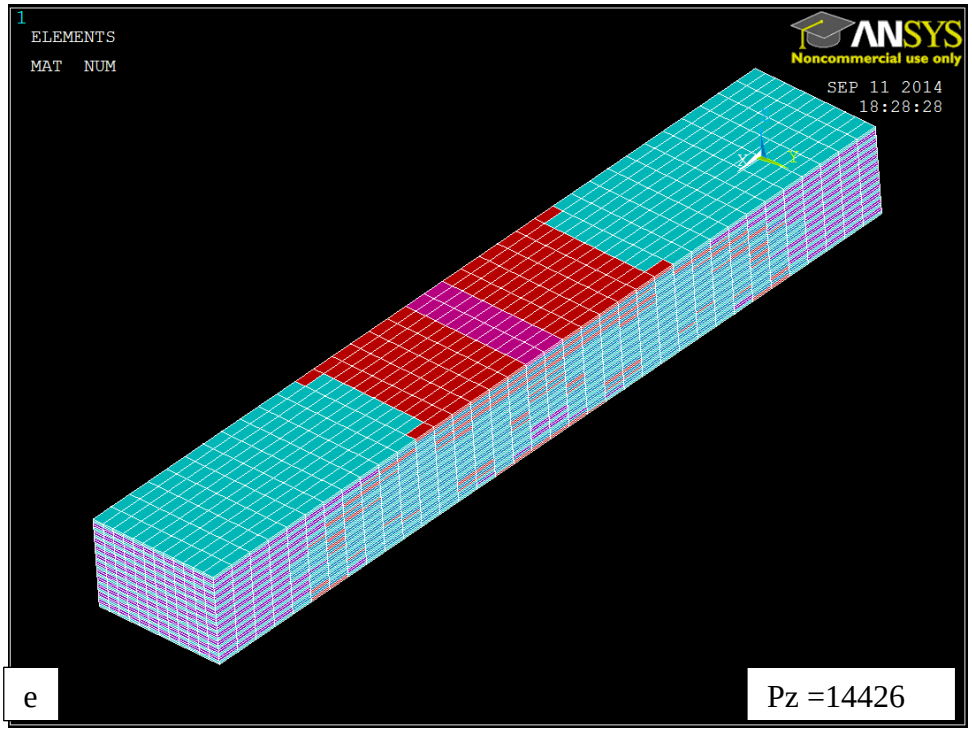
1
ELEMENTS
MAT NUM
ANSYS
Noncommercial use only
SEP 11 2014
18:28:28
e
Pz =14426

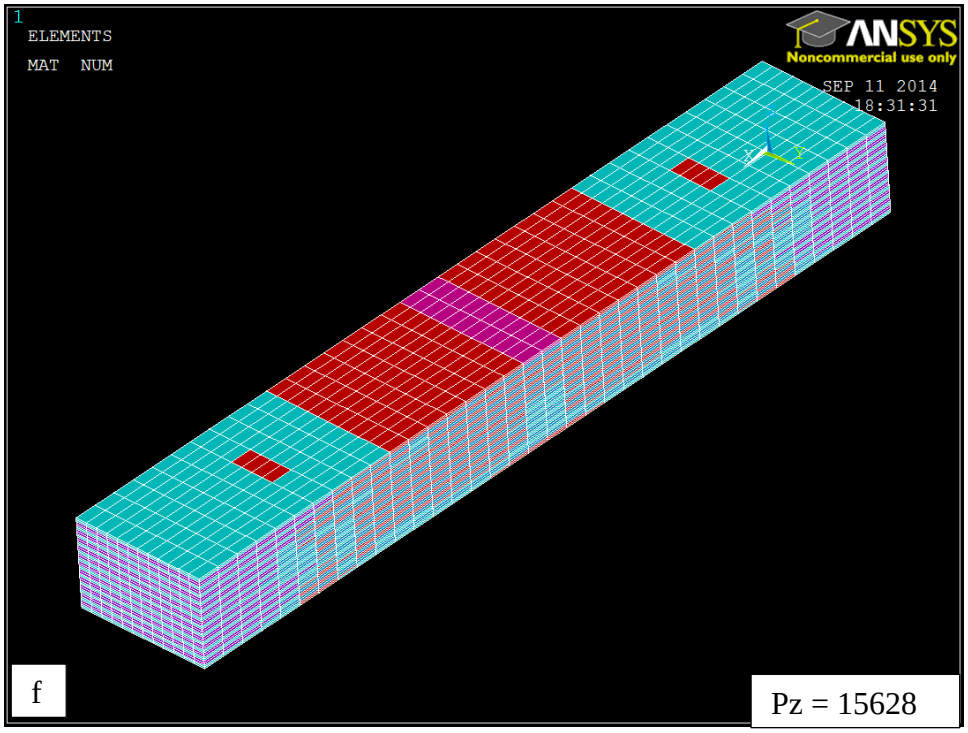


*Figure 5.15.* Progressive failed elements in the model for 12GF-11RF and ENFs MSBS model for Pressure in z-direction a) 6012psi, b) 7213psi, c) 9617psi, d) 12021psi, e) 14426psi, and f)15628psi

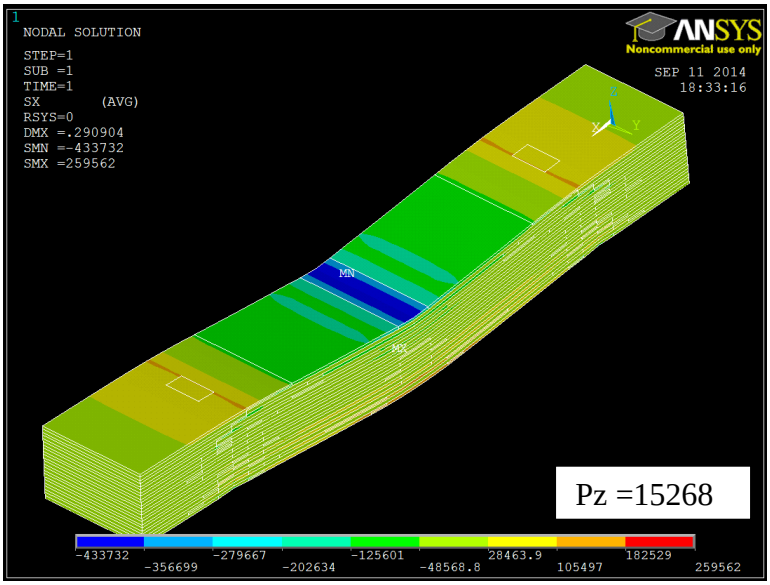


*Figure 5.16.* Stresses induced in x-x direction in progressive failure of 12GF-11RF MSBS composite

#### *5.7.1.2 Progressive failure of elements in 12GF-11RF and ENFs composite*

In order to perform the progressive failure of MSBS specimens a 3-D finite element model of the 12 GF-11RF-11ENFs composite was applied with incremental load as per the Table 5.3 and the corresponding stresses induced in the failed elements were captured. Using Tai-Wu failure criteria, the Tsai-Wu factor was calculated for each of the failed element in the each material. Figure 5.17a-f shows the failure of the element with incremental load was applied to perform the progressive failure of the composite using elemental solution method. Failure occurred due exceed in the stresses are noted in the Table 5.5

*Table 5.5* Analysis of stress in the 12GF-11RF and ENFs models from the elemental solution

| Pressure (psi) | MAT | $S_{xx}$ (ksi) | $S_{zz}$ (ksi) | $S_{zz}$ (ksi) | Deflection Uz (in) | SE (lb-in) |
|---|---|---|---|---|---|---|
| 4808 | 1 | - | - | - | 0.0098 | 0.4807 |
| | 2 | - | - | - | | |
| 6012 | 1 | Sxc>Sx | - | - | 0.01225 | 0.7515 |
| | 2 | - | - | - | | |
| 7213 | 1 | Sxc>Sx | - | - | 0.01532 | 1.1764 |
| | 2 | Sxc>Sx | Szc>Sz | - | | |
| 9617 | 1 | Sxc>Sx | - | - | 0.02035 | 1.9907 |
| | 2 | - | Szc>Sz | Sxzc, Sxt>Sxz | | |
| 12021 | 1 | Sxc>Sx | Szc>Sz | Sxzc, Sxt>Sxz | 0.02876 | 3.5277 |
| | 2 | Sxc>Sx | - | Sxzc, Sxt>Sxz | | |

Table 5.5 Analysis of stress in the 12GF-11RF and ENFs models from the elemental solution *Cont.*

| Pressure (psi) | MAT | $S_{xx}$ (ksi) | $S_{zz}$ (ksi) | $S_{zz}$ (ksi) | Deflection Uz (in) | SE (lb-in) |
|---|---|---|---|---|---|---|
| 14426 | 1 | Sxc>Sx | Szc>Sz | Sxzc, Sxt>Sxz | 0.03707 | 4.9457 |
| | 2 | Sxc>Sx | Szc>Sz | Sxzc, Sxt>Sxz | | |
| 15628 | 1 | Sxc>Sx | Szc>Sz | Sxzc, Sxt>Sxz | 0.05726 | 9.125 |
| | 2 | Sxc, Sxt>Sx | Szc>Sz | Sxzc, Sxt>Sxz | | |

The failed elements were captured at each pressure step ranging from 4808 psi to 14426 psi and are shown in Figures 6.17 a-e.

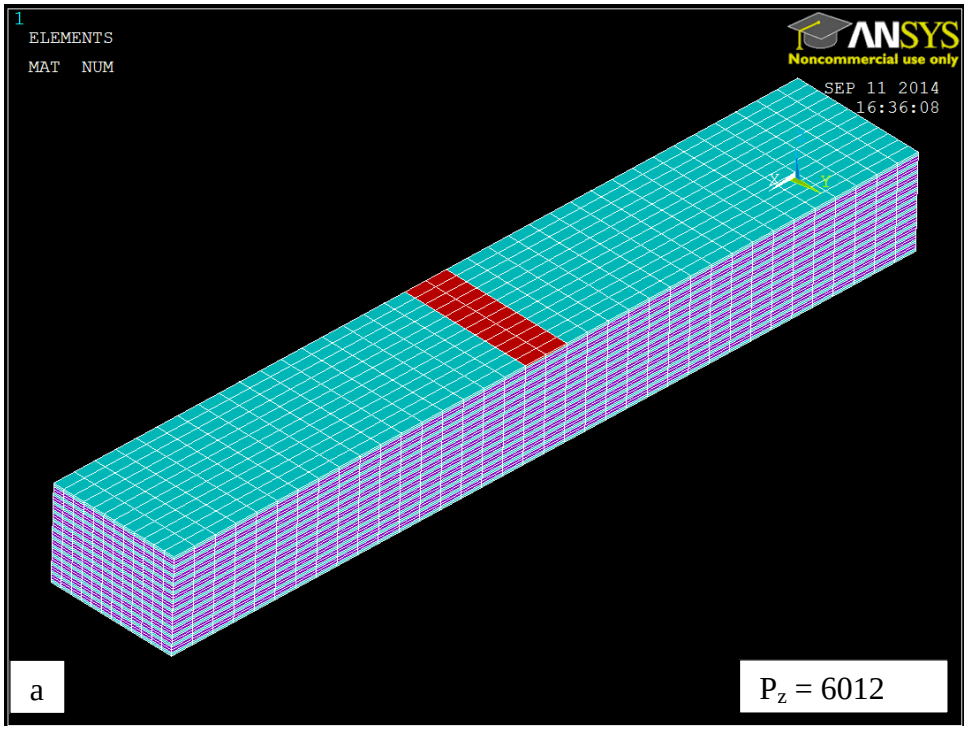
1
ELEMENTS
MAT NUM
ANSYS
Noncommercial use only
SEP 11 2014
16:36:08
a
$P_z$ = 6012

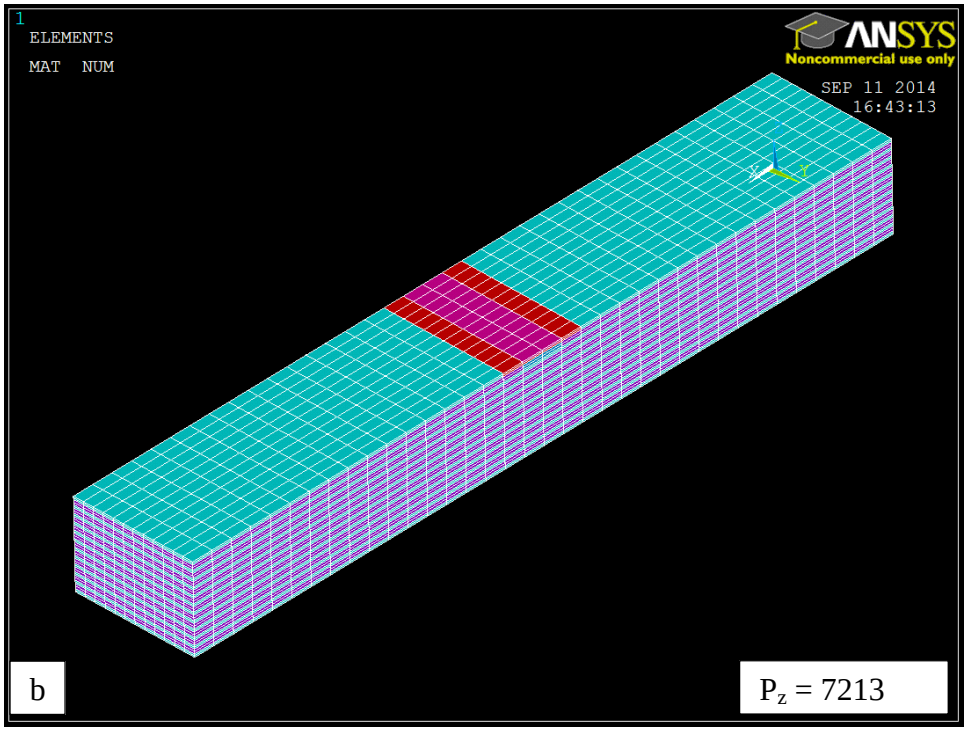
1
ELEMENTS
MAT NUM
ANSYS
Noncommercial use only
SEP 11 2014
16:43:13
b
$P_z$ = 7213

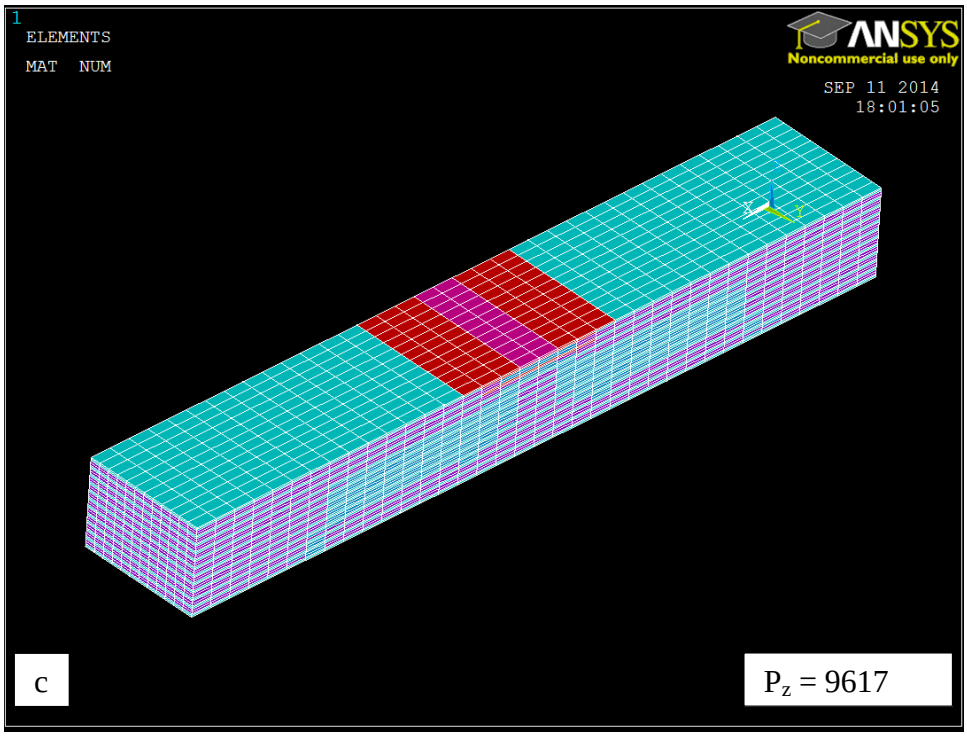
1
ELEMENTS
MAT NUM
ANSYS
Noncommercial use only
SEP 11 2014
18:01:05
c
$P_z$ = 9617

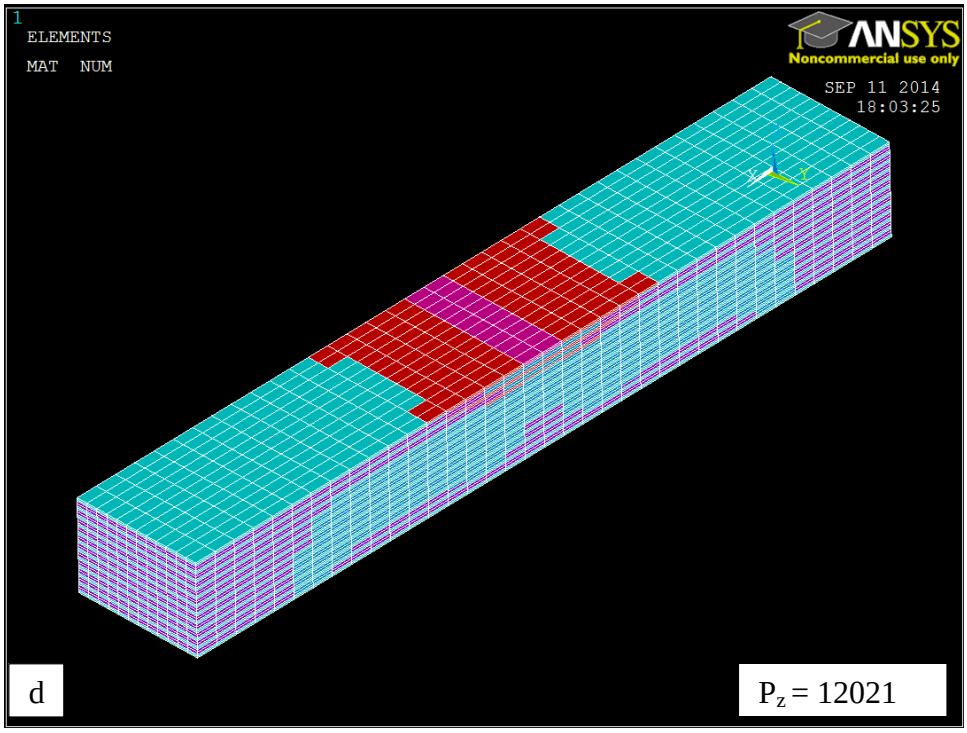
1
ELEMENTS
MAT NUM
ANSYS
Noncommercial use only
SEP 11 2014
18:03:25
d
$P_z$ = 12021

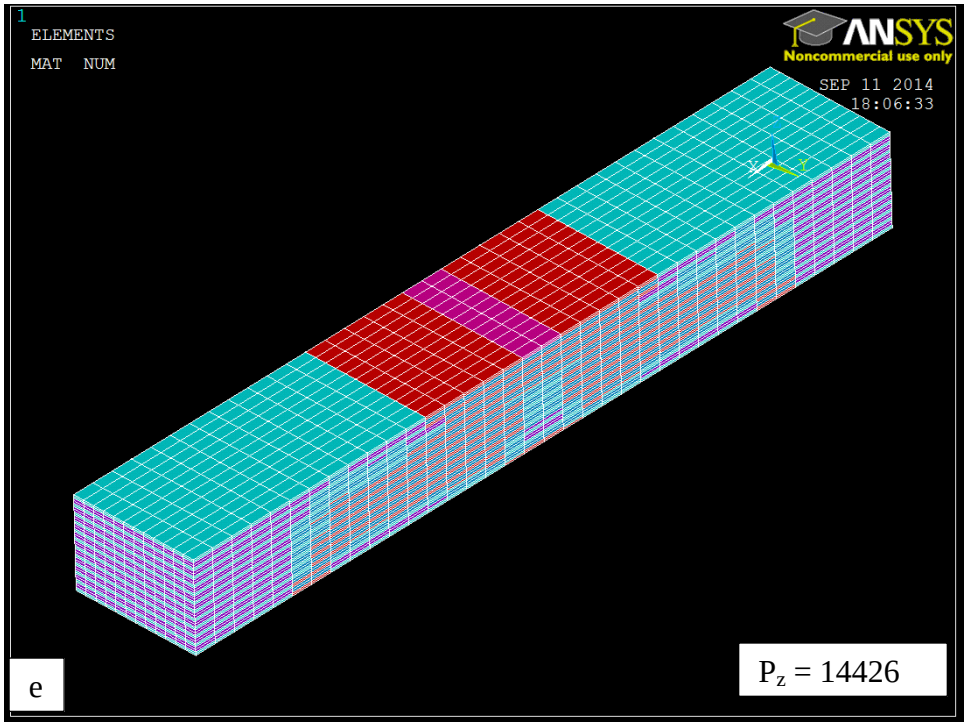


*Figure 5.17.* Progressive failed elements in the model for 12GF-11RF and ENFs MSBS model for Pressure in z direction a) 6012 psi, b) 7213 psi, c) 9617 psi, d) 12021 psi, and e) 14426 psi

The failed elements in the progressive failure of 12GF-11RFand ENFs composite model with applying incremental load of 6012 psi to 14426 psi. The failure stresses in the final model is shown in Figure 6.18, which shows that more than 90% of elements are failed. Top half of the plies in both MAT1 and MAT2 are failed due to the compression loading and bottom half of the plies are failed by tension loading. Very few of fiberglass plies and only one resin with ENFs ply were not failed. The failures of elements are noted from the Table 5.5.

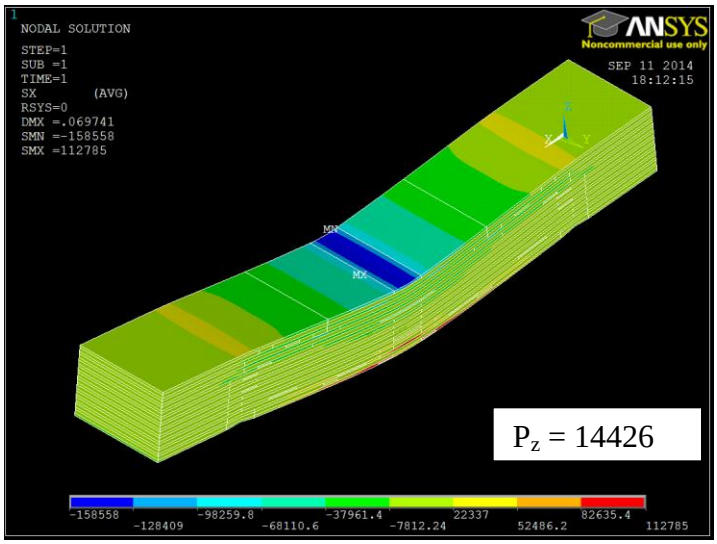


*Figure 5.18.* Stresses in x-x plane with progressive failure of 12GF-11RF and ENFs MSBS composite

### *5.7.1.3 Progressive failure of elements in 12GF-11RF and ENFs composite in [0/90] and [0/60]*

The progressive failure of the $[0/90/90/0/0/90]_s$ and $[0/60/-60/-60/60/0]_s$ stacked laminated composite with and without TEOS ENFs were performed using Tsai-Wu failure criteria and maximum strength-criteria. For the progressive failure analysis five load steps were chosen. This range was determined by using the maximum value of the load taken by the specimens during the MSBS testing. For [0/90] stacking sequence, the load steps were 100,150, 200, and 260 lbs and for the [0/60] stacking sequence the load steps were 75, 100, 125,150, and 140 lbs. The results of the progressive failure analysis are shown in Figures 6.19 and 6.20.The failed element s are shown with colors pink, blue and green. The pink color indicate the failed element in the top ply of the GF, in order to  transfer load transfer to the bottom element in next incremental load step, which crush the elements, therefore top ply element under the pressure were assigned with properties of the MAT1 but defined with another material.

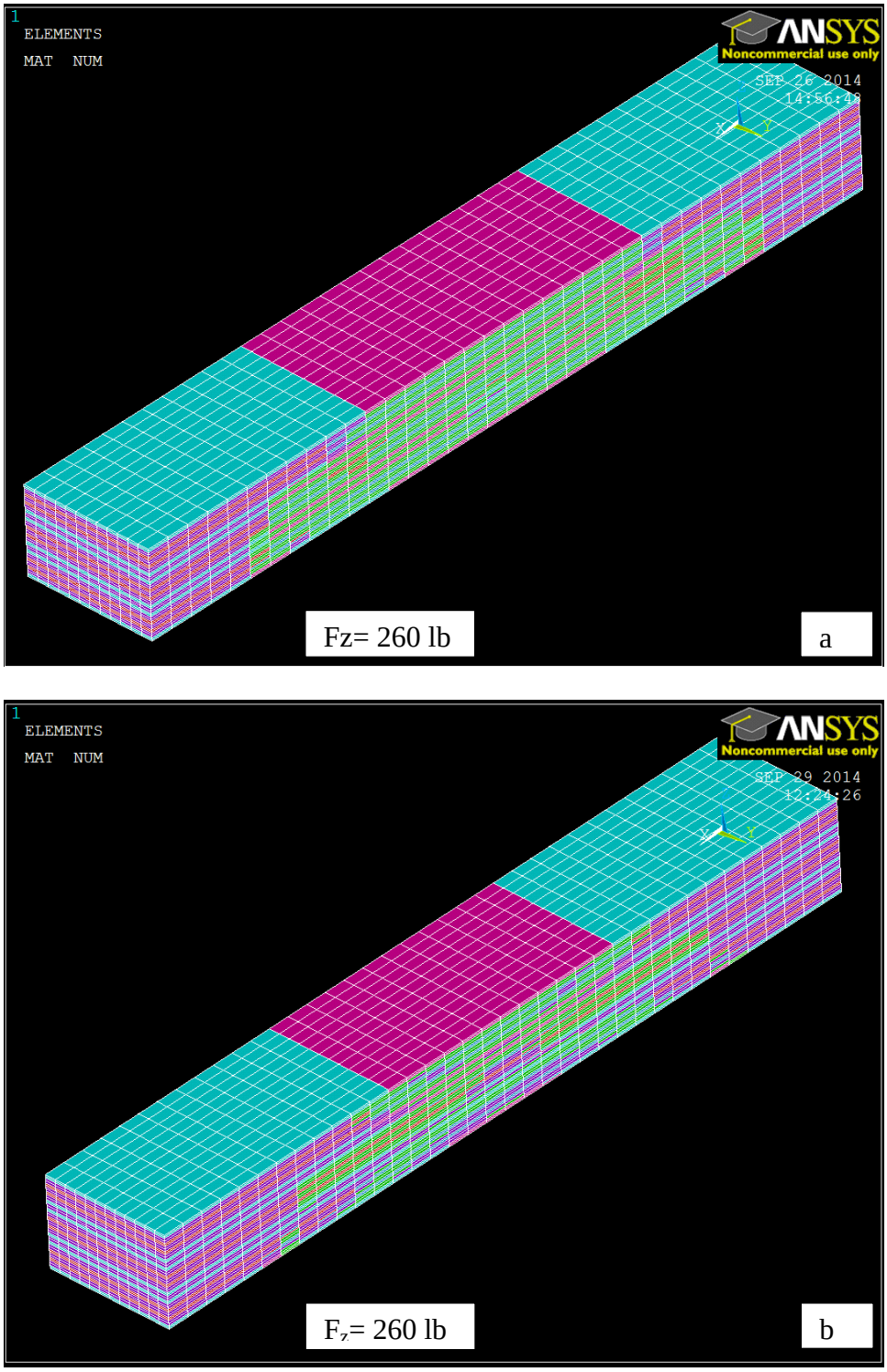


*Figure 5.19.* Progressive failure of laminated composite with $[0/90/90/0/0/90]_s$ stacking sequence a) GF-RF and b) GF-RF and ENFs

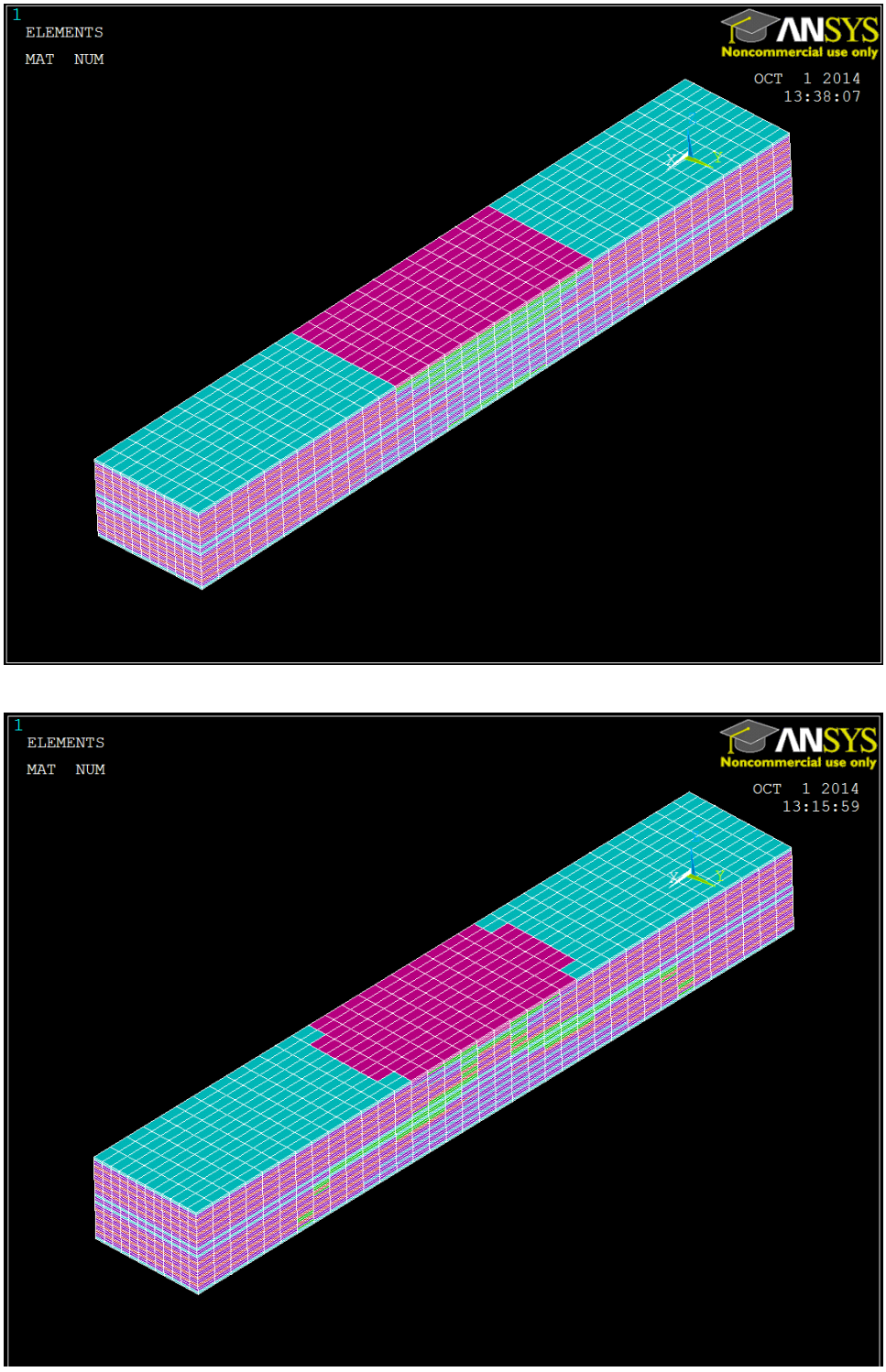


*Figure 5.20.* Progressive failure of laminated composite with $[0/60/-60/-60/60/0]_s$ stacking sequence a) GF-RF and b) GF-RF and ENFs

## 5.8 Calculation of Strain Energy Released During the Progressive Failure of MSBS Specimens

In order to calculate strain energy released due to progressive failure in fiberglass laminates, following procedure was adopted:

- Apply transverse load to the specimen
- Determine the strain energy of the elements due to loading
- Apply failure criteria
- Reduce the properties of failed elements
- Determine the new strain energy of the elements
- Determine the difference between the energies
- Continue the procedure by incrementing load

Following the above procedure, the total strain energy released and the strain energy of the failed elements for each load step was noted and is given in Tables 5.5 and 5.6.

*Table 5.6* Step-wise strain energy released in the bending deformation of the MSBS coupon from finite element analysis

| Z-Pressure (Psi) | Strain Energy of failed elements (lb-in) | |
|---|---|---|
| | 12GF-11RF composite | 12GF-11RF and ENFs composite |
| 4808 | 0 | 0 |
| 6012 | 0.0395 | 0.0181 |
| 7213 | 0.1871 | 0.0853 |
| 9613 | 0.8514 | 0.5935 |
| 12021 | 4.3019 | 3.3650 |
| 14426 | 16.31 | 10.74 |

The strain energy of both with and without TEOS ENFs non-woven mat in the hybrid composites was compared. The result of finite element analysis for both composites shows that the strain energy released in the hybrid composite with ENFs is increased by 38.36% with sandwiching the TESO ENFs.

### 5.8.1 Progressive failure of laminated fiberglass composite in $[0/0/0/0/0/0]_s$

Comparison of experimental and finite element load-displacement behavior of the fiberglass specimens without nanofibers and with nanofibers is shown in Figures 5.21 and 5.22. The load displacement curves show different behavior, the specimens with interleaved nanofibers mats show significantly higher area under load-displacement curve as compared to the specimens without presence of nanofibers mats. Overall both types of specimens indicated good agreement between experimental and finite element results.

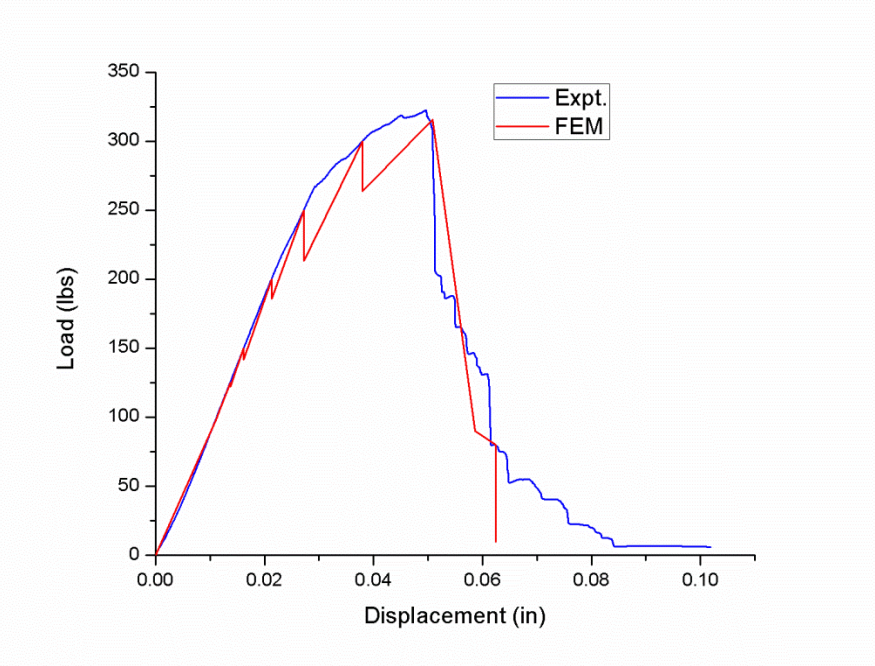


*Figure 5.21.* Comparison of experimental and FEM results12GF-11RFcomposites in three point bend test

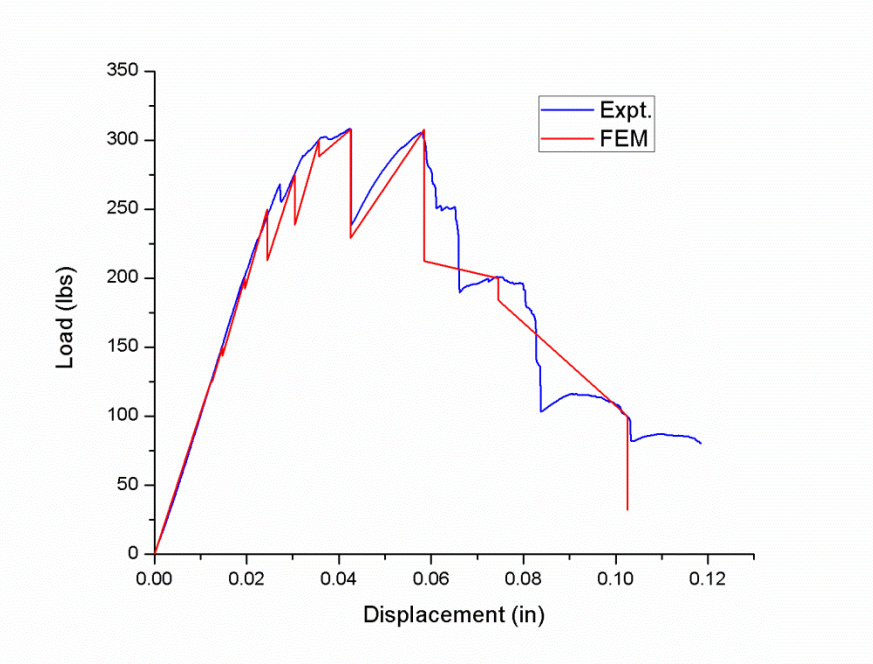


*Figure 5.22.* Comparison of experimental and FEM results GF-ENFs composites in three point bend test

Figure 5.23 presents load displacement behavior comparison of fiberglass laminates with and without interleaved nanofibers mats. The failure mechanisms of fiberglass composites with nanofibers are significantly different than the fiberglass laminates without nanofibers. The total energy absorbed (area under the curve) was found to be 51% higher in the case of fiberglass specimens with nanofibers mats.

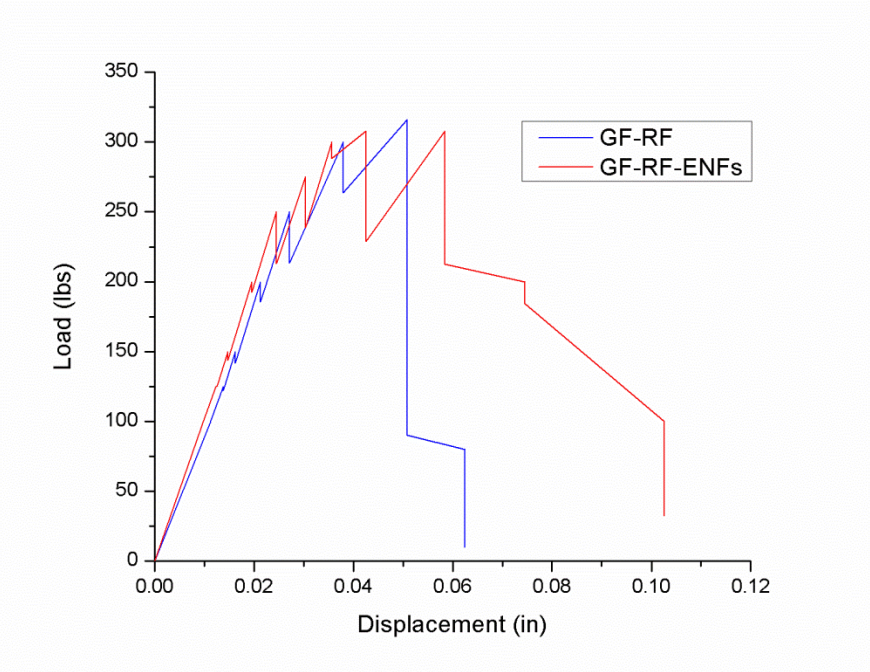


*Figure 5.23.* Comparison of FEM results for GF and GF-ENFs composites in three point bend test

### 5.8.2 Progressive failure of laminated composite in $[0/90/90/0/0/90]_s$ and $[0/60/-60/-60/60/0]_s$ stacking

The progressive failure analysis using 3-D finite element method were performed for the $[0/90/90/0/0/90]_s$ and $[0/60/-60/-60/60/0]_s$ stacking sequences with and without ENFs and the behaviors of the specimens were compared with experimental results and are shown in Figures 5.25 and 5.26 and Figures 5.27 and 5.28 respectively. Both behaviors were well agreed with experimental results.

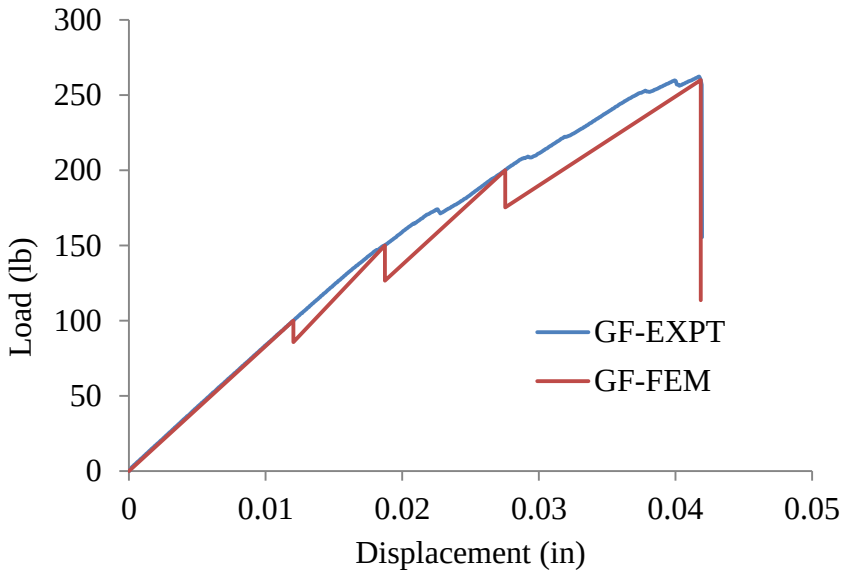


*Figure 5.24.* Comparison of experimental and FEM results of $[0/90/90/0/0/90]_s$ 12GF-11RFcomposites in three point bend test

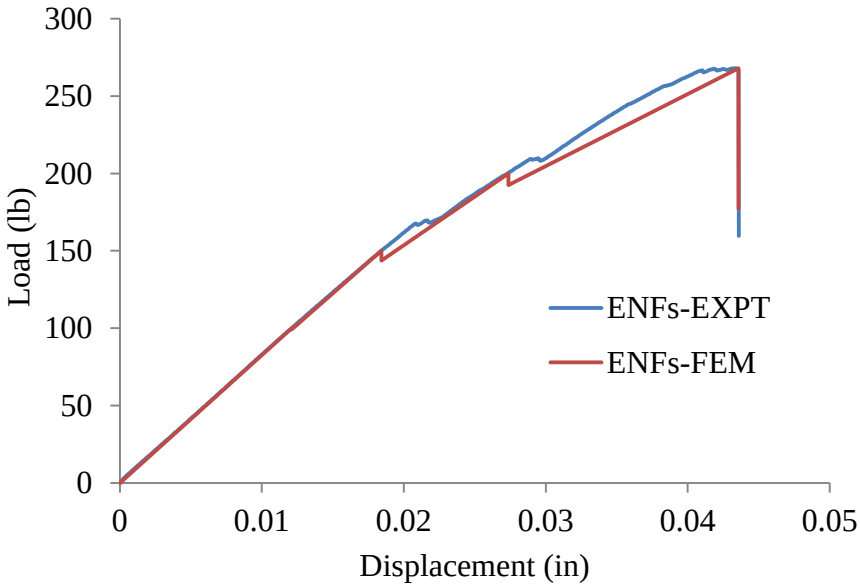


*Figure 5.25.* Comparison of experimental and FEM results of $[0/90/90/0/0/90]_s$ 12GF-11RF and ENFs composites in three point bend test

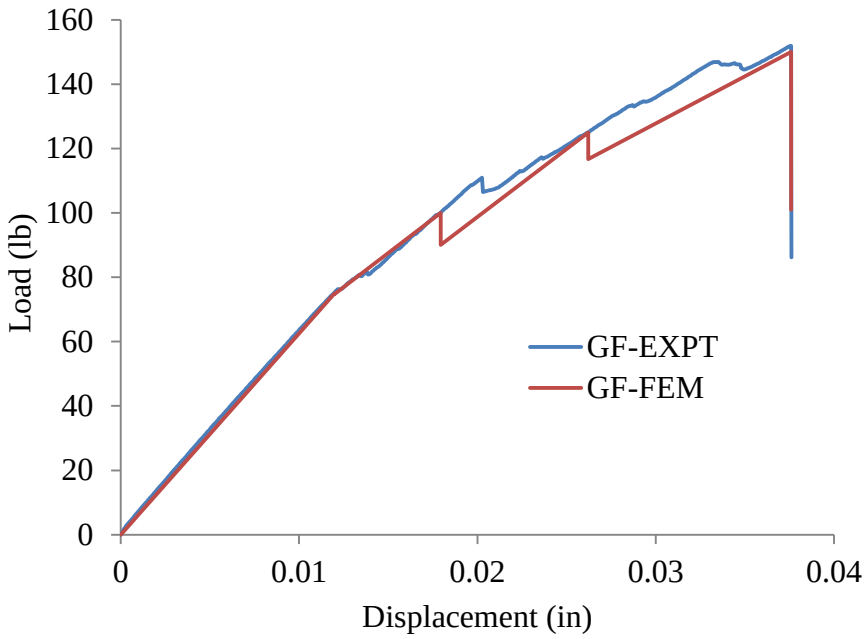


*Figure 5.26.* Comparison of experimental and FEM results of $[0/60/-60/-60/60/0]_s$ 12GF-11RFcomposites in three point bend test

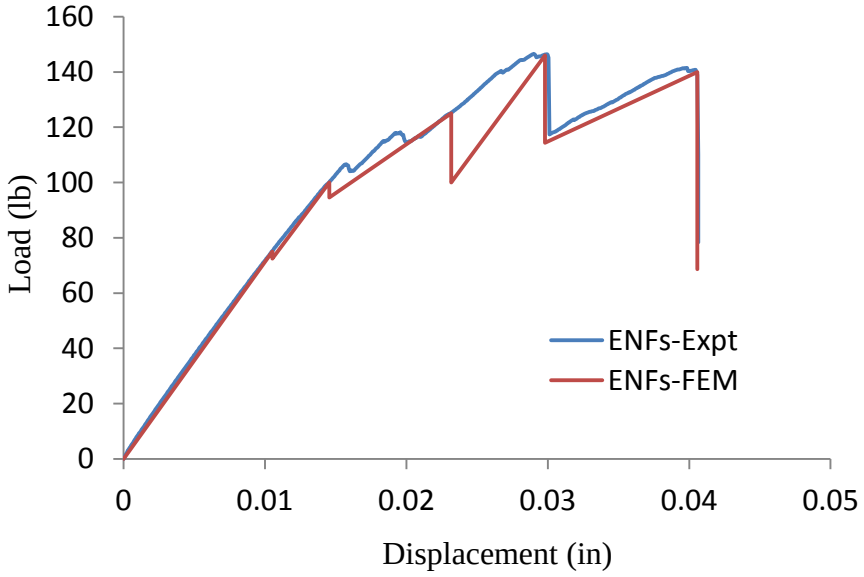


*Figure 5.27.* Comparison of experimental and FEM results of $[0/60/-60/-60/60/0]_s$ 12GF-11RF and ENFs composites in three point bend test

## 5.9 Comparison of Strain Energy with Experimental Results

Using Origin Lab software, the experimental data was analyzed to calculate strain energy absorbed each case of stacking sequence of the composites with and without TEOS ENFs. This was done by determining the area under the experimental load versus displacement curve. Table 5.7 shows the strain energy absorbed by each type of the composites, during the three point bending test.

*Table 5.7* Strain energy in each stacking sequence of the composites

| Stacking Sequence | Strain Energy of composite (FP) | | % increase in strain energy |
|---|---|---|---|
| | GF | GF-ENFs | |
| $[0/0/0/0/0/0]_s$ | 12.92 | 16.68 | 29.14 |
| $[0/90/90/0/0/90]_s$ | 8.41 | 9.02 | 7 |
| $[0/60/-60/-60/60/0]_s$ | 4.81 | 5.77 | 20 |
| $[+45/-45/45/-45/+45/-45]_s$ | 19.67 | 20.5 | 4 |

Experimental results indicate that in case of the strain energy absorption before the failure for the [0/0/0/0/0/0]s stacking sequence of the composite was about 30% more when TEOS ENFs interleaved. For the same configuration finite element analysis predicted that the strain energy absorbed by TEOS ENGs interleaved composite is increased by about 50%. Other stacking sequences with TEOS ENFs also shown improvement in the strain energy absorption and result are presented in Table 5.7.

## 5.10 Conclusions

The following are some of the conclusions of the finite element analysis.

1. A three dimensional 20 noded ANSYS SOLID186 element can be used for the progressive failure analysis of fiberglass composite beam.
2. A detailed 3-D finite element model of both fiberglass composites with and without presence of interleaved nanofibers mats was developed.
3. A Tsai-Wu failure criterion was used to predict the progressive failure of the fiberglass composites with and without presence of electrospun nanofibers.
4. The finite element analysis predicted that the strain energy absorbed by the TEOS ENFs interleaved composites for the [0/0/0/0/0/0]s stacking sequence increased by about 50% as compared to the experimental results which showed about 30% increase in strain energy absorption.
5. Three dimensional finite element model accurately predicted the progressive failures for the fiberglass composites with other stacking sequences including $[0/90/90/0/0/90]_s$ and $[0/60/-60/-60/60/0]_s$ with and without ENFs. The finite element results agreed well with the experimental results.

# CHAPTER 6

## Conclusions

The present investigation is concerned with the effects of electrospun nanofibers on the short beam strength of laminated fiberglass composite. TEOS electrospun nanofibers sintered at $600^0$ C were interleaved between the fiberglass plies and coupons were fabricated using out of autoclave vacuum bagging fabrication method. Fabricated coupons with and without presence of nanofiber mats were tested to study the progressive deformation and damage mechanics.

Four different fiberglass composite panels with symmetric, balanced stacking sequences were investigated. Thickness of each ply in the composite panels was evaluated using SEM imaging. The thickness of fiberglass prepreg, epoxy resin film and TEOS ENFs non-woven mat was found to be 0.00627 inches, 0.00802 inches, and 0.001085 inches respectively.

Three dimensional finite element model of the short beam specimen was developed using ANSYS finite element program to validate the experimental results. The progressive failure analysis of the short beam coupons fabricated using fiberglass plies with and without TEOS ENFs was performed. The finite element analysis resulted into following conclusions:

- A three dimensional 20 noded ANSYS SOLID186 element can be used for the progressive failure analysis of fiberglass composite beam.
- A detailed 3-D finite element model of both fiberglass composites with and without presence of interleaved nanofibers mats was developed.
- A Tsai-Wu failure criterion was used to predict the progressive failure of the fiberglass composites with and without presence of electrospun nanofibers.
- The finite element analysis predicted that the strain energy absorbed by the TEOS ENFs interleaved composites for the [0/0/0/0/0/0]s stacking sequence increased by about 50%

as compared to the experimental results which showed about 30% increase in strain energy absorption.

- Three dimensional finite element model accurately predicted the progressive failures for the fiberglass composites with other stacking sequences including $[0/90/90/0/0/90]_s$ and $[0/60/-60/-60/60/0]_s$ with and without ENFs. The finite element results agreed well with the experimental results.

The present investigation has also shown that future research is warranted in the following areas:

- Investigate the fracture toughness of the fiberglass composite interleaved with functionalized TEOS ENFs.
- Investigate other types of nanofibers for MSBS application.
- Effect of sintering on the performance of MSBS coupons.
- Perform the complete progressive failure using non-linear finite element analysis (use large displacement assumption) and dynamic analysis of MSBS model.
- Include effects of delaminations in the finite element model.
- Include failure criteria based upon transverse normal stresses.
- Study feasibility of using carbon nanofibers with carbon-epoxy prepreg.

## References

ASTM D. (1995). *Standard Test Method for Compressive Properties of Polymer Matrix Composite Materials with Unsupported Gage Section by Shear Loading*.

AGY. (2004). Advanced Materials Solutions for Demanding Applications. *AGY, Pub. No. LIT-2004-341 (03/04)* doi:March 2004

Alger, Mark SM. (1997). *Polymer science dictionary*: Springer.

Amaya, Peter. (2012). *Progressive Damage and Failure Model for Composite Laminates under Multiaxial Loading Conditions.* The Ohio State University.

ASTM (Ed.). (2002). *Annual Book of ASTM Standards* (Vol. vol. 15.3, ): ASTM International, West Conshohocken.

Astm, D. (2000). 3039/D 3039M-00. *Standard test method for tensile properties of polymer matrix composite materials, 10*.

Bolotin, VV. (1965). Basic equations of the theory of reinforced media. *Polymer Mechanics, 1*(2), 23-30.

Bui, QV. (2011). A modified Benzeggagh-Kenane fracture criterion for mixed-mode delamination. *Journal of Composite Materials, 45*(4), 389-413.

Camanho, Pedro Ponces. (2002). Failure Criteria for Fibre-Reinforced Polymer Composites. *DEMEGI, FEUP*.

Cantwell, Prof. Wesley. (2011). vacuum bagging. *Composite Forming Techniques.* from http://core.materials.ac.uk/repository/uol/mats311/slide2.jpg

Chamis, CC, & Sendeckyj, GP. (1968). Critique on theories predicting thermoelastic properties of fibrous composites. *Journal of Composite Materials, 2*(3), 332-358.

Chamis, Christos C. (1984). Simplified composite micromechanics equations of hygral, thermal, and mechanical properties. *Sampe Quarterly, 15*, 14-23.

Chaphalkar, Pramod, & Kelkar, A. (1999). *Analytical and experimental elastic behavior of twill woven laminate.* Paper presented at the Proceedings of the 12th International Conference on Composite Materials.

Chen, Qi, Zhang, Lifeng, Yoon, Myung-Keun, Wu, Xiang-Fa, Arefin, Ragib H, & Fong, Hao. (2012). Preparation and evaluation of nano-epoxy composite resins containing electrospun glass nanofibers. *Journal of Applied Polymer Science, 124*(1), 444-451.

Chen, Qi, Zhao, Yong, Zhou, Zhengping, Rahman, Arifur, Wu, Xiang-Fa, Wu, Weidong, . . . Fong, Hao. (2013). Fabrication and mechanical properties of hybrid multi-scale epoxy composites reinforced with conventional carbon fiber fabrics surface-attached with electrospun carbon nanofiber mats. *Composites Part B: Engineering, 44*(1), 1-7.

Cheremisinoff, Nicholas P, & Cheremisinoff, Paul N. (1995). *Fiberglass reinforced plastics: Manufacturing techniques and applications*: William Andrew.

Chorng-Fuh, Liu, & Horng-Shian, Jou. (1993). A new finite element formulation for interlaminar stress analysis. *Computers & structures, 48*(1), 135-139.

Cook, J, Gordon, JE, Evans, CC, & Marsh, DM. (1964). A mechanism for the control of crack propagation in all-brittle systems. *Proceedings of the Royal Society of London. Series A. Mathematical and Physical Sciences, 282*(1391), 508-520.

Cumings, R.C., & Vanderbos, T.G. (2008). Composite article debulking process: Google Patents.

Curtis P T. (1989). The fatigue behaviour of fibrous composite materials. *The Journal of Strain Analysis for Engineering Design, 24*(4), 235-244.

Daniel, IM, & Ishai, O. Engineering mechanics of composite materials, 1994: Oxford University Press, New York.

Davies, P, Blackman, BRK, & Brunner, AJ. (1998). Standard test methods for delamination resistance of composite materials: current status. *Applied Composite Materials, 5*(6), 345-364.

De Morais, AB, & Pereira, AB. (2008). Mixed mode II+ III interlaminar fracture of carbon/epoxy laminates. *Composites Science and Technology, 68*(9), 2022-2027.

Deitzel, J. M., Kleinmeyer, J., Harris, D., & Beck Tan, N. C. (2001). The effect of processing variables on the morphology of electrospun nanofibers and textiles. *Polymer, 42*(1), 261-272. doi: http://dx.doi.org/10.1016/S0032-3861(00)00250-0

Deitzel, J. M., Kosik, W., McKnight, S. H., Beck Tan, N. C., DeSimone, J. M., & Crette, S. (2002). Electrospinning of polymer nanofibers with specific surface chemistry. *Polymer, 43*(3), 1025-1029. doi: http://dx.doi.org/10.1016/S0032-3861(01)00594-8

Demczyk, BG, Wang, YM, Cumings, J, Hetman, M, Han, W, Zettl, A, & Ritchie, RO. (2002). Direct mechanical measurement of the tensile strength and elastic modulus of multiwalled carbon nanotubes. *Materials Science and Engineering: A, 334*(1), 173-178.

Demir, Mustafa Muammer, Yilgor, I, Yilgor, E e a1, & Erman, Burak. (2002). Electrospinning of polyurethane fibers. *Polymer, 43*(11), 3303-3309.

Designation, ASTM. (2003). D 638-03,". *Standard test method for tensile properties of plastics*, 1-15.

Dzenis, Yuris A, & Reneker, Darrell H. (2001). Delamination resistant composites prepared by small diameter fiber reinforcement at ply interfaces: Google Patents.

Fang, Jian, Niu, HaiTao, Lin, Tong, & Wang, XunGai. (2008). Applications of electrospun nanofibers. *Chinese Science Bulletin, 53*(15), 2265-2286.

Fong, H, Chun, I, & Reneker, DH. (1999). Beaded nanofibers formed during electrospinning. *Polymer, 40*(16), 4585-4592.

Fong, Hao, & Reneker, Darrell H. (1999). Elastomeric nanofibers of styrene–butadiene–styrene triblock copolymer. *Journal of Polymer Science Part B: Polymer Physics, 37*(24), 3488-3493. doi: 10.1002/(SICI)1099-0488(19991215)37:24<3488::AID-POLB9>3.0.CO;2-M

Formhals, Anton. (1934). Process and apparatus fob pbepabing: Google Patents.

Gao, Yi, Sagi, Sriramaraju, Zhang, Lifeng, Liao, Yiliang, Cowles, David M., Sun, Yuyu, & Fong, Hao. (2008). Electrospun nano-scaled glass fiber reinforcement of bis-GMA/TEGDMA dental composites. *Journal of Applied Polymer Science, 110*(4), 2063-2070. doi: 10.1002/app.28695

Gibson, PW, Schreuder-Gibson, HL, & Rivin, D. (1999). Electrospun fiber mats: transport properties. *AIChE journal, 45*(1), 190-195.

Goodsell, Johnathan, Pagano, Nicholas J, Kravchenko, Oleksandr, & Pipes, R Byron. (2013). Interlaminar stresses in composite laminates subjected to anticlastic bending deformation. *Journal of Applied Mechanics, 80*(4), 041020.

Gotsis, Pascal K, Chamis, Christos C, & Minnetyan, Levon. (1998). Progressive fracture of fiber composite thin shell structures under internal pressure and axial loads. *International Journal of Damage Mechanics, 7*(4), 332-350.

Greiner, Andreas, & Wendorff, Joachim H. (2007). Electrospinning: A Fascinating Method for the Preparation of Ultrathin Fibers. *Angewandte Chemie International Edition, 46*(30), 5670-5703. doi: 10.1002/anie.200604646

Harris, Charles E, & Morris, DH. (1986). A comparison of the fracture behavior of thick laminated composites utilizing compact tension, three-point bend, and center-cracked tension specimens. *Fracture Mechanics: Seventeenth Volume, ASTM STP, 905*, 124-135.

Hexcel. (January 2013). Hexply Prepreg Technology (2013 ed., Vol. FGU 017c): ® Hexcel Registered Trademark, © Hexcel Corporation.

Huang, Lei, Apkarian, Robert P, & Chaikof, Elliot L. (2001). High-resolution analysis of engineered type I collagen nanofibers by electron microscopy. *Scanning, 23*(6), 372-375.

Huang, Zheng-Ming, Zhang, Y-Z, Kotaki, M, & Ramakrishna, S. (2003). A review on polymer nanofibers by electrospinning and their applications in nanocomposites. *Composites science and technology, 63*(15), 2223-2253.

Hyer, Michael W. (2009). *Stress analysis of fiber-reinforced composite materials*: DEStech Publications, Inc.

Ishikawa, Takashi, & Chou, Tsu-Wei. (1982). Elastic behavior of woven hybrid composites. *Journal of Composite Materials, 16*(1), 2-19.

Kant, TARUN, & Swaminathan, K. (2000). Estimation of transverse/interlaminar stresses in laminated composites–a selective review and survey of current developments. *Composite structures, 49*(1), 65-75.

Kelkar, Ajit D, Mohan, Ram, Bolick, Ronnie, & Shendokar, Sachin. (2008). Effect of electrospun fibers on the Interlaminar properties of woven composites. *Advanced Materials Research, 47*, 1031-1034.

Kelkar, Ajit D, Tate, Jitendra S, & Bolick, Ronnie. (2006). Structural integrity of aerospace textile composites under fatigue loading. *Materials Science and Engineering: B, 132*(1), 79-84.

Kelkar, Ajit, Shendokar, Sachin, Kelkar, Anand, & Bolick, Ronnie. (2010
). *Effect of electrospun nanofibers on mechanical properties of epon 862-w*. Paper presented at the The 18'h Annual International conference on composites /Nano engineering - Icee-18 Anchorage, Alaska, USA.

KIM, Jong-Sang, & LEE, Dai Soo. (2000). Thermal Properties of Electrospun Polyesters. *Polymer journal, 32*(7), 616-618.

Lekhnitskiĭ, SG. (1963). *Theory of elasticity of an anisotropic elastic body*: Holden-Day.

Liao, Xiaoling, Li, Hejun, Xu, Wenfeng, & Li, Kezhi. (2008). Effects of tensile fatigue loads on flexural behavior of 3D braided C/C composites. *Composites science and technology, 68*(2), 333-336.

Liu, Haiqing, & Hsieh, You-Lo. (2002). Ultrafine fibrous cellulose membranes from electrospinning of cellulose acetate. *Journal of Polymer Science Part B: Polymer Physics, 40*(18), 2119-2129.

Liu, Yi, Sagi, Sriramaraju, Chandrasekar, Ramya, Zhang, Lifeng, Hedin, Nyle E, & Fong, Hao. (2008). Preparation and characterization of electrospun SiO2 nanofibers. *Journal of nanoscience and nanotechnology, 8*(3), 1528-1536.

Martin, Roderick H. (1991). Interlaminar fracture characterization: a current review: DTIC Document.

McCartney, LN. (2002). Prediction of ply crack formation and failure in laminates. *Composites science and technology, 62*(12), 1619-1631.

Morozov, VictorN, Morozova, TamaraYa, & Kallenbach, NevilleR. (1998). Atomic force microscopy of structures produced by electrospraying polymer solutions. *International Journal of Mass Spectrometry, 178*(3), 143-159.

Mouritz, AP. (2007). Review of z-pinned composite laminates. *Composites Part A: applied science and manufacturing, 38*(12), 2383-2397.

Mouritz, AP, Baini, C, & Herszberg, I. (1999). Mode I interlaminar fracture toughness properties of advanced textile fibreglass composites. *Composites Part A: Applied Science and Manufacturing, 30*(7), 859-870.

Naik, NK, & Ganesh, VK. (1992). Prediction of on-axes elastic properties of plain weave fabric composites. *Composites Science and Technology, 45*(2), 135-152.

Nandakumar, Pratap Nuggehalli, & Raju, Keshavanarayana Suresh. (2009). Load rate effects on Interlaminar fracture toughness of composite materials.

O'Brien, T Kevin. (1998). Interlaminar fracture toughness: the long and winding road to standardization. *Composites Part B: Engineering, 29*(1), 57-62.

Paiva, Jane Maria Faulstich de, Mayer, Sérgio, & Rezende, Mirabel Cerqueira. (2006). Comparison of tensile strength of different carbon fabric reinforced epoxy composites. *Materials Research, 9*, 83-90.

Pipes, R Byron, & Pagano, NJ. (1970). Interlaminar stresses in composite laminates under uniform axial extension. *Journal of Composite Materials, 4*(4), 538-548.

Raju, Ivatury S, & Wang, John T. (1994). Classical laminate theory models for woven fabric composites. *Journal of composites technology & research, 16*(4), 289-303.

Reddy, Junuthula Narasimha. (2004). *Mechanics of laminated composite plates and shells: theory and analysis*: CRC press.

Reneker, Darrell H, & Chun, Iksoo. (1996). Nanometre diameter fibres of polymer, produced by electrospinning. *Nanotechnology, 7*(3), 216.

Reneker, Darrell H, Yarin, Alexander L, Fong, Hao, & Koombhongse, Sureeporn. (2000). Bending instability of electrically charged liquid jets of polymer solutions in electrospinning. *Journal of Applied physics, 87*, 4531.

Sakka, S, & Kamiya, K. (1982). The sol-gel transition in the hydrolysis of metal alkoxides in relation to the formation of glass fibers and films. *Journal of Non-Crystalline Solids, 48*(1), 31-46.

Sankar, Bhavani V, & Sharma, Suresh K. (1997). Mode II delamination toughness of stitched graphite/epoxy textile composites. *Composites Science and Technology, 57*(7), 729-737.

Sengupta, Jayashree. (2014). *Progressive Failure of Laminated Composite Cylindrical Shells.*

Shendokar, Sachin, Kelkar, Ajit, Mohan, Ram, Bolick, Ron, & Chandekar, Gautam. (2008). *Effect of Sintering Temperature on Mechanical Properties of Electrospun Silica Nanofibers*.

Sierakowski, Robert L, & Newaz, Golam M. (1995). *Damage tolerance in advanced composites*: CRC PressI Llc.

Slager, Aaron. (2007). Interlaminar Fracture Of Unidirectional Reinforced Composites With Toughnened Resin Systems.

Standard, ASTM. (2001). D3518/D3518M–94 (2001). *Standard Test Method for In-Plane Shear Response of Polymer Matrix Composite Materials by Tensile Test of a±45º Laminate. Annual Book of ASTM Standards, 15*.

Standard, ASTM. (2005). D5379/D5379M, 2005. *Standard Test Method for Shear Properties of Composite Materials by the V-Notched Beam Method. West Conshohocken, PA.*

Standard, ASTM Test. (2000). D2344/D2344M-00el,". *Standard Test Method for Short-Beam Shear Strength of Polymer Matrix Composite Materials and Their Laminates." ASTM lntemational, West Conshohockcn, PA*.

Stillwell, CR. (1996). Characterization of pore structure in filter cartridges. *Advances in filtration and separation technology*, *10*, 151.

Strong, A Brent. (2008). *Fundamentals of composites manufacturing: materials, methods and applications*: Sme.

Talreja, Ramesh. (2006). Multi-scale modeling in damage mechanics of composite materials. *Journal of materials science*, *41*(20), 6800-6812.

Tan, P, Tong, L, & Steven, GP. (1997). Modelling for predicting the mechanical properties of textile composites—a review. *Composites Part A: Applied Science and Manufacturing*, *28*(11), 903-922.

Tan, S. H., Inai, R., Kotaki, M., & Ramakrishna, S. (2005). Systematic parameter study for ultra-fine fiber fabrication via electrospinning process. *Polymer*, *46*(16), 6128-6134. doi: http://dx.doi.org/10.1016/j.polymer.2005.05.068

Taylor, Geoffrey. (1964). Disintegration of water drops in an electric field. *Proceedings of the Royal Society of London. Series A. Mathematical and Physical Sciences*, *280*(1382), 383-397.

Teo, WE, & Ramakrishna, S. (2006). A review on electrospinning design and nanofibre assemblies. *Nanotechnology*, *17*(14), R89.

Todo, M, Jar, P-YB, & Takahashi, K. (2000). Initiation of a mode-II interlaminar crack from an insert film in the end-notched flexure composite specimen. *Composites Science and Technology*, *60*(2), 263-272.

Tsai, Stephen W, & Wu, Edward M. (1971). A general theory of strength for anisotropic materials. *Journal of composite materials, 5*(1), 58-80.

Velmurugan, R, & Solaimurugan, S. (2007). Improvements in Mode I interlaminar fracture toughness and in-plane mechanical properties of stitched glass/polyester composites. *Composites science and technology, 67*(1), 61-69.

Voigt, W. (1889). On the relation between the elasticity constants of isotropic bodies. *Ann. Phys. Chem, 274*, 573-587.

Wang, Youjiang, & Zhao, Dongming. (1995). Characterization of interlaminar fracture behaviour of woven fabric reinforced polymeric composites. *Composites, 26*(2), 115-124.

Wang, Yu, Serrano, S, & Santiago-Aviles, JJ. (2002). Conductivity measurement of electrospun PAN-based carbon nanofiber. *Journal of materials science letters, 21*(13), 1055-1057.

Wen, Shipeng, Liu, Li, Zhang, Lifeng, Chen, Qi, Zhang, Liqun, & Fong, Hao. (2010). Hierarchical electrospun SiO2 nanofibers containing SiO2 nanoparticles with controllable surface-roughness and/or porosity. *Materials Letters, 64*(13), 1517-1520. doi: http://dx.doi.org/10.1016/j.matlet.2010.04.008

Whitcomb, JohnD. (1991). Three-dimensional stress analysis of plain weave composites. *Composite materials: Fatigue and fracture., 3*, 417-438.

Wicks, Sunny S, de Villoria, Roberto Guzman, & Wardle, Brian L. (2010). Interlaminar and intralaminar reinforcement of composite laminates with aligned carbon nanotubes. *Composites Science and Technology, 70*(1), 20-28.

Wong, Eric W, Sheehan, Paul E, & Lieber, Charles M. (1997). Nanobeam mechanics: elasticity, strength, and toughness of nanorods and nanotubes. *Science, 277*(5334), 1971-1975.

Wood, Michael DK, Sun, Xiannian, Tong, Liyong, Luo, Quantian, Katzos, Anthony, & Rispler, Adrian. (2007). A new ENF test specimen for the mode II delamination toughness testing of stitched woven CFRP laminates. *Journal of composite materials, 41*(14), 1743-1772.

Xu, HHK, Sun, L, Weir, MD, Antonucci, JM, Takagi, S, Chow, LC, & Peltz, M. (2006). Nano DCPA-whisker composites with high strength and Ca and PO4 release. *Journal of dental research, 85*(8), 722-727.

Yang, Chuijin, Chen, Jubing, & Zhao, Shexu. (2013). The Interlaminar Stress of Laminated Composite under Uniform Axial Deformation. *Modeling and Numerical Simulation of Material Science, 3*, 49.

Zako, Masaru, Uetsuji, Yasutomo, & Kurashiki, Tetsusei. (2003). Finite element analysis of damaged woven fabric composite materials. *Composites Science and Technology, 63*(3), 507-516.

Zhang, YX, & Yang, CH. (2009). Recent developments in finite element analysis for laminated composite plates. *Composite Structures, 88*(1), 147-157.

Zhu, Jiang, Imam, Ashraf, Crane, Roger, Lozano, Karen, Khabashesku, Valery N, & Barrera, Enrique V. (2007). Processing a glass fiber reinforced vinyl ester composite with nanotube enhancement of interlaminar shear strength. *Composites Science and Technology, 67*(7), 1509-1517.

Zong, Xinhua, Kim, Kwangsok, Fang, Dufei, Ran, Shaofeng, Hsiao, Benjamin S, & Chu, Benjamin. (2002). Structure and process relationship of electrospun bioabsorbable nanofiber membranes. *Polymer, 43*(16), 4403-4412.

Zussman, E, Chen, X, Ding, W, Calabri, L, Dikin, DA, Quintana, JP, & Ruoff, RS. (2005). Mechanical and structural characterization of electrospun PAN-derived carbon nanofibers. *Carbon, 43*(10), 2175-2185.